

2



Naval Oceanographic and
Atmospheric Research Laboratory

Technical Note 87
November 1990

Satellite Altimetry for Naval Oceanography

AD-A231 081

DTIC
ELECTE
JAN 17 1991
S E D

D. R. Johnson
Remote Sensing Branch
Ocean Sensing and Prediction Division
Ocean Science Directorate

Approved for public release; distribution is unlimited. Naval Oceanographic and Atmospheric Research Laboratory,
Stennis Space Center, Mississippi 39529-5004.

These working papers were prepared for the timely dissemination of information;
this document does not represent the official position of NOARL.

ABSTRACT

Taking advantage of experience gained during the flight of the U.S. Navy's GEOSAT altimeter, this technical note discusses some of the problems encountered and recommends new approaches for future altimeter systems. In particular, I strongly urge that exact-repeat track sampling be continued for the next decade. Optimum sampling for mesoscale features can be realistically accomplished with three altimeters flying at 7-day refresh periods with equidistant crosstrack spacing. More formal recommendations will come with the results of current studies using various configurations during mission simulations. It is also recommended that additional effort be invested in sea-ice monitoring and in geophysical corrections.

Accession For	
NTIS GRA&I	<input checked="" type="checkbox"/>
DTIC TAB	<input type="checkbox"/>
Unannounced	<input type="checkbox"/>
Justification	
By	
Distribution/	
Availability Codes	
Dist	Avail and/or Special
A-1	

ACKNOWLEDGMENTS

This work was supported by the Oceanographer of the Navy, Program Element 63704N, Space and Naval Warfare Systems Command, "Satellite Applications and Technology." I benefitted greatly from comments by A. Pressman, J. Hawkins, J. Mitchell and V. Noble.

The mention of commercial products or the use of company names does not in any way imply endorsement by the U.S. Navy or NOARL.

CONTENTS

	PAGE
I. INTRODUCTION	1
II. SPECIFICATIONS	3
III. RECOMMENDATIONS	5
IV. REPEAT ORBIT SAMPLING	7
V. SPACE AND TIME SAMPLING	11
VI. ACCURACY/RADIAL ORBIT DETERMINATION	17
VII. JOINT PROGRAMS	19
VIII. SEA ICE	20
IX. GEOPHYSICAL CORRECTIONS	23
REFERENCES	35
APPENDIX A. LIST OF ACRONYMS	37
APPENDIX B. RELEVANT PUBLICATIONS	39

SATELLITE ALTIMETRY FOR NAVAL OCEANOGRAPHY

I. INTRODUCTION

This technical note addresses the problem of new approaches to satellite altimetry which will be needed to meet future naval tactical and strategic performance goals. In particular, it considers advanced sampling strategies and increased measurement accuracies that will lead to improved operational geophysical products.

The U.S. Navy's Geodesy Satellite (GEOSAT) failed in January 1990, after supplying nearly 4.75 years of critical data on global ocean topography, as well as nadir measurements of wind speed, significant wave height, and sea-ice edge location. One of the major reasons for the success of GEOSAT came with the Exact Repeat Mission (ERM), a NOARL-designed and Navy sponsored effort focused on the use of satellite altimetry for oceanography. This effort provided more oceanographic altimetry than has previously existed, and for the first time allowed Navy operational, as well as scientific, benefits of satellite altimetry to be realized in a major way. This unprecedented data set has created a new view of the global oceans from a scientific perspective. In addition, such efforts as the GEOSAT Ocean Applications Program (GOAP) have successfully addressed the more difficult problem of deriving useful geophysical products on a Navy operational near-real

time scale. From these experiences, recommendations can be offered on improvements which will help the Navy meet future tactical and strategic performance goals.

The U.S. Navy's GEOSAT program has created optimism in the scientific community on the ability of satellite altimeters to monitor global ocean and ice dynamics. However, significant problems remain with the ability of a single altimeter to satisfactorily monitor the ocean mesoscale in an operational time frame. Data fusion with simultaneous measurements by other instruments (including additional altimeters) and data assimilation into numerical models need to be considered, as well as improvements in geophysical corrections. For this reason, specifications for future altimeters must be developed as part of a system rather than as a single engineering entity.

In this technical note the need for repeat orbit sampling, the use of multiple altimeter satellites and/or single satellites with multiple beam altimeters, and different strategies for orbital configurations are examined. This technical note provides a first-cut summary of recommendations which we plan to refine by direct simulation of the ingestion of altimetry into the Navy's future operational data streams. It is anticipated that these more rigorous studies will require a refinement of the recommendations.

In addition to mesoscale oceanography sampling requirements, the need for improved sea ice sampling and geophysical corrections are discussed. The technical note is organized so that

a specifications list and a set of recommendations come first, followed by the text. An Appendix contains relevant publications on the subject.

II. SPECIFICATIONS

A. COVERAGE:

1. ± 81.5 degrees latitude (nominal) for sea ice and ocean mesoscale coverage.
2. ± 65 degrees latitude (nominal) for ocean mesoscale (refer to section VIII).
3. ± 72 degrees latitude (GEOSAT/SEASAT) (** NOTE 1).
4. 8.5 degree longitudinal track separation per day (** NOTE 2).

B. ORBIT:

1. Exact repeat to ± 1 km (cross track - ** NOTE 3).
2. 3 to 35 day refresh periods - dependent upon availability of simultaneous measurements, such as from other altimeters or AVHRR, and assimilation methodology.

C. PRECISION:

SEA-SURFACE HEIGHT: ± 3 cm

SURFACE SLOPE: $\pm 5.0E-07$ (** NOTE 4).

SEA-ICE EDGE: ± 7 km (nominal footprint diameter).

SEA-ICE CONCENTRATION: $\pm 5\%$ (** NOTE 5).

SEA-ICE FREEBOARD: ± 25 cm (** NOTE 6).

WIND SPEED: ± 1 m/s

SURFACE WAVE HEIGHT: ± 0.1 m

D. ACCURACY:

SEA-SURFACE HEIGHT: ± 10 cm difference at 100 km separation

(** note 7); degrades to detection only at 50% of mesoscale height anomaly.

SATELLITE HEIGHT ABOVE SEA LEVEL: ± 5 cm.

SURFACE SLOPE: $\pm 1.0E-06$; degrades to unusable at $\pm 2.0E-06$.

SEA-ICE EDGE: ± 7 km

SEA-ICE CONCENTRATION: $\pm 10\%$; degrades to unusable at 25%.

SEA-ICE FREEBOARD: ± 50 cm; degrades to unusable at 2 m.

WIND SPEED: ± 1 m/s or 10%, whichever is greater.

SURFACE WAVE HEIGHT: ± 0.5 m or 10%, whichever is greater.

E. TIMELINESS:

SEA-SURFACE HEIGHT: 6 hr (degrades to unusable at 5-7 days).

SURFACE SLOPE: 6 hr (degrades to unusable at 5-7 days).

SEA-ICE: 6 hr (degrades to unusable at 5-7 days).

WIND SPEED: 3 hr (degrades to unusable at 12 hrs).

SURFACE WAVE HEIGHT: 3 hrs (degrades to unusable at 12 hrs).

NOTES:

- (1) The GEOSAT/SEASAT orbit follows a non-sun-synchronous, exact-repeat track. The advantages to selecting this orbit for near-future altimeters are that a reference surface (see section IV) is available for immediate use (including synthetic geoids in some regions), and that over 3 years of statistics are available for improved statistical prediction models.
- (2) This requires three altimeters flying simultaneously. Thirty-three percent degradation for each missing altimeter (Advanced Very High Resolution Radiometer (AVHRR) can be considered nominally equivalent to one altimeter for detection only). One multibeam altimeter with 50-km side beams and a 20-day refresh period can provide adequate coverage for non-eddy-resolving global model assimilation, but is not adequate for eddy-resolving assimilation.
- (3) With non-repeat orbit, application is limited to detection of mesoscale features in the few areas where a highly accurate geoid is available. Objective data assimilation is not feasible with non-repeat orbits.
- (4) Cross-track SSH slope is obtainable with a multibeam altimeter. Together with along-track slope, it can be used to calculate current vectors. The precision given here allows current speed calculations to ± 5 cm/s at 45 degrees

latitude. It should be noted, however, that SSH slope is not presently being considered for use in Navy operational products.

- (5) Ice coverage sets specifications for parameterization of waveform (refer to Section VIII).
- (6) Ice freeboard sets specifications for recording and transmitting tracking parameters (for retracking surface refer to Section VIII).
- (7) Radial orbit determination is a dominant source of error in SSH, overwhelming mesoscale anomaly heights. Fortunately the large wavenumber gap between mesoscale features and the radial orbit errors has allowed regional corrections at the decimeter level. The accuracy given here specifies that along-track SSH differences to within ± 10 cm should be obtainable over a distance of 100 km (refer to Section VI).

III. RECOMMENDATIONS

A. The altimeter specifications listed in Section II provide general guidance for mission design of future altimeter systems. It should be noted that such specifications as coverage and refresh periods should not be determined separately from considerations of an altimeter as part of a sampling system. More formal recommendations on sampling strategy are being developed, based upon ocean mission simulations.

B. Because the uncertainty in geoid determination tends to mask ocean dynamic topography from altimetry, repeat orbit sampling is essential over most of the ocean for mesoscale analysis. Repeat orbits allow a reference surface , which serves as a geoid, to be generated.

C. Refresh times of 3 to 35 days are candidate repeat periods for naval operational usage. These periods are dependent upon the number of altimeters, the availability of simultaneous measurements such as Advanced Very High resolution Radiometer (AVHRR), and the assimilation models used. Based upon experience during the GEOSAT mission, the optimum realistic space/time sampling of mesoscale features would occur with three altimeters at 7-day refresh periods and phased for homogeneous cross-track separation.

D. For the near-future GEOSAT Follow-On altimeters, it is recommended that sampling be continued along the GEOSAT-ERM groundtrack. The reference surface and statistics, determined from over 3 years of sampling, can be immediately incorporated into Navy models.

E. Proper mission design work for altimetric satellites should identify those candidate repeat orbits which also satisfy the constraints imposed by ground-station overpass, sun-chronicity, altitude, and input times (see specification list) for models which require time-critical data.

F. DMSP Block 6 polar orbiters should carry altimeters, and repeat orbits found that satisfy all constraints. Satellite altimeters on foreign and other-agency platforms should be considered for cost-effective exploitation, and negotiations for raw altimetry data done at an early stage.

G. Sea-Ice monitoring by altimeters should be considered as part of the sampling strategies. Parameterization of the waveform for efficient extraction of ice information should be included in the Sensor Data Record (SDR).

H. Geophysical corrections are a major concern. Altimeters of the future should carry bore-sighted radiometers for water vapor corrections. Effective algorithms for electromagnetic bias

should be sought. Tidal models need improvements in many shallow-water regions. The effect of atmospheric pressure loading across a spectrum of frequencies and wavenumbers needs to be investigated and a model developed.

I. Advanced techniques in radial orbit determination, such as PRARE (Precise Range and Range Rate Experiment) and unmanned undertrack transponders (COMPASS Experiment), should be exploited in order to drive the radial orbit accuracy to below 10 cm.

IV. REPEAT ORBIT SAMPLING

Flying satellite altimeters in a non-repeat orbit has some advantages. Among these are weight reduction (engendered by elimination of the on-board station keeping fuel and hardware - this may be crucial with inexpensive launch vehicles such as the PEGASUS), elimination of extra costs of station keeping, and elimination of sample time lost during orbit adjustments.

The crucial question, which must be addressed in planning altimeter missions with non-repeat sampling, is whether or not the marine geoid will be sufficiently known in the next decade to avoid contamination of the ocean dynamic signal with geoid uncertainties. Exact determination of the marine geoid has been one of the principal concerns in using altimetry measurements to estimate Sea Surface Height (SSH) topography (defined as the

contribution from subtidal ocean dynamics to sea level variation in space and time). Since both the marine geoid and the SSH signals are modified by organized bathymetric features, no wavenumber spectral gap is available to distinguish one from the other. Separation of the relatively small SSH signals from the much larger marine geoid undulations requires independent measurements of both.

The marine geoid can vary by tens of meters over the global ocean, and as much as 40 cm/km over length scales of tens of kilometers near steep bottom topography. This signal, if not eliminated from the altimeter time delay, can overwhelm the SSH contribution of tens of centimeters. Furthermore, this is not a problem associated only with steep bottom topography or with long wavelengths. Global geoid slopes are characteristically about ± 5 cm/km over a length scale of 100 km. Larger slopes can occur with smaller length scales - Brenner et al., (1990), suggest that corrections might need to be made for the ± 1 km ground-track wandering of GEOSAT during the ERM period. Knowledge of the marine geoid to within a horizontal resolution of 1 km would be needed to provide a signal error contribution of less than 5 cm on a global scale. In areas of strong geoidal changes, such as the Japan/Kurile Trench (Kuroshio), Emperor Seamounts (Kuroshio Extension), New England Seamounts (Gulf Stream) and Iceland/Faeroes Ridge (Iceland/Faeroes Front), these errors can be even more significant (Ca. 10-40 cm). It must be noted that these examples

are exactly the regions of high Navy interest for mesoscale oceanography.

Obtaining high resolution measurements of the marine geoid will continue to be a major problem for some time in the future. Shipboard gravity surveys are much too slow and expensive for the density of measurements needed. Our present geoids were created by using altimeter measurements blended with surveys where available. But the altimeter measurements from GEOSAT Pre-ERM meld ocean dynamic topography with geoid measurements. Hence, even the best classified geoids are contaminated by the ocean SSH which we seek to measure for naval applications. From a geodesist's point of view, the SSH signal is a minor error on the geoid. From the tactical oceanographer's point of view, however, the contamination is critical. Collinear averaging during the ERM period has improved geoidal estimates along the repeat track, since this method tends to smear the SSH signals over longer wavelengths. However, such an improvement is valid only near the repeat ground-tracks -- 60 km spacing at midlatitudes. Mean dynamic topography inclusion in the geoid near strong ambient currents, such as the mean Gulf Stream, remains large (ca. 100 cm).

This problem was avoided during the GEOSAT pre-ERM period by cross-over point differencing and in the ERM period by collinear differencing, or by the use of independent "data" such as in situ measurements (Mitchell et al., 1990) or simulated topography (Kelly and Gillie, 1990). Since the SSH varies temporally, but the geoid does not, differencing eliminates the

geoid. Differencing also eliminates the absolute (temporal mean) SSH. It is the temporal variation about the mean, which remains in the SSH, that has contributed so significantly to our interpretation of altimeter signals in terms of ocean mesoscale dynamics. If we do not use a repeat orbit, the differencing can only be done at cross-over points. The majority of data, which falls in between the cross-over points, will not be usable for SSH retrieval. The alternative of using the present best classified geoid is not satisfactory for universal oceanography because of contamination by simultaneously included ocean SSH.

In figure 1, the difference is illustrated between subtracting a geoid contaminated with dynamic topography and subtracting a collinear reference surface. If we assume, for simplicity of argument, that there are no tides, no environmental corrections and no orbital errors, then the altimeter-measured sea level at time index, i , is composed of the true marine geoid plus the instantaneous dynamic topography:

$$H_i = G + D_i$$

where H_i = altimeter measured sea level

G = true marine geoid

D_i = instantaneous dynamic topography at time i .

From the geodetic mission, H_i , assimilated with sparse shipboard measurements, became the "measured marine geoid." Future measurements of the ocean surface, H_j , at time index, j , are subtracted from H_i in order to obtain an estimate of dynamic

topography:

$$\tilde{D}_j = H_j - H_i.$$

Since the true marine geoid cancels in this difference, the estimate of dynamic topography becomes

$$\tilde{D}_j = D_j - D_i.$$

Figure 1 shows two examples of instantaneous dynamic topography across the Gulf Stream region (figs. 1a and 1b) and the resulting difference between the two (fig. 1c). Although the cold core ring can be easily located in this example, the warm core ring and the Gulf Stream locations are ambiguous.

The second method, shown in figure 1, creates a reference surface, R , by averaging over N collinear passes:

$$R = G + (\sum_i D_i)/N$$

Since the ocean features vary in location and amplitude, the averaged dynamic topography will be smoothed. When this reference surface is subtracted from an instantaneous measurement, the marine geoid is eliminated:

$$\tilde{D}_j = H_j - R = D_j - (\sum_i D_i)/N$$

The resulting picture of the Gulf Stream area is superior using the collinear reference surface technique.

Although we can expect improvements in our computations of the marine geoid during the next decade and improvements in our ability to separate the SSH signal from the geoid, there is no present indication that we will be able to reach the point where the separation will be satisfactorily achieved in time for the next generation of altimeters. In addition, long term

measurements from non-changing orbits are needed in order to generate statistically significant time series. This is of major importance for understanding, as well as for predicting, ocean dynamics. For the foreseeable future, it is essential that satellite altimeters designed to monitor the ocean mesoscale be flown in orbits whose ground-tracks repeat to within ± 1 km.

Mission design work for future satellites will need to identify those candidate orbits that satisfy the constraint of specific local time overflight and exact-repeating ground-tracks, along with the constraint of effective operating altitude. During the Navy-Remote Ocean Sensing System (N-ROSS) mission design exercise, these constraints had to be met, as well as constraints imposed by ground-track separation. Sun-synchronous, exact repeat orbits that satisfied ground-station overflights (with limited interference by other Defense Meteorological Satellite Program (DMSP) satellites) were successfully identified (Mitchell and Born, 1984; Eisele and John, 1984).

V. SPACE AND TIME SAMPLING

The U.S. Navy has a high priority need for an eddy-resolving ocean monitoring and prediction capability in support of antisubmarine warfare (ASW). Such a capability will be achieved when satellite-derived SSH topography of high precision and spatial/temporal resolution can be assimilated into computer models of the ocean's dynamics and thermodynamics. With recent improvements in hardware and in geophysical corrections,

precision to within 5 cm is achievable. However, the limited spatial/temporal sampling resolution of previous and upcoming single-satellite altimeter systems is a principal concern that must be addressed with improved sampling capabilities, as well as with improved data fusion and data assimilation techniques.

With present satellite systems, such as GEOSAT, Environmental Research Satellite (ERS-1) and Topography Experiment (TOPEX), a single instrument obtains a nadir sample at an along-track separation of approximately 0.7 km. Beam size in a roughened sea, as well as averaging in order to achieve SSH precision of 5 cm, produces an effective along-track resolution of about 7 km. Since tactically significant eddies are those with diameters of 25 km Greenland-Iceland-Norwegian Sea (GIN Sea) to 150 km (Gulf Stream), the along-track resolution and precision are sufficient. However, cross-track spatial and temporal resolution are both insufficient for complete coverage. The tradeoffs between space and time coverage using a single beam, single satellite are such that both needs cannot be fulfilled at a 100% level without resorting to additional measurements.

At a nominal altitude of 800 km, satellite-borne altimeters orbit the earth at the rate of about 14.3 revolutions per day. At midlatitudes this produces a daily track separation, considering both ascending and descending tracks, of nominally 1200 km. Under this scenario, then, it would take about 8 to 12 days to produce a sampling grid capable of marginally locating Gulf Stream size eddies, and up to 48 days to resolve a GIN Sea eddy.

But in this 8 to 48-day window, the eddies migrate from 25 km to over 300 km away from their initial point, and the resulting picture from this nonsynoptic sampling scheme creates a distorted version of mesoscale features.

This difficulty is somewhat ameliorated because the smaller eddies typically occur at higher latitudes where cross-track spacing is tighter. The problem, however, is not completely satisfied by a single altimeter. In order to produce an operational product during GOAP (see Appendix) altimeter data from GEOSAT was supplemented by AVHRR. Based upon this experience, the relative contributions to the final product as derived from AVHRR, altimetry and analyst estimates (guesses) were about one-third each. AVHRR is not consistently available due to cloud cover and is suitable for detection only, not for direct assimilation into models.

Since the space and time coverage of satellite altimeters is necessarily sequential, and since microwave radars are incapable of directly monitoring subsurface structure, modeling techniques have been sought that incorporate sequential surface data into numerical ocean dynamic models. Data assimilation techniques, first used in an equivalent context for meteorology, show promise in covering unsampled areas, as well as in recreating subsurface structure from surface data. But how well can these techniques substitute for measurements? Definitive studies are lacking - partly due to the rapid developments in this area; however, some indications are available.

Using the results of a North Atlantic three layer model as ground truth and sampling the model SSH as if an altimeter satellite were flown with repeat orbits of 3, 10, 17 and 29 days, Verron (1990) studied assimilation efficiency by comparing the time evolution of the modeled ground truth against assimilation. The 10- and 17-day repeat orbits gave the best results for capturing the midlatitude jet circulation and mesoscale variability, with root mean square variability between assimilation and ground truth reduced to 35% - 40% of the initial uncorrelated state. This crudely suggests that the combination of a single altimeter with assimilation techniques can provide about 65% of the required information. While modeling techniques can improve our ability to interpolate, it cannot be expected to replace real measurements.

During 1991, a Gulf Stream nowcast/forecast system based upon the GEOSAT altimeter and infrared (IR) analyses coupled to a realistic primitive equation (PE) circulation model of the Northwest Atlantic will be placed into Navy operations at both the Naval Oceanographic Office (NAVO) Operational Oceanographic Center (OOC) and Fleet Numerical Oceanographic Center (FNOC). Within the next several years, an analogous system for the entire North Pacific basin (at regional/tactical scale resolution) will be fully developed. These systems provide for direct coupling of ocean mesoscale altimetric information to range-dependent PE acoustic model runs. Simulations are planned to include a full examination

of the mission design options and requirements and their resultant impact on acoustic products. The following will be simulated:

- (1) orbit selection (repeat periods, effects of non-repeat orbits and various orbital inclinations),
- (2) single vs. multisatellite vs. multibeam altimeter missions (i.e., sampling strategies),
- (3) precision requirements for measurement of surface topography (SSH),
- (4) accuracy requirements for measurement of SSH,
- (5) requirements for other environmental corrections (e.g., ionosphere/water vapor), and
- (6) timeliness requirements and impact on operational products.

In order to maximize altimetry data exploitation, these analysis and prediction systems should be incorporated into the system design.

It has been suggested that a multibeam altimeter would improve the space/time resolution problem. Brown et al. (1989) show that a pure multiple beam system (independent measurements for each beam) is feasible, with some restrictions and limitations. At a satellite altitude of 800 km, a three-beam system was suggested, with a nadir beam and one beam on each side of the flight direction at a 50 km ground-track separation. Wider separation would involve flying the satellite at a higher altitude in order to achieve the same 5-cm level of precision. It should be noted that the off-nadir samples would not provide

information on wind speed and wave height. It is possible, however, that off-nadir beams may provide additional sea ice information. Some interesting opportunities may exist with off-nadir, polarized beams- - it is suggested that Naval Research Laboratory (NRL) examine this problem.

Figure 2 shows the sampling pattern for three single-beam altimeters, with cross-track separation of 50 km. This coverage pattern is similar to a three-beam altimeter and is sufficient for discussion purposes. In figure 2 shows 3 days of GEOSAT's 17 day repeat orbit. This characteristic 3-day near-repeat orbit (GEOSAT & ERS-1 contain this near-repeat pattern) can be used to discuss spatial/temporal coverage of longer repeat periods. Over each subsequent 3 days, the pattern will be repeated, but shifted to the east. In this case, the shift will be about 125 km in the midlatitudes, so that ocean coverage to approximately 50 to 60-km spatial resolution can be made with the entire 17- day pattern.

A 50-km cross track separation is sufficient to adequately resolve most Gulf Stream size eddies and Gulf Stream size frontal distortions. Furthermore, additional information about eddy and frontal characteristics can be obtained from a multibeam system that can not be discerned from a single beam altimeter. These characteristics include size, amplitude, and swirl velocity, as well as higher precision location. Better estimates of surface current velocity can also be obtained at stream crossings, since local bending of the fronts can be derived. These characteristics can be determined only with simultaneous measurements, such as

obtained with a multibeam system.

However, figure 2 also demonstrates that the same spatial sampling problem occurs as with single beam altimeters. The large diamond-shaped areas are empty of measurements on an operational time window and will only non-synoptically be filled in. Deployment of a single multibeam altimeter will basically provide additional and improved information close to the nadir point, but will not significantly help in the large scale synoptic sampling problem. In cases of basin scale assimilation into models, the single multibeam altimeter will not be as effective as multiple single-beam altimeters flying at better spacing. Even for the mesoscale, several single-beams with complementary groundtrack coverage could provide more synoptic coverage over a regional domain than a single multibeam.

Although the best scenario, from a strictly sampling point of view, would involve multiple multibeam altimeters, the cost and feasibility of such a system may soon be prohibitive future. Multiple satellites with single-beam altimeters can provide more uniform coverage in space and time. As an example of alternative schemes, consider three single-beam satellites, phased to fly adjacent orbits with 7-day repeats at an inclination of about 98 degrees. At 40 degrees latitude, the paths would be about 100 km apart. Considering both ascending and descending tracks, the cross-track sample spacing would nominally be 50 km, an adequate midlatitude mesoscale coverage. As an additional advantage, the adjacent paths would be convergent at higher latitudes where eddy

size scales also become smaller; e.g., at 65 degrees latitude (Iceland/Faeroes Front) the sample spacing would reduce to nominally 28 km (in contrast, the multibeam altimeter track separation remains constant). In this scenario, one of the satellites might carry precise orbit determination equipment (refer to Section VI) and the other two orbits laid down by adjustment at cross-over points with the precise orbit satellite.

Many such scenarios exist. Care should be taken to design orbits such that fusion of different data types from different satellites can be optimized. Orbit repeats of 3 to 35 days are optimum for general operational time scales, but this depends heavily on concurrent measurements from other sources. Better definitions of sampling strategies will come from current programs.

VI. ACCURACY/RADIAL ORBIT DETERMINATION

Although measurements of sea ice, Significant Wave Height (SWH) and wind speed are important to the full complement of Navy operational products, measurements of SSH are given the highest priority for satellite radar altimeters. Fundamental to the determination of SSH, however, is the accuracy of the altimeter system in measuring absolute sea level (the height of the ocean surface relative to an earth reference ellipsoid). It should be noted that absolute sea level contains contributions from SSH, tides, and the marine geoid.

Accuracy specifications have, unfortunately, suffered from somewhat ambiguous definitions. A common definition specifies accuracy as the ability of the altimeter to measure the distance

between it and the surface of the ocean. This definition of accuracy takes into account the speed of signal transmission, the nature of the reflecting surface and the ability to time the echo. However, it does not account for uncertainty in the satellite's position. Providing a realistic accuracy specification for SSH products (rather than "altimeter" accuracy) demands that the specification include radial orbit uncertainty, since this is the major contributor to SSH error.

Tracking during the GEOSAT-ERM gave a radial orbit uncertainty of approximately 2 m over the Northwestern Atlantic. This level of uncertainty is greater than the SSH signals of interest. Fortunately, the dominant error comes from a once per revolution "bounce" of the satellite, with the error falling off rapidly at higher harmonics. Various methods of removing the long wavelength error, such as tilt and bias removal, were successfully applied in order to retrieve ocean SSH signals with wavelengths of less than a few hundreds of kilometers. However, basin scale (10,000 km) SSH topography is also removed; hence, circulation applicable to global and basin scale models cannot be calculated.

It is recommended that advanced tracking techniques be investigated for future altimeter systems. In addition to the Global Positioning Satellite (GPS) system, the French DORIS and the ESA PRARE are capable of tracking to the decimeter level. A collaborative experiment between NOARL and the Rutherford Appleton Laboratories in the UK showed possibilities of using an unmanned

undertrack altimeter transponder for tracking to ± 3 cm in vertical positioning (COMPASS Experiment).

VII. JOINT PROGRAMS

A. External

In the coming decade a number of oceanographic satellites with altimeters as part of the instrument payload are scheduled to be flown by non-DOD agencies and by foreign countries (e.g., ERS and TOPEX/POSEIDON). It should be expected that this global interest in remote sensing will continue into the Block 6 time frame. It is recommended that these satellites should be exploited for naval interests and that scheduling of DOD satellites should at least account for the presence of external satellites.

B. DOD.

Altimeters are becoming smaller in size, and power requirements are decreasing. It can be expected that major improvements in both areas will continue into the Block 6 time frame. For this reason, it will be highly feasible to include altimeters on polar-orbiting satellites without disruption of the primary missions.

VIII. SEA ICE

In addition to detecting and monitoring ocean mesoscale activity, it is important to note that meeting future naval tactical and strategic performance goals will require enhanced

capabilities of sea-ice monitoring. In this respect, the altimeter proved to be an exceptionally useful all-weather instrument. The all-weather capability is critical, particularly in polar and subpolar regions where ice and ocean meet and cloud cover is predominant. During the GOAP program, sea ice locations were generated along satellite nadir tracks. These locations were operationally transmitted to the Navy Polar Oceanography Center (NPOC), where they were incorporated into ice edge maps of the polar regions (Hawkins and Lybanon, 1989).

The presence of sea ice can be determined by the strength and shape of the returned altimeter signal. Over sea ice, this echo will be much more peaked than over the ocean. Simple parameters, such as the Automatic Gain Control (AGC) and Voltage Proportional to Attitude (VATT), which are generated for engineering purposes, were used to determine this peakiness with little additional effort. Although the contrast between sea ice and ocean returns of AGC and VATT can clearly be used to identify the ice edge, strong variability of these parameters and of the waveform itself has indicated that there is a much larger potential for recovering additional sea ice information in an operational setting.

Studies (Fetterer et al., 1990) have shown that even the simple AGC and VATT variations over sea ice off East Greenland can be used to distinguish meridional banding of the marginal ice zone, pack ice, and fast ice. In addition, advanced analysis techniques (Chase and Holyer, 1990) applied to the waveforms have

demonstrated good possibility of recovering ice coverage and ice type. Sensor Data Records from future altimeters should be designed to include simple parameterization of the waveforms for maximum extraction of sea ice information.

The relatively poor between-track resolution of satellite altimetry is a serious disadvantage to monitoring sea ice with a single instrument. However, this is mitigated in several ways. In an operational time frame, altimetry has been fused with AVHRR (cloud contamination problems) and passive microwave (limited resolution) to provide a synoptic picture of the ice. Although sea ice measurements are limited to altimeter nadir positions, in polar latitudes the convergence of ground tracks is such that horizontal resolution between tracks decreases considerably. In addition, multiple altimeter satellites soon will provide greatly enhanced coverage and additional opportunities to examine this underutilized resource for sea ice monitoring. Furthermore, it should be noted that the requirement for repeat orbits is not a necessary factor in sea ice sampling, except for the determination of freeboard.

To more effectively exploit the altimeter's ability to monitor sea ice, it will be important to fly the satellite to higher latitudes than those reached by the orbital inclination of SEASAT/GEOSAT. At 108 degrees inclination (72 degrees latitude) the GEOSAT altimeter could cover only the very southern parts of the Chukchi, Beaufort, East Siberian and Kara Seas, and along the East Greenland Coast to Davy Sound. The major portions of these

seas, as well as the Fram Strait and the principal ice-covered portions of the Barents Sea were unsampled. In contrast, the European Space Agency (ESA) satellite, ERS-1, will have an inclination of 98.5 degrees (81.5 degrees latitude). By flying at a higher inclination, ERS-1 will have the ability to sample these areas.

To better monitor sea ice in strategically and tactically important areas, it will be necessary to fly at higher orbital inclinations than maintained by SEASAT/GEOSAT. However, with higher inclinations, the accurate monitoring of western boundary currents (Gulf Stream and Kuroshio Extension) will be somewhat compromised. With low orbital inclinations, such as maintained by TOPEX/POSEIDON (63 degrees), the ascending and descending ground-tracks are nearly orthogonal at midlatitudes. This means that both meridional and zonal components of the currents will be resolved. In contrast, the ascending and descending ground tracks of ERS-1 are not orthogonal, and the meridional component of current will be poorly resolved (although total transport measurements, as well as the ability to locate rings, will be basically unaffected).

There is a tradeoff, then, in selecting orbital inclinations that enhance monitoring of sea ice and those which enhance monitoring western boundary currents. A compromise can be reached with multiple altimeters of different repeat periods as well as different orbital inclinations. Again, it will be necessary to simulate various scenarios to optimize sampling

strategies.

IX. GEOPHYSICAL CORRECTIONS

If we define altimeter precision as the ability to repeat a measurement, given the same environmental conditions, then a 5-cm precision level can probably be accomplished without difficulty. However, since we are also concerned about accuracy-- the ability to obtain absolute values-- then the whole area of geophysical corrections must be given some serious attention. Improvement in corrections for atmospheric water vapor content, ionospheric effects, and electromagnetic bias are needed to accurately establish the ocean topography with respect to a reference surface. Furthermore, improvements in corrections for ocean/earth tides and atmospheric pressure loading are needed to properly interpret the ocean topography in terms of dynamics. In the application of a systems approach, all geophysical corrections leading to the accuracy of the final product need attention before significant improvements can be achieved. The design and funding of future systems must consider corrections as important components of the system.

A. Wet Tropospheric Correction

Intervening atmospheric water vapor will tend to lengthen the measured range between the satellite altimeter and the ocean surface. This makes it possible for horizontal gradients in atmospheric water vapor content to be misinterpreted as oceanic SSH signals or causes oceanic SSH signals to be masked or

disoriented. On the global scale, Menaldo (1990) found that for altimeter-derived mesoscale circulation features of 10 cm or greater, water vapor is not generally a problem. Phoebus and Hawkins (1990), however, used near coincident SSM/I-determined water vapor measurements to estimate range corrections to GEOSAT altimetry in the Northeast Pacific. Range corrections of 15 to 20 cm over horizontal distances of 100 to 250 km were often found, which significantly altered the synoptic picture of mesoscale activity in this region. Timeliness of the water vapor data was of major concern, since the water vapor fields were associated with rapidly moving atmospheric fronts. Using water vapor data too far removed in time from the altimeter signals tended to introduce false signals into the SSH fields. To compensate for significant water vapor changes over small horizontal scales, it is strongly recommended that a bore-sighted, dual-channel, microwave radiometer be included on all satellite altimeters.

B. Ionospheric Corrections

In similar fashion to the problem of water vapor, the presence of free electrons and ions in the ionosphere reduces the propagation speed of the altimeter signal, lengthening range measurements between satellite and ocean. Because of its large spatial scale and because models are reasonably accurate, the induced error has a lessened impact on SSH estimates. However, inhomogeneous and rapidly varying ionospheric conditions associated with magnetic storms and solar flares can contribute 5 to 10 cm of error and should be taken into account (Musman et al., 1990).

C. Electromagnetic Bias

Because of the trochoidal shape of ocean surface gravity waves, the relative radar cross section (strength of return) of a roughened sea surface increases below mean sea level (troughs of waves) and decreases above it (crests of waves). Range measurements of satellite altimeters, then, are biased toward the wave troughs, rather than accurately picking up the mean sea level. In addition, a tracker bias occurs because of the difficulty in timing the leading edge of the pulse over a roughened sea. Corrections to these biases (Electromagnetic bias) are generally made as a percentage of the measured SWH (7%). Theoretical descriptions and experimental measurements have, so far, not given an adequate picture of this effect (Walsh et al., 1989). At small sea states, the correction may not be significant. However, as the sea state increases, the error may become pronounced. Comparisons of this correction with in situ measurements have shown an uncertainty level of about 1.2% of SWH (Douglas and Agreen, 1983). At large SWH, this becomes very important, especially since the interaction of waves with strong currents tend to alter wave height on the same horizontal scale as the current systems.

D. Tidal Corrections

Although tides in midocean are relatively small and fairly well modeled, evidence is accumulating that serious discrepancies are occurring in some regions-- especially in those areas associated with rapidly changing bottom topography and in

those areas associated with the conjunction of tidal amphidromes from different basins. Cartwright and Ray (1990) extracted the M2 tide (lunar semidaily) from GEOSAT data and determined that differences with the commonly used Schwiderski model of 10 to 20 cm were not unusual. Pistek and Johnson (1990) found that sharp peaks of 25 cm in tidal corrections over the Iceland/Faeroes Ridge were giving false indications of the Iceland/Faeroes Front (fig. 3). It is recommended that improved tidal models be generated with higher resolution (Schwiderski's model gives 1 degree resolution in latitude and longitude) and with the inclusion of tidal data extracted from GEOSAT.

E. Atmospheric Pressure Loading

The presence of an excess or a deficit of atmospheric mass above the sea surface induces an inverse response of sea level which can imitate (or create) ocean dynamics. A relationship exists of 1.01 cm of ocean deflection to 1 mbar of atmospheric pressure. The largest atmospheric pressure fluctuations of 40-50 mbars are caused by low pressure systems that propagate across oceans with local time scales of 1 to 2.5 days, creating the potential for SSH responses of 40 to 50 cm. However, the time and space scales of the storms are important to initiating a full response (Van Dam et al., 1990), and it is unclear how much of a pressure loading correction is needed. Considerably more effort in both theory and experiment are needed to properly correct this problem.

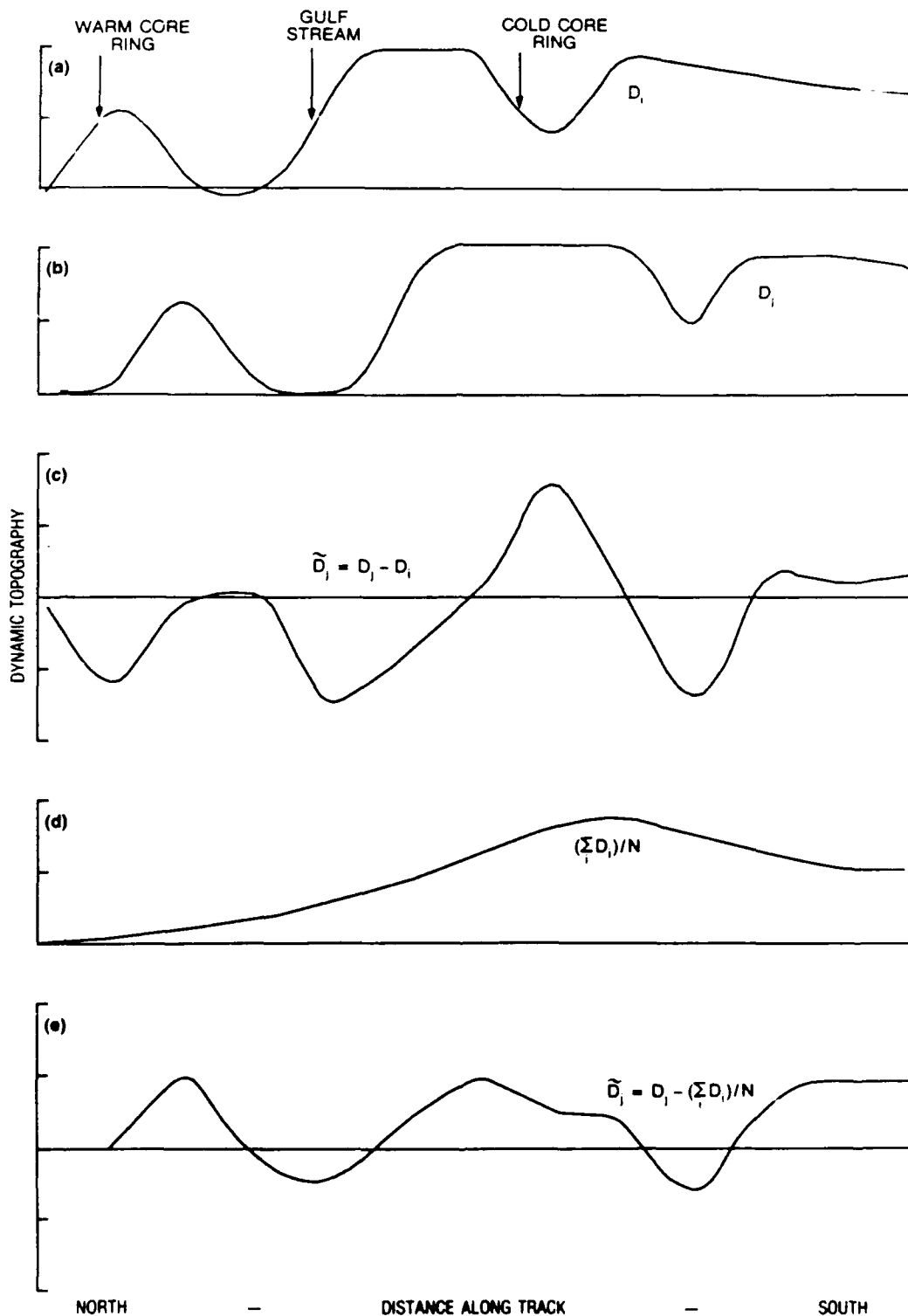


Figure 1: (a) Instantaneous dynamic topography at time index i .
 (b) Instantaneous dynamic topography at time index j .
 (c) Estimate of dynamic topography by subtracting contaminated geoid from instantaneous measurement.
 (d) Mean dynamic topography contribution to reference surface in collinear averaging technique.
 (e) Estimate of dynamic topography by subtracting reference surface derived by averaging collinear tracks.

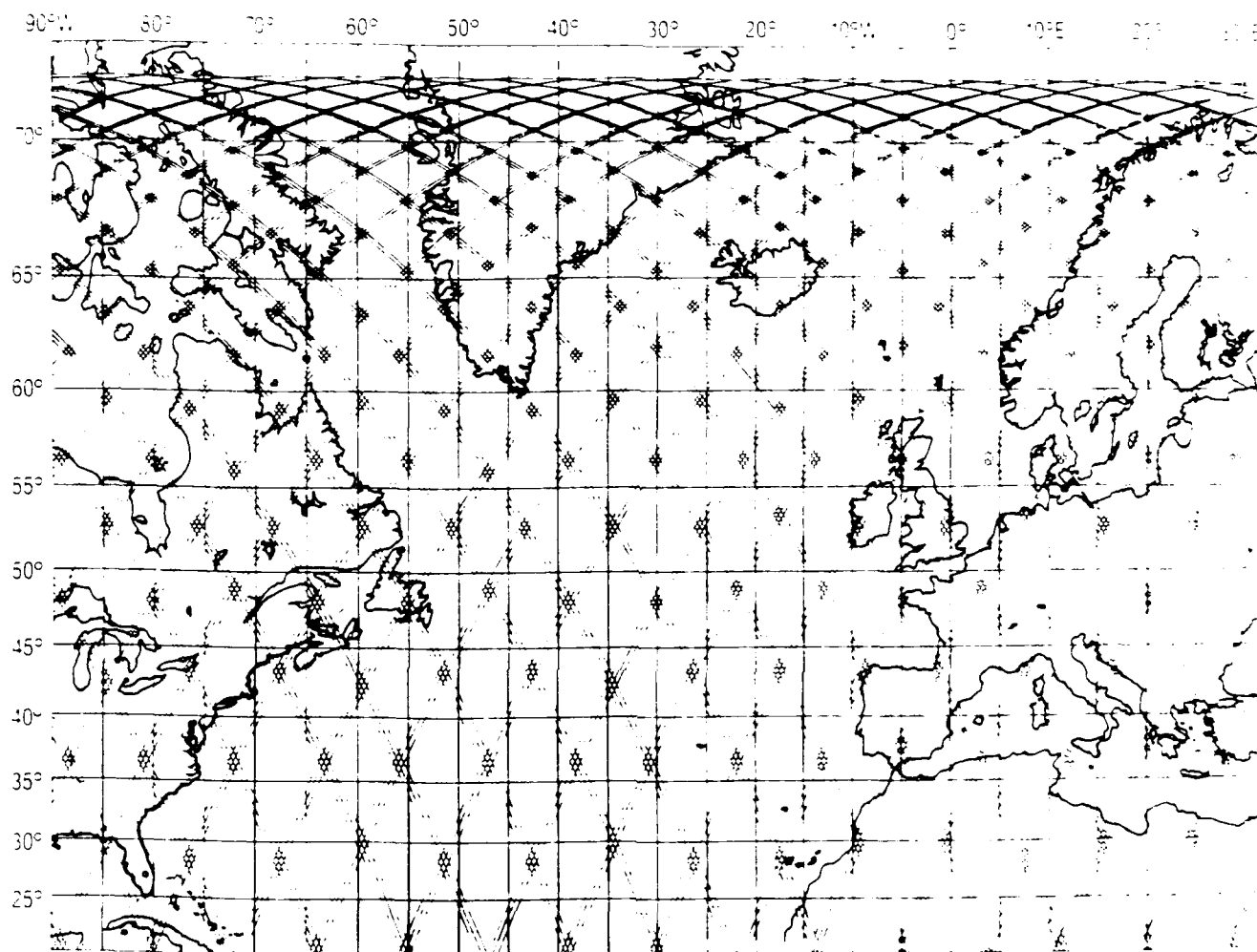


Figure 2: Near-repeat (3 day) ground-track pattern of three independent altimeter satellites. At the equator the separation is 50 km between adjacent tracks; at higher latitudes, where eddy sizes grow smaller, the track separation also decreases. This is in contrast to a multibeam altimeter with constant separation of groundtracks. Note the large gaps in coverage in midlatitudes.

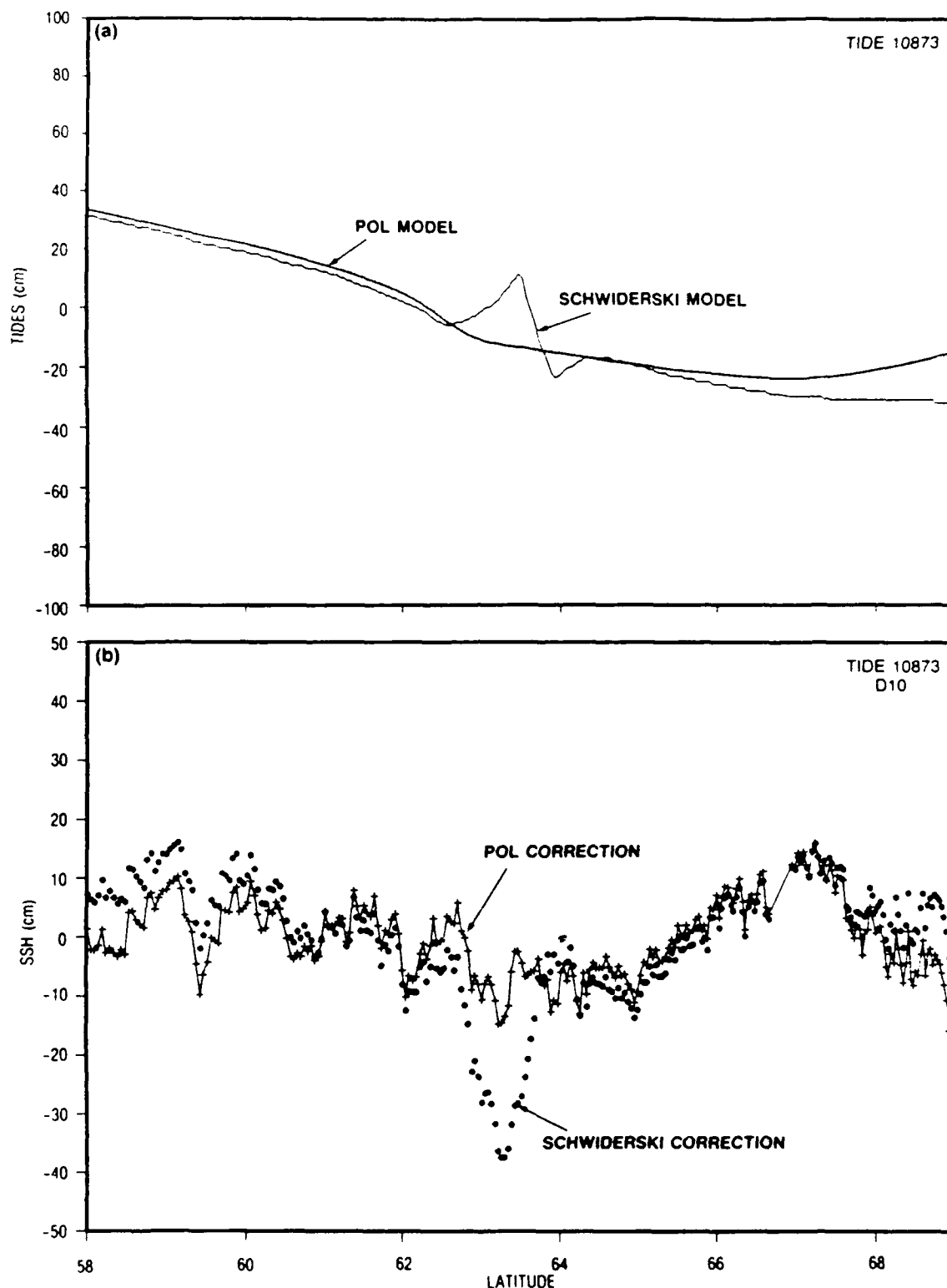


Figure 3: (above) Comparison of tidal height corrections using Schwiderski's model and the Proudman Oceanographic Laboratory's (POL) model. (below) Comparison of the correction effects of the two models on a GEOSAT SSH track descending across the Iceland/Faeroes Front. The front (from independent sources) occurs at about the same location as the false oceanographic feature (63.5 degrees) generated by the tide correction.

REFERENCES

- Brenner, A. C., C. J. Koblensky and B. D. Beckley (1990). A preliminary estimate of geoid-induced variations in repeat orbit satellite altimeter observations. J. Geophys. Res. 95, 3003-3040.
- Brown, G. S., L. S. Miller and L. W. Choy (1989). Multibeam radar altimetry: spaceborne feasibility and airborne experimentation. Naval Research Laboratory, Washington, DC, NRL report 9229.
- Cartwright, D. E. and R. D. Ray (1990). Oceanic tides from GEOSAT altimetry. J. Geophys. Res. 95, 3069-3090.
- Chase, J. R. and R. J. Holyer (1990). Estimation of sea-ice type and concentration by linear unmixing of GEOSAT altimeter waveforms, accepted by J. Geophys. Res.
- Douglas, B. C. and R. W. Agreen (1983). The sea state correction for GEOS-3 and SEASAT satellite altimeter data. J. Geophys. Res. 88, 1655-1661.
- Eisele, J. A. and G. V. John (1984). Orbital analysis of N-ROSS, Special Programs Office, Aerospace Systems Division, Naval Research Laboratory.
- Fetterer F. M., S. Laxon and D. R. Johnson (1990). A comparison of GEOSAT altimeter and Synthetic Aperture Radar measurements over East Greenland pack ice, accepted by IEEE J. of Remote Sensing.
- Hawkins, J. D. and M. Lybanon (1989). GEOSAT altimeter sea-ice mapping. IEEE J. of Oceanic Engin. 14, 139-148.
- Kelly, K. A. and S. T. Gillie (1990). Gulf Stream surface transport and statistics at 60 W from the GEOSAT altimeter. J. Geophys. Res. 95, 3149-3162.
- Kindle, J. C (1986). Sampling strategies and model assimilation of altimetric data for ocean monitoring and prediction. J. Geophys. Res. 91, 2418-2432.
- Menaldo, F. (1990). Path length variations caused by atmospheric water vapor and their effects on the measurement of mesoscale ocean circulation features by a radar altimeter. J. Geophys. Res. 95, 2923-2932.
- Mitchell, J. L. and G. H. Born (1984). A position paper: Mission design considerations for mesoscale oceanography with the N-ROSS altimeter, Naval Oceanography Research and Development Activity, Stennis space Center, MS, NORDA Technical Note 251.

Mitchell, J. L., J. M. Dastugue, W. J. Teague and Z. R. Hallock (1990). The estimation of geoid profiles in the Northwest Atlantic from simultaneous satellite altimetry and airborne expendable bathythermograph sections, J. Geophys. Res. in press.

Musman, S., A. Drew and B. Douglas (1990). Ionospheric effects on GEOSAT altimeter observations. J. Geophys. Res. 95, 2965-2968.

Phoebus, P. A. and J. D. Hawkins (1990). The impact of wet tropospheric correction on the interpretation of altimeter-derived ocean topography in the Northeast Pacific. J. Geophys. Res. 95, 2939-2952.

Pistek, P. and D. R. Johnson (1990). The Iceland-Faeroe Front: remote sensing and In Situ observations, in preparation.

Van Dam, T. M., J. M. Wahr and E. R. Benton (1990). Determining the atmospheric loading response of the oceans using GEOSAT ERM data. EOS 71 (2), p.127.

Verron, J. (1990). Altimeter data assimilation into an ocean circulation model: sensitivity to orbital parameters. J. Geophys. Res. 95, 11443-11459.

Walsh, E. J., F. C. Jackson, E. A. Uliana, and R. N. Swift (1989). Observations on electromagnetic bias in radar altimeter sea surface measurements. J. Geophys. Res. 94 (14) 575-14,584.

APPENDIX A: ACRONYMS

AGC	Automatic Gain Control
ASW	Anti-Submarine Warfare
AVHRR	Advanced Very High Resolution Radiometer
CNES	Centre National d'Etudes Spatiales
DMSP	Defense Meteoroloical Satellite Program
DOD	Department of Defense
EM bias	Electromagnetic bias
ERM	Exact Repeat Mission
ERS1	European Remote Sensing satellite number 1
ESA	European Space Agency
GEOSAT	Geodetic Satellite
GIN Sea	Greenland/Iceland/Norwegian Sea
GOAP	GEOSAT Ocean Applications Program
NASA	National Air and Space Administration
NOARL	Naval Oceanographic and Atmospheric Research Laboratory.
NPOC	Naval Polar Oceanography Center
NRL	Naval Research Laboratory
N-ROSS	Naval Remote Ocean Sensing System
OLS	Optical Line Scanner
PRARE	Precise Range and range Rate Experiment
SSH	Sea Surface Height
SSM/I	Special Sensor Microwave Imager
SWH	Significant Wave Height
TOPEX	Topography Experiment
VATT	Voltage proportional to Attitude

This page intentionally left blank

APPENDIX B: RELEVANT PUBLICATIONS

Operational Altimeter-Derived Oceanographic Information: The NORDA GEOSAT Ocean Applications Program

MATTHEW LYBANON,* RICHARD L. CROUT,** CONRAD H. JOHNSON* AND PAVEL PISTEK*

**Naval Oceanographic and Atmospheric Research Laboratory, Stennis Space Center, Mississippi*

***Planning Systems, Incorporated, Slidell, Louisiana*

(Manuscript received 23 February 1989, in final form 24 October 1989)

ABSTRACT

The U.S. Navy's GEOSAT active microwave altimeter provides detailed oceanographic and atmospheric information. It measures global oceanic wind speeds and significant wave height, sea ice edge in the polar regions, and dynamic topography related to mesoscale ocean circulation. The Naval Ocean Research and Development Activity processed near-real-time GEOSAT data to monitor oceanic processes from July 1985 to January 1989. We found that the combination of topographic information from GEOSAT, synoptic sea-surface-temperature information from infrared imagery, and local information from bathythermographs provides valuable information on Gulf Stream circulation. The size of the area involved, the intensity of currents, and the rapidity with which changes occur previously limited our technical ability to observe the Gulf Stream and its attendant spin-off eddies. Long-term study with the information sources described above has given a more complete picture of the Gulf Stream region's mesoscale circulation than ever before achieved.

1. Introduction

The Naval Ocean Research and Development Activity (NORDA; since 10 October 1989, NORDA has been the Naval Oceanographic and Atmospheric Research Laboratory) routinely prepared an analysis of mesoscale ocean features in the northwest Atlantic Ocean's Gulf Stream region from U.S. Navy GEOSAT (GEOdesy SATellite) altimeter measurements, infrared (IR) imagery, and in situ temperature data. The GEOSAT Ocean Applications Program (GOAP) provided the mesoscale analysis and three other types of altimeter-derived oceanographic information on a regular schedule for over 3 years, July 1985–January 1989, following several years of preparation. GOAP's purpose was to conduct an operational demonstration of the altimeter's usefulness to collect timely, accurate global environmental data, to process the data in near real time, and to transmit the products to the Navy's Fleet Numerical Oceanography Center (FNOC) for use in routine analysis and prediction of oceanographic parameters (Clancy 1987). As an operational demonstration GOAP was effectively a feasibility study, in which NORDA derived oceanographic information from GEOSAT altimetry and transmitted the results to a Navy operational environmental center on a quasi-operational schedule.

Altimetry is not as severely hampered by cloud cover

as IR imagery, and it also measures oceanographic phenomena which have no surface thermal expression. The topographic information that the altimeter provides can be used to detect oceanographic features whose surface thermal signatures are masked by atmospheric effects (e.g., water vapor) or covered by clouds. Another source of difficulty with IR imagery is that the warming of the ocean's surface layer during spring and summer tends to obscure cold-core rings south of the Gulf Stream. Altimeter measurements frequently increase the amount of detail in mesoscale analyses when they are used to supplement IR imagery as an information source. NORDA produced two mesoscale analyses per week during GOAP. The GOAP mesoscale analyses were incorporated into the FNOC system (Clancy 1987) and provided to a Navy regional oceanographic center.

GOAP also provided daily global information on surface wind speed and significant wave height, and sea ice edge in both the Arctic and Antarctic regions. All three of these "product" types have substantially increased the amount of information available to the Navy on these oceanographic parameters. GEOSAT only has one ground station, which restricts the number of times per day data can be received. This, in turn, severely limits the quantity of wind and wave data timely enough to be used in FNOC analyses. However, retrospective studies have shown that the information has the potential to be of value (e.g., Pickett et al. 1987). The sea ice edge information produced has been used routinely (Hawkins and Lybanon 1989). This paper describes the production of all four types of oceanographic information from GEOSAT altimetry, but will

Corresponding author address: Dr. Matthew Lybanon, GEOSAT Ocean Applications Program, Department of the Navy, Naval Oceanographic and Atmospheric Research Laboratory, Stennis Space Center, MS 39529-5004.

concentrate primarily on mesoscale feature analysis. The latter sections of the paper discuss interpretive techniques, give examples of the information that altimetry contributes to the analysis, and present some conclusions drawn from the 3-year GOAP analysis results. In particular, section 5b gives Gulf Stream position information derived from the GOAP mesoscale analyses.

2. Background

GEOSAT was built by the Johns Hopkins Applied Physics Laboratory (APL) and launched on 12 March 1985, into an 800-km altitude, 108-degree inclination orbit. The initial orbit generated a ground track pattern that almost repeated every 3 days, and had an average ground track spacing of 4 km at the equator by the end of the 18-month-long primary mission (McConathy and Kilgus 1987). The satellite carries a single instrument, a 13.5 GHz nadir-looking radar altimeter similar to the SEASAT altimeter in its mechanical, thermal, and electrical interfaces, but with some engineering changes intended to extend its lifetime and reduce its noise level (MacArthur et al. 1987).

GEOSAT's primary mission was to provide the dense global grid of altimeter data required to improve knowledge of the earth's gravitational field. Collection of altimeter data for oceanographic and meteorological investigations was the secondary mission during the first 18 months of GEOSAT, but it became the primary mission thereafter. The Oceanographer of the Navy formulated GOAP, an oceanographic analysis program, to increase the overall value of the GEOSAT data. After over 3 years of successful operation, NORDA transitioned GOAP to operational status at the Naval Oceanographic Office (NAVOCEANO).

On 1 October 1986, APL began maneuvers that placed the spacecraft into a 17-day exact repeat orbit optimized for collecting oceanographic data. The subsequent GEOSAT Exact Repeat Mission (ERM) was designed so that long-term, along-track averaging could give an accurate local mean sea surface, and minimize the errors that occur when an imperfectly known marine geoid is subtracted from the altimeter data to produce mesoscale dynamic topography. The ascending nodes of the exact repeat orbit are approximately at $1.004 + n(1.4754)^{\circ}\text{E}$ longitude, where n is an integer between 0 and 243. Thus, the ground track is a network that repeats every 244 revolutions, with a spacing of about 120 km in the Gulf Stream region. The orbit is adjusted as necessary to maintain this pattern laterally within less than 1 km. The ERM began on 8 November 1986.

3. GOAP processing

a. Data system

The altimeter transmits 1020 pulses per second and measures the return waveforms. Averaging aboard the spacecraft reduces the data rate by a factor of 100, so

measurements are transmitted to the ground at a rate of approximately 10 per second. The APL ground station receives the data approximately every 12 hours and produces NORDA Data Records (NDRs), which contain measured range, significant wave height, wind speed, and automatic gain control (all except wind speed at a 10-per-second rate), plus mode and data quality flags, and corrections for satellite and instrument errors. APL promptly transmits the NDRs to NORDA over a 9600-baud dedicated telecommunication circuit. During GOAP NORDA derived oceanographic products from the NDR data and transmitted them to FNOC over a similar circuit, using the standard Data Exchange Formats endorsed by the Federal Coordinator for Meteorological Services and Supporting Research (U.S. Dept. of Commerce, NOAA, 1982).

Both telecommunication links used 9600-baud, dedicated telephone lines but different communication protocols. The NORDA-APL line used an IBM binary synchronous protocol with line control software written by APL. The hardware interface was based on the Gould Systems Engineering Laboratories Model 9116 Binary Synchronous Line Interface Module. The NORDA-FNOC line used the X.25 protocol. NORDA's computer was interfaced to that line via a ComDesign TX-700 X.25 Packet Assembler Disassembler.

NORDA's GOAP information processing system hardware consisted of two Gould Systems Engineering Laboratories 32/27 32-bit minicomputers with associated peripherals, including International Imaging Systems (I²S) image processing hardware. The software had four types of elements: communications and file management, real-time processing, objective processing, and interactive processing.

The first element performed line-control functions for the two data links and transferred files between disks and the telecommunication lines. The second produced the scalar wind, significant wave height, and ice edge products. The third involved such functions as earth location, land/sea determination, bad point editing and averaging, geophysical corrections, height residuals calculation, etc. The fourth covered operations used in the subjective generation of the mesoscale product (discussed in a later section). That element was primarily comprised of I²S System 575 software, a proprietary interactive command interpreter with an associated image processing library designed to operate with I²S Model 75 hardware.

Quality control was an important part of the processing to derive the oceanographic products. Some quality-control tests checked "flags," i.e., one-bit indicators. The NDR contains two types: mode flags and data quality flags. A mode word, made up of three status/mode words from the spacecraft's telemetry stream, contains the mode flags, which indicate the altimeter's operational status, details about its acquisition of the return signal, etc. The data quality flagword contains the results of tests performed during ground

processing at APL, which determine the statistics and "reasonableness" of measured and calculated quantities (Cole 1985).

The quality control checks that were performed for all products are status flag, mode word, missing data, and time checks.

Status flag check. Each GEOSAT record (approximately 5 s of data) in the NDR has an associated status flag, which tells whether the data have been received by APL, and whether the data have been sent to NORDA. (The NDR is a direct-access file, which is not necessarily filled in time order.)

Mode word check. Each GEOSAT subrecord (approximately 1 second of data) contains the mode word described above. Data were considered good when the flags indicated that GEOSAT was in the proper operational mode and valid data was received.

Missing data check. The data quality flagword in each subrecord consists of 27 flags. The flags were checked for the presence or absence of height, significant wave height, and automatic gain control (AGC) values.

Time check. Each NDR contains data for 1 day, nominally to within less than a second. The NDR provides two sets of time tag data, which are used to compute time for each GEOSAT subrecord. The time per frame was obtained by differencing the two time tags. This time must be within 0.001 s of 0.098 s per frame. If the 0.001 s variance condition was met, the time for the start of day of the NDR was computed using the start frame count. The start time had to be within 60 s of the start of day (UTC) for the NDR to be processed.

b. Oceanographic parameters

1) SCALAR WIND SPEED AND SIGNIFICANT WAVE HEIGHT

The change in the microwave signal's surface reflectivity due to the wind-driven surface roughness provides an altimetric estimate of surface scalar wind speed. The algorithm employed at APL (Brown et al. 1981) is

$$W = \exp[(S - B)/A], \quad (1)$$

where

$$S = 10^{-(\sigma^{\circ} + 2.1)/10}, \quad (2)$$

In these equations,

- W = wind speed at 10 meters above the ocean surface,
- σ° = radar backscatter cross section,
- A, B = constants for 3 different σ° ranges.

The σ° is inferred from the altimeter's AGC signal. The complete Brown algorithm is a two-stage procedure. Equations (1) and (2) define the first stage. The

second stage calculates an improved wind speed estimate, a fifth-degree polynomial function of the W given by Eq. (1). The latter calculation compensates for skewness in the distribution of the difference values between buoy- and altimeter-measured wind speed (Brown et al. 1981). The estimate of backscatter is highly sensitive to an off-nadir pointing error; consequently, such an error would corrupt the wind speed estimate. A separate calculation corrects backscatter for the off-nadir pointing error (Cole 1985), prior to its use in Eq. (2). That calculation makes use of a parameter called VATT, which is described in the ice index discussion. The off-nadir correction to backscatter effectively corrects wind speed for pointing errors.

The reflecting surface modulates the transmitted pulse. More specifically, ocean waves stretch the return waveform's leading edge, so that its slope provides an estimate of significant wave height (SWH); higher waves produce smaller slopes. The SWH calculation is performed aboard the GEOSAT spacecraft and the results are transmitted to the ground station.

APL calculates both wind speed and wave height. During GOAP NORDA edited the values for data quality, averaged the wave height values to a once-per-second rate (APL supplies wind speed at that rate), put the resulting edited, once-per-second wind and wave values into a wind-wave record, and transmitted them to FNOC. FNOC uses the GEOSAT wind speed data in their marine wind analysis, while the significant wave height data are an input to the FNOC visual sea height analysis.

Dobson et al. (1987) compare GEOSAT wind speed and significant wave height measurements to in situ observations. Their overall conclusion is that the wind speed measurements agree within 1.8 m s^{-1} and wave height measurements agree within 0.49 m. Monaldo (1988) discusses two related topics: What are the expected differences between buoy and altimeter estimates of these quantities, and what conclusions can be drawn about the capacity of an altimeter to measure them.

NORDA applied several special data quality checks to the wind speed and wave height values. The data quality flagword was checked for height, AGC, and SWH standard deviations out of bounds. Also, there was a check of the "VATT not available" flag. These flags indicate problems with the wind or wave data in the subrecord. A least-squares fit of a straight line was performed on the SWH data that passed the prior data quality checks. Then, any SWH value more than two standard deviations from the fitted line was marked bad in the processing software's internal data quality flags.

2) SEA ICE EDGE

The return pulses from sea ice have a significantly different shape than returns from the ocean (Eppler

1982). Dwyer and Godin (1980) developed a semi-empirical algorithm for the GEOS-3 altimeter that measures those differences. That algorithm, as modified for GEOSAT, is

$$\text{index} = [(100 + \text{AGC}) / (100 \times \text{VATT})], \quad (3)$$

where

AGC = automatic gain control signal.

VATT = "voltage" proportional to attitude (dimensionless)

$$\text{VATT} = [(\text{ATTG} - \text{ATTGE}) / (\text{AGCG} - \text{ATTGE})], \quad (4)$$

and the intermediate quantities are functions of the 60 basic return pulse waveform samples [the sample indexing is the same as for the SEASAT altimeter (MacArthur 1978)]

ATTG = mean of last 8 samples.

ATTGE = mean of first 8 samples.

AGCG = mean of center 48 samples (not including the track point gate).

This "ice index" is a number in the range of 0.6–0.7 over water and is greater than 1 over ice. (That threshold is based on a prelaunch simulation that used SEASAT data.) So, water–ice transitions are evident in the ice index's time history.

As in the case of the other oceanographic products, the ice products are based on 1-second average values of altimeter-derived quantities. NORDA provided alphanumeric ice index data files for both the Northern and Southern hemispheres. In addition, NORDA prepared daily ice index plots and transmitted them to the Naval Polar Oceanography Center (NPOC) via FNOC (Hawkins and Lybanon 1989). The graphic products are the same size and projection as NPOC's other working charts, which facilitates their use. Figure 1 shows a sample ice index graphic product.

The graphic products show ice index profiles over water, with the satellite's nadir tracks as base lines (Hawkins and Lybanon 1989). Their interpretation to delineate water–ice transitions is suggested above. The point along a ground track where the ice index rises above the threshold clearly indicates the ice edge. The threshold value was modified from 1.0 to 0.9 after NORDA and NPOC gained experience in interpreting GEOSAT ice index data. NORDA is continuing research efforts designed to extract more information from the ice index.

NORDA performed two data quality checks during the ice index processing. A least-squares fit was used to eliminate AGC outliers, as was done for SWH data. Also, VATT values less than 0.0 or greater than 2.2 were excluded.

3) SEA SURFACE HEIGHT MEASUREMENT

The radar altimeter measures the distance from its antenna's electrical center to the instantaneous sea

surface as averaged over the footprint. The effective (pulse-limited) footprint is a function of significant wave height. The footprint's radius is

$$r = \sqrt{h} c \tau' \quad (5)$$

where h is the satellite's altitude, c is the speed of light, and the effective pulse duration τ' is

$$\tau' = \left[\tau^2 + \left(\frac{H^2}{c^2} \right)^{1/2} \right] \quad (6)$$

In Eq. (6) τ is the pulse duration (3.125 ns for GEOSAT) and H is wave height. GEOSAT's footprint diameter is 1.7 km for a perfectly flat sea, increases to 2.1 m for 1-m waves, 4.0 m for 5-m waves, and 5.6 m for 10-m waves. [Brooks et al. (1978) provide a helpful diagram and the correct equation for flat seas. For rough seas the pulse duration is replaced by the effective pulse duration of Eq. (6).]

Sea level is the difference between the altimeter-measured distance and the satellite's height, where the latter is determined independently by tracking and orbit determination. (Orbit height is normally referenced to a standard "reference ellipsoid"; consequently, so is sea level.) Then, the difference between sea level and the geoid, the sea surface height (SSH) residual, provides information on ocean dynamics.

The GEOSAT altimeter provides dense, all-weather range measurements along the satellite's nadir track with 3.5-cm precision (MacArthur et al. 1987) and an average white-noise level of about 8 cm (Sailor and LeSchack 1987). Conversion to SSH residuals requires orbital calculations (both for earth location and satellite height determination), correction for orbit error and other geophysical error sources, and removal of the geoid or other reference surface. Lybanon and Crout (1987) discuss the error sources and provide estimates of their magnitudes.

NORDA performed one data quality check specifically for SSH processing: A least-squares fit was used to eliminate altimeter height word outliers, as was done for SWH and AGC (the latter during ice processing) data.

Available "geoids" are not true geoids; they contain errors. These geoids generally include information derived from altimeter data, taking advantage of the fact that the long-term temporal mean of altimeter-derived sea level is approximately the marine geoid. (The ERM's repeat orbit provides the opportunity to use along-track ensemble means as reference surfaces for the SSH computation. In some areas these are the best "geoids" available.) However, that mean also includes the time-independent part of the dynamic topography. The presence of this contaminating term significantly interferes with interpretation of the SSH residuals.

It is impossible to separate this part without independent information. The construction of so-called "synthetic geoids" by removal of the mean oceanography contamination is a topic of considerable current interest. Kilgus (1989) reports on several synthetic

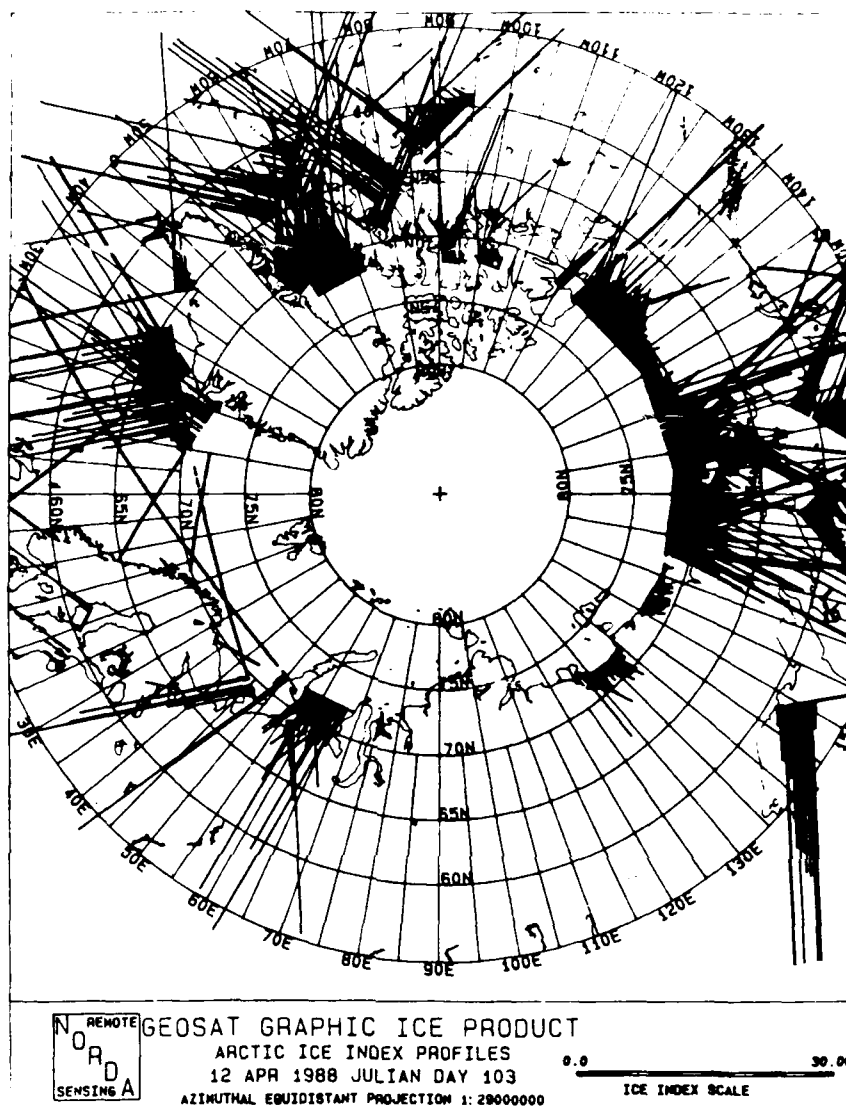


FIG. 1. Sample GEOSAT ice index graphic product. Ice index values are plotted along GEOSAT ground tracks. Ice edge crossings are clearly apparent.

geoid methods (detailed descriptions have been submitted for publication by the researchers), all of which introduce additional information to achieve the separation. Tapley et al. (1988) describe a different approach which uses altimeter data, tracking data, and surface gravity data to solve simultaneously for the sea surface topography, the Earth's gravity field, the satellite's orbit, and other parameters.

Figure 2 illustrates the problem. The dashed line in Fig. 2a shows an idealized mean Gulf Stream height profile, which is often present as a geoid error. The three solid lines are instantaneous Gulf Stream SSH profiles as they would appear if they could be calculated without error. The mean is "smeared" because of the Gulf Stream's meandering while the altimeter data incorporated in the geoid were collected, and possibly because of filtering used in the geoid's construction.

The mean Gulf Stream's amplitude is shown as less than that of the instantaneous Gulf Stream profiles, another possible effect of the filtering. The three instantaneous profiles include one north of, one coincident with, and one south of the mean Gulf Stream's position. Figures 2b, 2c, and 2d show the result of differencing the instantaneous and mean profiles, as in the subtraction of the "contaminated" reference surface from sea level. In general, both the resulting profile's shape and, to a smaller extent, its position are affected. (Although it is not apparent from the plots, the amplitude of the variation in Fig. 2c is smaller than that for the other two.) Several NORDA efforts are in progress to account for and correct the geoid error caused by the presence of mean oceanography. Kilgus (1989) describes preliminary results from some of them.

An added benefit can result from performing this

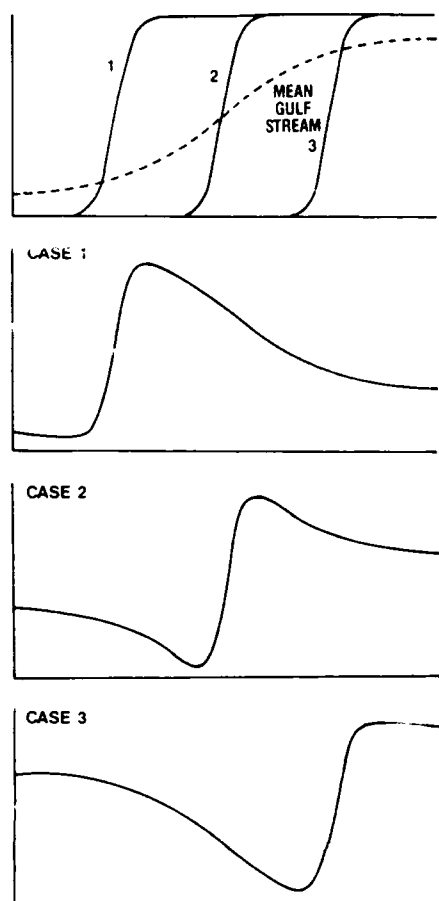


FIG. 2. Effect of mean oceanography in reference surface upon SSH residuals. Subtraction of reference surface induces error in residuals. (Top) Mean Gulf Stream profile and 3 instantaneous ideal (error-free) Gulf Stream SSH profiles. (Case 1) Difference, instantaneous Gulf Stream north of mean Gulf Stream. (Case 2) Difference, instantaneous Gulf Stream coincident with mean Gulf Stream. (Case 3) Difference, instantaneous Gulf Stream south of mean Gulf Stream.

correction. It is at least plausible that the more accurate SSH profiles that result should permit the calculation of reasonably accurate geostrophic velocity values. Kelly and Gille (1990) found this to be the case. They describe a simple method for estimating the mean dynamic topography, which they use in the calculation of the absolute surface geostrophic velocity and transport. Their estimates are consistent with other measurements.

During most of the GOAP demonstration NORDA used orbits calculated by the Naval Space Surveillance System (NAVSPASUR). NAVSPASUR received tracking data from the Defense Mapping Agency's TRANET system and calculated a special set of short-arc solutions, each valid for a particular track through the GOAP mesoscale test area. These orbits had a radial position uncertainty of about 10 to 20 m, and were available promptly enough for the near-real-time GOAP analysis. More recently, orbits with a radial position uncertainty of approximately 3 m, which were

calculated by the Navy Astronautics Group, became available.

Simple linear detrending was adequate to reduce the residual orbit error to the centimeter level for the relatively short tracks (2000 km or less) through the GOAP mesoscale test area. To a good approximation, the orbit error is sinusoidal with a period equal to the orbital period. It is not quite adequate to expand the sinusoid in a Taylor series and look at the magnitude of the first term beyond the linear term to estimate the residual error, because there is also a phase angle, i.e., the 2000-km segment may be any (small) "piece" of the sinusoid. However, a simple computer simulation shows that for 10–20 m orbit errors, the mean rms error after removing a straight line is under 5 cm. A slightly different analysis shows that the maximum value of the residual nonlinear error is 1.2 cm per meter of orbit error.

This "tilt and bias correction" simultaneously took care of the other long-wavelength errors that affect the mesoscale analysis. Ocean tides, electromagnetic (EM) bias, and the wet tropospheric pathlength correction were addressed explicitly, because they have significant energy at mesoscale wavelengths.

Tides were calculated from the Schwiderski model (Schwiderski and Szeto 1981), which has an accuracy of 10 cm or better over open ocean. EM bias, an apparent shift in sea-surface elevation caused by a difference in strength of the reflection from the troughs and crests of ocean waves, can be modeled adequately as a range error proportional to significant wave height. The altimeter's electronic tracker is responsible for a similar bias; GOAP used a combined correction factor of 5 percent of significant wave height (Born et al. 1982). MacArthur (APL, private communication, 1989) thinks that 5 percent is a reasonable value.

The tropospheric water vapor pathlength error may have a magnitude of 25 to 30 cm, and a local (i.e., in the mesoscale range) variability of 10 to 20 cm (Hawkins and Smith 1986). NORDA's processing software provided for this correction, although no good means of determining it was available during the GOAP operational demonstration. Because the mesoscale topographic signals of interest in the Gulf Stream region are of the order of 50–100 cm, a major impact on the location of mesoscale features was not expected, and not observed very often. NORDA is now using a correction based on observations from the recently launched Special Scanner Microwave Imager (SSM/I) radiometer. Algorithms to calculate an SSM/I wet troposphere correction were developed by J. Hollinger (1980). Tapley et al. (1982) showed that the water vapor correction based on SEASAT Scanning Multichannel Microwave Radiometer (similar to SSM/I) measurements was realistic. Phoebus and Hawkins (1990) discuss the significance of the water vapor correction (calculated from SSM/I measurements) in the northeast Pacific Ocean, where the oceanographic signals are much smaller.

4. Mesoscale analysis

a. Background

NORDA prepared a description of Gulf Stream region mesoscale ocean features beginning in the fall of 1985, first at 10-day intervals and later twice each week. This was a logical continuation of work begun in the 1970s by NAVOCEANO scientists, who studied the Gulf Stream and rings and published results in the *Gulf Stream Monthly Summary* and later in *Gulf Stream* (1975–1981). The latter publication has since been replaced by the *Oceanographic Monthly Summary*. Maps based on satellite image analyses, which show the positions of the Gulf Stream and rings, have also been produced weekly by the Naval Eastern Oceanography Center (NEOC) and several times a week by the National Oceanic and Atmospheric Administration (NOAA). GOAP's important contribution was the introduction of the altimetric signal into the interpretive process. Altimetry's advantages are all-weather capability and close connection of the measurement with ocean dynamics, as discussed in Section 3b(3). The GOAP analyses covered the area outlined in Fig. 3, and provided information of operational use to the Navy. Recently, eddy-resolving regional models for the Gulf Stream were developed (Robinson et al. 1988), and comparisons between the two outputs and analyses of the differences are being studied. GEOSAT data are being used to test and refine them.

Cheney and Marsh (1981) verified the presence of dynamic ocean features in SEASAT altimeter profiles. Cheney (1982) combined 2 weeks of satellite IR imagery, bathythermograph (BT) data, and drifter tra-

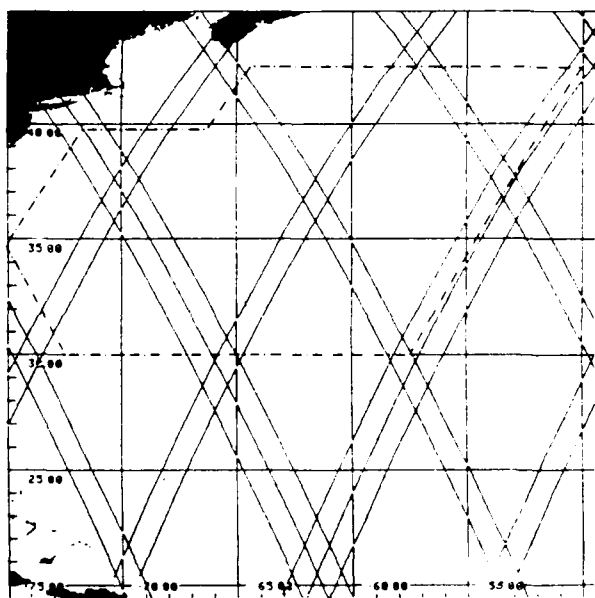


FIG. 3. Area covered by GOAP mesoscale analyses, outlined by dashed line, plus 7-day satellite ground track laydown (from first 18 months of GEOSAT mission).

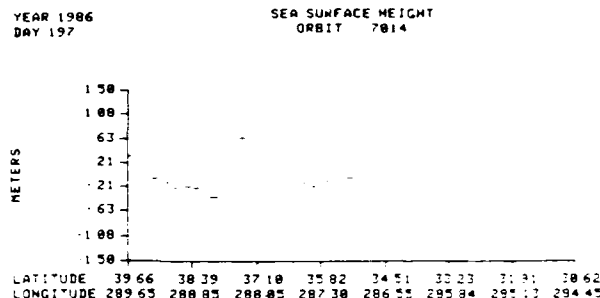


FIG. 4. Sea surface height residual for GEOSAT orbit 7014, a descending pass, showing the Gulf Stream signature between 37°S and 38°N.

jectories into Gulf Stream region mesoscale feature maps. These maps were compared to SEASAT altimeter profiles to determine the altimeter data's usefulness in finding the mesoscale features. Based on the successful results of these comparisons, NORDA took the analysis one step further. Latitude and longitude positions of the north and south walls of the Gulf Stream and of ring centers and edges, from altimeter SSH residuals, were combined with 3 to 4 days of IR imagery and 1 week of expendable bathythermograph (XBT) data to produce a mesoscale map of the Gulf Stream twice weekly. This map, referred to as the GEOSAT mesoscale map, was produced starting in September 1985.

SEASAT altimeter data showed that the Gulf Stream and its associated rings display a topographic signal of approximately 0.5 to 1.0 m (Cheney and Marsh 1981). Nevertheless, it is difficult to interpret altimetric signals in the Gulf Stream area. This portion of the paper discusses some of these difficulties, describes the steps in the preparation of mesoscale maps, and shows some preliminary statistical results derived from them.

b. Features

The Gulf Stream alone is a complicated oceanographic feature whose investigation goes far back into the last century. Stommel's book, *Gulf Stream* (1965), one of the classics of oceanographic literature, summarizes earlier works and started an era of new investigations. Satellite IR imagery immensely enhances the understanding of the Gulf Stream's complexity. Altimetry provides the means for identifying its location, and shows promise for giving more detailed and quantitative information concerning the mesoscale flow field. Figure 4 shows the altimetric signal across the Gulf Stream. The figure plots the SSH residual, the difference between sea level and the geoid, after corrections, as described in Section 3b(3).

Gulf Stream rings are a vital component of the Gulf Stream system. A ring is a special type of eddy that forms from a cut off Gulf Stream meander (Stommel 1965; Fuglister 1972; Richardson 1983). Rings are among the most energetic eddies in the ocean, and

their thermocline displacements, swirl speeds, and volume transports are nearly equivalent to the Gulf Stream's. They change their shapes and positions, sometimes rapidly, and interact with the Gulf Stream and other rings. They generate mean flow and are vital in transporting different water masses across the Stream (Newton 1961; Cheney and Richardson 1976).

c. Cold-core rings

Fuglister (1972) and Doblar and Cheney (1977) describe the creation of cold-core rings (CCRs). A CCR consists of a closed segment of the Gulf Stream that swirls cyclonically around a cold slope water core. Due to their initial surface temperature distribution, newly formed rings can be observed in satellite IR imagery. Richardson summarized their properties (1983). A new CCR is elliptical but becomes nearly circular as it moves away from the Gulf Stream. Typical diameters are 150 to 300 km. SEASAT altimeter observations showed that CCR sea surface depressions are approximately 0.5 to 1.0 m (Cheney and Marsh 1981). Figures 5, 6, and 7 show examples of the GEOSAT altimetric cold ring signals. Satellite ground tracks serve as baselines for the SSH plots.

Figure 5 shows the altimetric signal's all-weather advantage over IR images: both ascending tracks (year days 119 and 122) show the presence of a large (200-km diameter) CCR invisible in the IR, hidden under cloud cover. The ring is marked as "A" in the figure. Ring A appears in the IR satellite image from 4 days later (Fig. 6), and is intersected by year day 123's descending track. The "young" CCR shows a very symmetric 80-cm depression with the swirl velocity increasing with distance from the center. The SSH gradient indicates a surface velocity maximum of 200 cm s^{-1} 60 km from the center, with a dropoff farther from the center. This agrees with in situ observations (Olson 1980).

In the ring's central part, the near-surface rotation period is about 2 days. It is important to notice the ring's extent. Gulf Stream and Sargasso Sea waters are entrenched into the ring, while the cold slope water, visible as a light-colored center, has a diameter of only 80 km. An "older" CCR, ring B, is visible in Fig. 6 in the lower center of the IR image, and it is partly visible in Fig. 7. Infrared imagery indicates that this ring did not move during this 10-day period. It was crossed by an ascending altimeter track on year day 133. That SSH profile shows a 40-cm depression and a 150-km diameter, with maximum surface current speed of 100 cm s^{-1} .

Cold-core ring interactions with the Gulf Stream fall into two categories (Richardson 1983). In the first the ring reattaches to the Gulf Stream. The ring center opens to the north of the Gulf Stream, and an open meander is created. Later, this ring is completely absorbed by the Gulf Stream. In the second category a "nonfatal" interaction occurs when a ring becomes at-

tached to the Gulf Stream, moves downstream, and detaches from the Gulf Stream to form a modified ring.

Figure 8 shows an interaction of the first type. Part of the Gulf Stream is still visible in the altimeter signal north of ring C. The altimeter track on year day 73 crosses the ring, and a large, slightly asymmetric dip in the altimeter data (150 cm) is clearly visible. Figure 9 shows the altimeter data in detail (upper plot) with the corresponding geostrophic velocity profile (lower plot). Geostrophic velocity was computed from SSH data using a finite-difference approximation to the derivative. The SSH data were first filtered by a median filter (Gallagher and Wise 1981). Figure 9 also shows the importance of accounting for centrifugal force in the geostrophic velocity computation. The solid-line curve in the lower plot was obtained by a straightforward geostrophic calculation, while the dashed-line curve shows the velocity obtained by including centrifugal force.

d. Warm-core rings

Warm-core anticyclonic rings form (by pinching off) from the Gulf Stream throughout the slope water in a region bounded by the Gulf Stream and the continental slope. Their diameters are around 100 km. A warm-core ring (WCR) consists of an annular area of Gulf Stream water surrounding a Sargasso Sea core (Gotthardt 1973; Bisagni 1976; Lai and Richardson 1977; Halliwell and Mooers 1979).

WCRs move westward with a mean speed of 5 cm s^{-1} , which is the mean slope water flow speed, and as they drift westward they gradually shrink in size. They interact very often with the Gulf Stream, sometimes separating, sometimes coalescing with it. They entrain the slope water and sometimes the shelf water, and advect it around and into the Gulf Stream (Morgan and Bishop 1977). When WCRs reach Cape Hatteras, they coalesce with the Gulf Stream (Gotthardt and Potocsky 1974). An interdisciplinary study of WCRs was carried out in 1981 through 1985; results are published in *JGR: Warm-Core Rings Collection* (1985).

Figure 5 shows a WCR (ring D) interacting with the Gulf Stream. A large amount of Gulf Stream water is entrenched into the ring. An ascending altimeter track that crossed this WCR 3 days before this IR image was taken shows the warm ring extending about 150 km with a 50-cm altimeter signal. The second WCR visible in this IR image is ring E, which is clustered near 40°N , 65°W . Figure 6 shows ring D as a very compact warm ring which redeveloped 4 days after interaction with the Gulf Stream. No altimeter track crossed this WCR until year day 131, 5 days later. That track, which intersects one edge of ring D, shows a large signal, almost 80 cm, that indicates the spinoff after interacting with the Gulf Stream. (The day 131 altimeter track is cut off at the northern edge of the GOAP region, so it does not completely cross the ring.)

Similarly, Fig. 6 shows ring E visible in an ascending

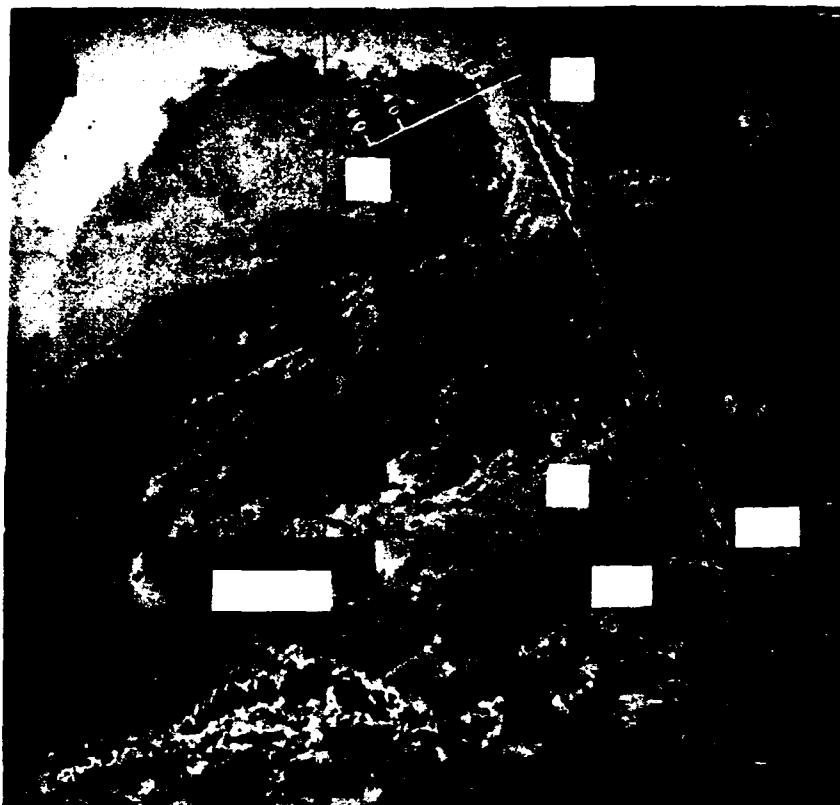


FIG. 5. Altimeter data superimposed on IR image from 2 May 1986. Ascending tracks through GOAP area from day 119 (29 April) and day 122 (2 May) cross a CCR (A) and the Gulf Stream. The altimeter data indicates that the CCR is larger than it appears in the IR image. The day 119 track also crosses a WCR (D).

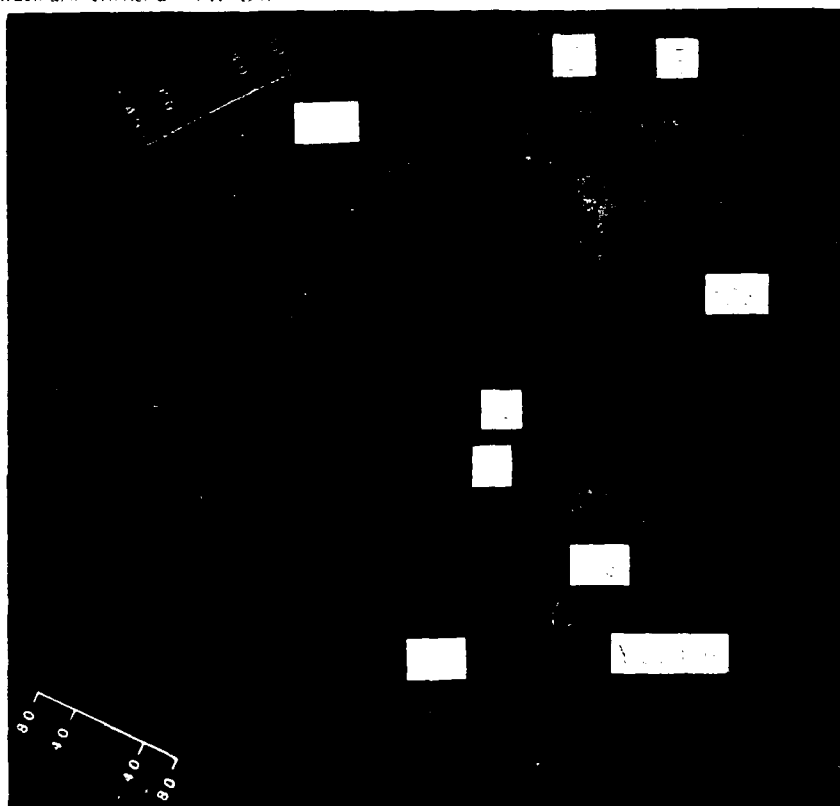


FIG. 6. Image 4 days later with four GFO SVP tracks superimposed. The altimeter tracks cross the Gulf Stream, two CCRs, and two WCRs that are also visible in the IR image. The SSH data provides additional information on the sizes and strengths of the features.

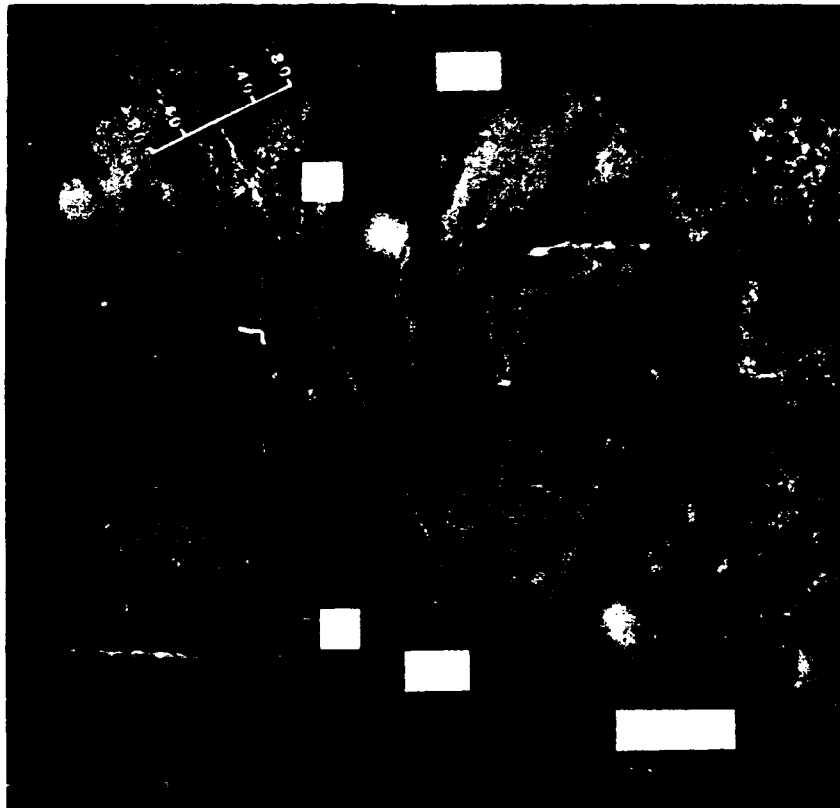


FIG. 7. Image 10 days later with GEOSAT tracks superimposed. The IR imagery between 6 May and 16 May was completely cloud-covered. All the information during the intervening period came from altimetry.

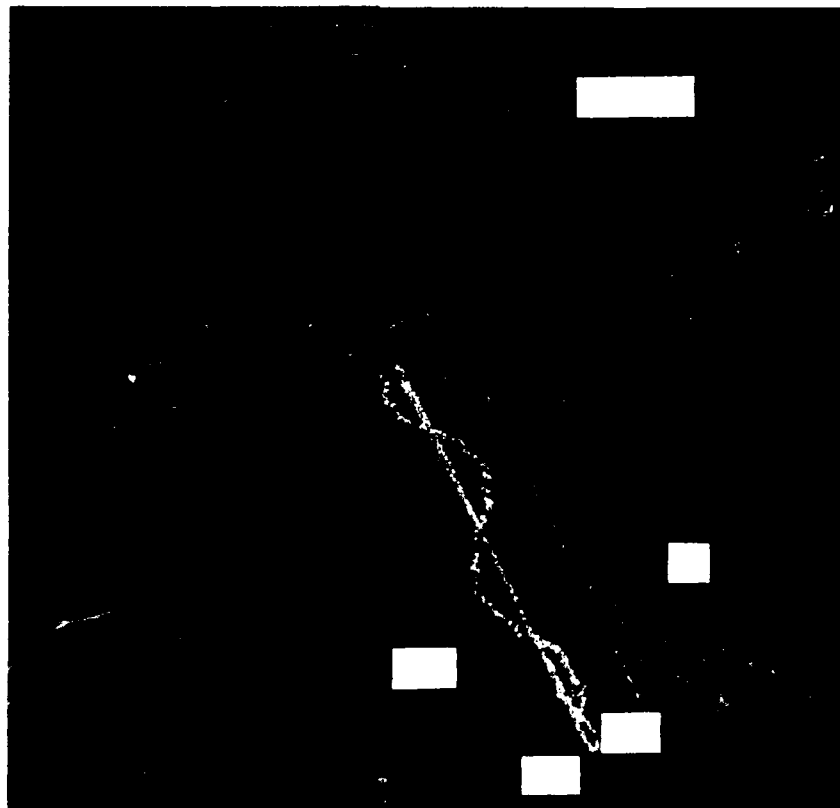


FIG. 8. Infrared image showing CCR interacting with Gulf Stream. The day 73 GEOSAT track indicates a strong CCR with a 150-cm dynamic height depression.

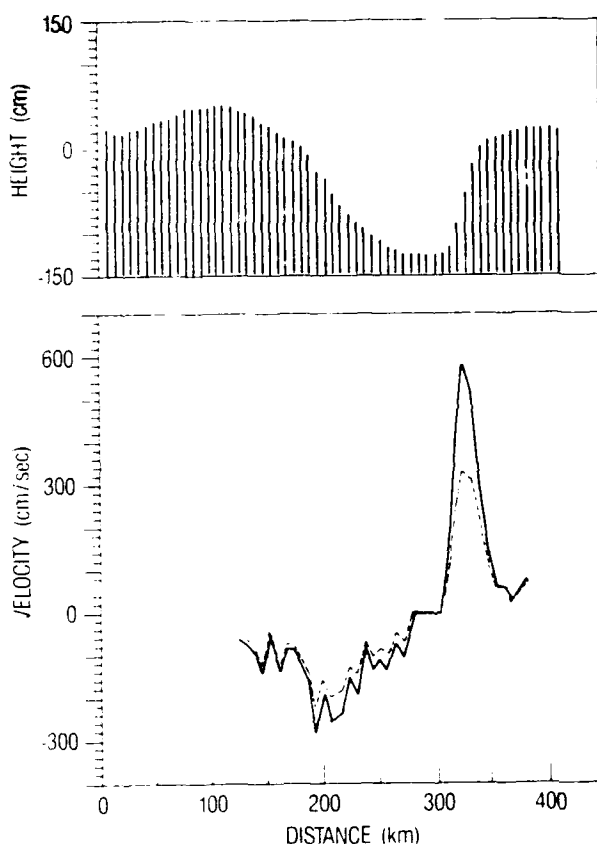


FIG. 9. Altimeter trace through CCR of Fig. 8 (upper plot) with corresponding geostrophic velocity profile (lower plot, solid curve). Dashed curve in lower plot shows the result of applying the centrifugal correction.

track's altimetric signal (year day 125). This WCR moved westward from its earlier position. Though this strong vortex is not visible in the IR image because of cloud cover, the altimeter shows almost 100 cm of relief. Figure 7 shows a repeated interaction between ring D and the Gulf Stream 10 days later. A descending altimeter track (year day 134) intersects this ring. It shows a strong, asymmetric signal that indicates the partly meander-like circulation with a large portion of the Gulf Stream signal south of the WCR.

c. Interpretation and difficulties

NORDA chose the northwest Atlantic region that contains the Gulf Stream and rings as a demonstration area because of the pronounced altimetric signal and the existence of a high-quality geoid. Figure 3 shows the GOAP area and the GEOSAT orbit's ground-track laydown for a 7-day period during the primary mission (the first 18 months). Consecutive ascending or descending tracks were separated by 25.1 degrees of longitude at the equator as the satellite revolved around the earth about 14.3 times per day. The situation is essentially the same for the ERM orbit. Since the al-

timeter is a nadir-looking instrument with a field of view of only a few km, there are very wide gaps in coverage during a 1-day period, approximately 2100 km in the GOAP area. Even after a week there are large, diamond-shaped holes in the coverage.

The spatial scale of mesoscale features in the Gulf Stream area is about 100 km. The Gulf Stream's daily position changes can be large (about 30 km), while the rings move slowly, 4 to 5 km per day on the average; occasionally they may shift 15 km per day. Obviously altimeter coverage alone cannot describe the mesoscale field. NORDA chose satellite IR imagery to compensate for the altimeter's lack of synopticity, and occasional in situ XBT measurements provided detailed information about the ocean's vertical thermal structure at key locations.

The almost ever-present appearance of clouds is one of the detriments common to all present mesoscale interpretations in the Gulf Stream region when using IR. Experience indicates that although one IR image may reveal all or none of the Gulf Stream, typically about 30–40 percent is visible. This percentage differs with the season. During the summer months seasonal surface heating obscures the IR signatures of older cold rings. In such conditions the altimetric signal becomes essential. Difficulties in the interpretation of altimetric signals in terms of mesoscale features stem from:

- (i) the particular geometry of mesoscale features and altimetric tracks (important if no IR is available), and
- (ii) geophysical corrections.

Oblique crossings of the Gulf Stream by the altimeter belong to the first category. A pass perpendicular to the Gulf Stream would have a strong, narrow SSH signal, but a pass at an acute angle would take longer to cross the Gulf Stream, and the signal would be spread out. Also, little or no Gulf Stream signal is apparent when the altimeter crosses an area of strong interaction between the Gulf Stream and rings (Fig. 6 shows an example). The ground track may also intersect a ring near its edge, making it appear small.

The main problems of the second category result from errors in the reference surface. The error connected with "smearing" of the Gulf Stream in the geoid was discussed in section 3b(3). A good example is the S-shaped altimeter signal in Fig. 6, in the ascending track for year day 125. It corresponds to case 2 of Fig. 2. This error appears to strengthen the warm ring's signal in the north and falsely indicates a return current south of the Gulf Stream. Along GEOSAT-ERM ground tracks, estimates of the geoid profile which are relatively uncontaminated by the mean topography can be obtained as the difference between simultaneous dynamic topography profiles (from deep XBT sections) and GEOSAT-ERM overflights (Mitchell et al. 1989). Of course, such estimates are contaminated by the barotropic component of sea level (see Hallock et al. 1989).

Distortions and asymmetries of rings were observed due to errors in the reference surface. In general, CCRs are easier to detect than WCRs. The reasons are that warm rings very often interact with the Gulf Stream, the geoid is less well known in the area of the continental slope where WCRs exist, and WCRs have flatter profiles than CCRs of similar diameter. The balance of forces explains the last effect. In warm rings, the horizontal pressure gradient is aided by centrifugal force to balance the Coriolis force. In contrast, cold rings exhibit a large sea surface displacement because the Coriolis and centrifugal forces work in unison against the pressure gradient.

Our experience indicates that simultaneous IR and altimetry often agree in determining the northern Gulf Stream boundary, with precision limited by the altimeter data (14 km). But, there are cases when they disagree. The IR image in Fig. 8 indicates that the Gulf Stream meanders southward around the interacting cold ring. Altimeter data, namely the year day 70 ascending track, agree with IR images in this southern branch, but also show a continuation of the Gulf Stream as a bridge north of the ring. Figure 6 shows a sharp meander, perhaps in weak interaction with the CCR. The year day 125 ascending altimeter track shows the Gulf Stream's position shifted about 40 km north of where the IR image indicates. These cases are not

unprecedented: Hansen and Maul (1970), Robinson et al. (1974), and Horton (1984) found that the 15°C isotherm at 200 m, considered to be the core of the Gulf Stream, can be considerably separated from the near-surface thermal structure. Perhaps in the above interactions the deeper portion of the Gulf Stream acts separately from the surface Gulf Stream and produces the surface topography seen in the SSH signal. It is also possible that part of the difference observed is due to a mismatch in time between the IR and altimetric observations.

It is sometimes difficult to establish whether meanders are pinched off from the Gulf Stream. Figure 10 shows a large cold-core meander extending 380 km southward. This meander is strong and never closes to create a cold ring. Fortunately, IR data are available to confirm this interpretation.

f. Preparation of mesoscale maps

NORDA used altimeter SSH residuals combined with Advanced Very High Resolution Radiometer (AVHRR) and XBT data to produce a depiction of the Gulf Stream's north and south walls and warm- and cold-core rings. This depiction consists of an alphanumeric description of the features' positions and strengths (i.e., sea-surface temperature gradients).

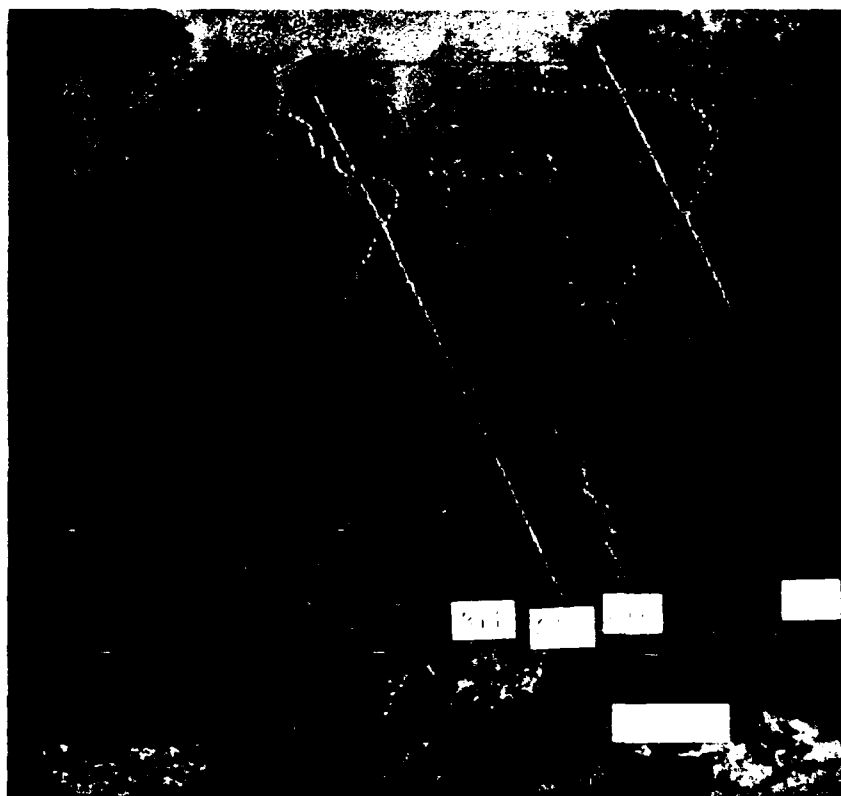


FIG. 10. Infrared image for 9 November 1985 with superimposed altimetry. Note very large cold core meander extending 380 km southward.

During the GOAP operational demonstration this description was sent as a Navy message and used as a "bogus" (a commonly-used Navy term for manually adjusted data, e.g., front and eddy locations) for FNOC's Expanded Ocean Thermal Structure three-dimensional thermal analysis (Clancy 1987). NORDA also provided the information in graphic form (the mesoscale map described in section 4a) as a quality-control measure. A 4- to 7-day sliding window of SSH and AVHRR data went into each of the twice-weekly GEOSAT mesoscale maps and alphanumeric descriptions.

Section 3 describes the treatment of the altimeter data during the operational demonstration. An average of two AVHRR images per day were received from each NOAA satellite. Those for which the area of interest was not totally cloud-covered were calibrated and "warped" to a Mercator projection at a resolution of 2.5 km. In some cases it was found helpful to combine channels 4 and 5 to create multichannel sea-surface temperature (MCSST) images, especially during the summer when high concentrations of water vapor often obscure the oceanic features in a single channel. The NORDA analyst displayed IR images in a format compatible with the altimetry to cover the area of interest with a 5-km resolution, but 2.5-km-resolution sections were available if needed. During the cloudy periods, composite images created from several days of IR data show more of the mesoscale features than individual images. Those "warmest-pixel" composites were created from a registered sequence of images by assigning to each pixel location the value corresponding to the highest temperature from all images in the sequence.

NORDA received daily BT data from FNOC. These data are collected by FNOC from various ship surveys without systematic distribution in relation to our purposes. The NORDA analyst used the profile's character and the depth of the 15°C isotherm to apply corrections to the mesoscale feature map.

Figures 5-8 and 10, which show SSH profiles superimposed on an IR image, illustrate the approach used in the GOAP mesoscale analysis, which is to combine complementary data types. Altimeter data displayed on an image of the Gulf Stream area helps the analyst to visualize the relationship between the two data types. The imagery's superior area coverage compensates for the altimeter's lack of synopticity (Leitao et al. 1979), while the mesoscale features' thermal signatures give information about their shapes. The figures also illustrate the altimeter's ability to penetrate cloud cover and reveal information not visible in the IR imagery. The analyst combines all of this information with the aid of interactive image processing, which allows color enhancement of IR imagery and provides the ability to overlay profiles of other data. The interactive aspect allows the analyst to view an image, manipulate it and observe the results, and continue to perform image processing operations until

he is satisfied with the results. The addition of BT observations provided the interpreter even more information.

The analyst begins the GOAP interpretive procedure by displaying SSH profiles from passes within the area of interest, and uses a cursor to select positions of interest along each profile. The analyst also displays significant wave height, geoid height, tilt and bias correction, raw (altimeter-measured) range, water vapor correction, and tide height along the orbital pass ground track to check for data errors.

Figure 4 shows an example of an SSH profile used in an analysis. Selected points are assigned numbers and all data associated with each point are stored in a file. Figure 11 presents two other SSH profiles and the features derived from them.

Once a representative sample of SSH residuals are displayed and analyzed, the selected points are displayed against the common grid (Fig. 12). Four to seven days of data are generally displayed for each mesoscale feature map. This time represents a compromise between the amount of data necessary to complete the mesoscale map and the time scale of mesoscale motions characteristic of the Gulf Stream system. The most recent SSH profile receives the greatest weighting in the final mesoscale feature map.

The next step is the study of IR images from the same period. First, the analyst displays the most recent IR image on the common grid, and stretches the con-

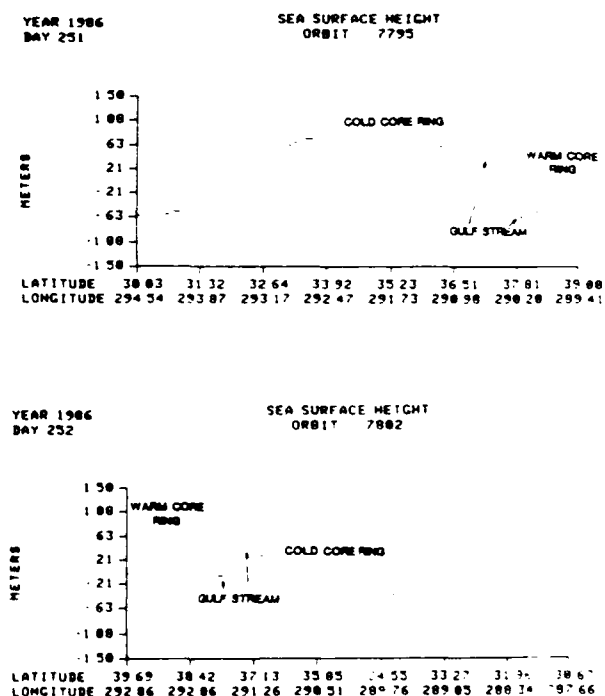


FIG. 11. Sea surface height residuals for GEOSAT orbits 7795 and 7802 on year days 251 and 252, respectively, showing identifiable mesoscale features.

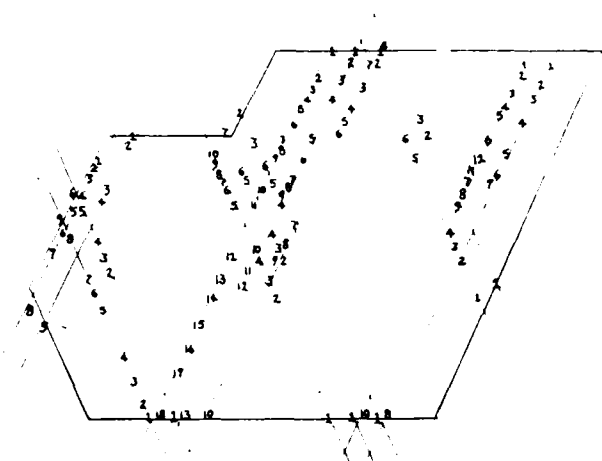


FIG. 12. Selected GEOSAT passes and various points selected along each nadir track to represent possible mesoscale feature locations for a 7-day period.

trast and brightness to enhance the features visible in the image. The analyst observes the imagery at a thermal resolution of 0.125°C in limited temperature ranges by selective enhancement of temperature "win-

dows." Likewise, a "zoom" to a full-resolution display of a smaller area is possible if necessary to study detail.

Using a trackball to position the cursor, the analyst selects points along the Gulf Stream's north and south walls to represent their positions. Similarly, the analyst selects WCR and CCR centers and radii, and saves all the values to a file. The analyst repeats the process for older IR images in reverse chronological order. He then combines the SSH and IR data by displaying them together on the common grid. In many instances the north wall positions indicated by the SSH residual profiles and the IR imagery are within one SSH residual point, or 7 km, of each other. Using the most recent available data, the analyst constructs a continuous line depicting the Gulf Stream. In areas of no SSH residuals or IR imagery, the analyst uses his experience analyzing the Gulf Stream's behavior, and the Gulf Stream and ring positions from the most recent previous mesoscale feature map, to complete the new map.

Next, the analyst displays BT data on the common grid. Each BT's position and measured vertical temperature profile are displayed (Fig. 13). The depth of the 15°C isotherm is a key in the Gulf Stream area to evaluate the mesoscale feature map's correctness (Tracey and Watts 1986). If the 15°C water is below 460 m, then the BT is assumed to be in Sargasso water. If

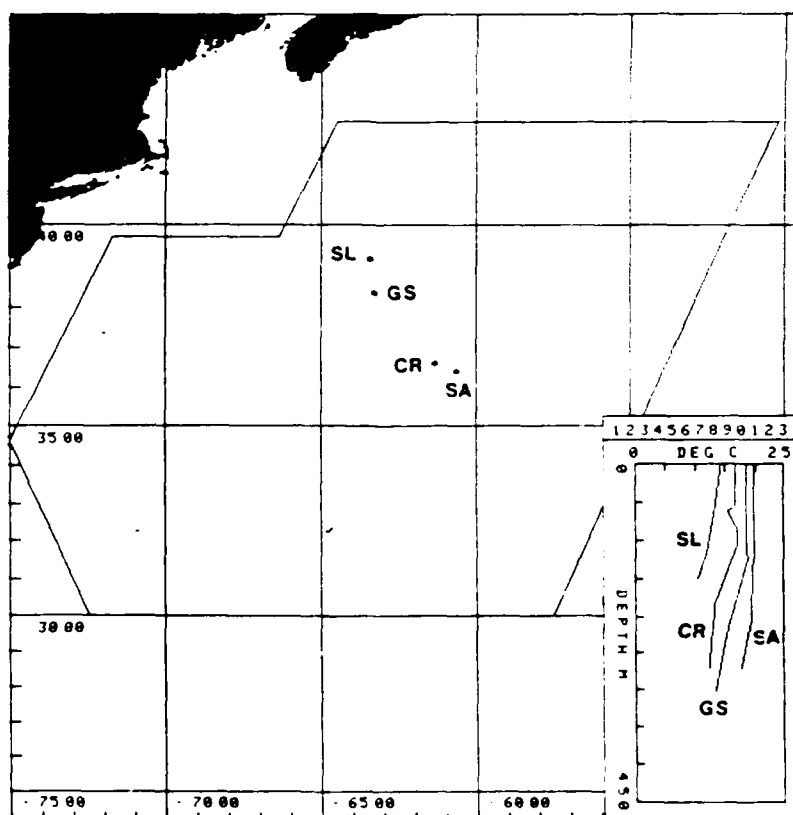


FIG. 13. Positions of bathythermographs from FNOG and the vertical temperature profiles associated with each (SL: slope, CR: cold-core ring, GS: Gulf Stream, and SA: Sargasso).

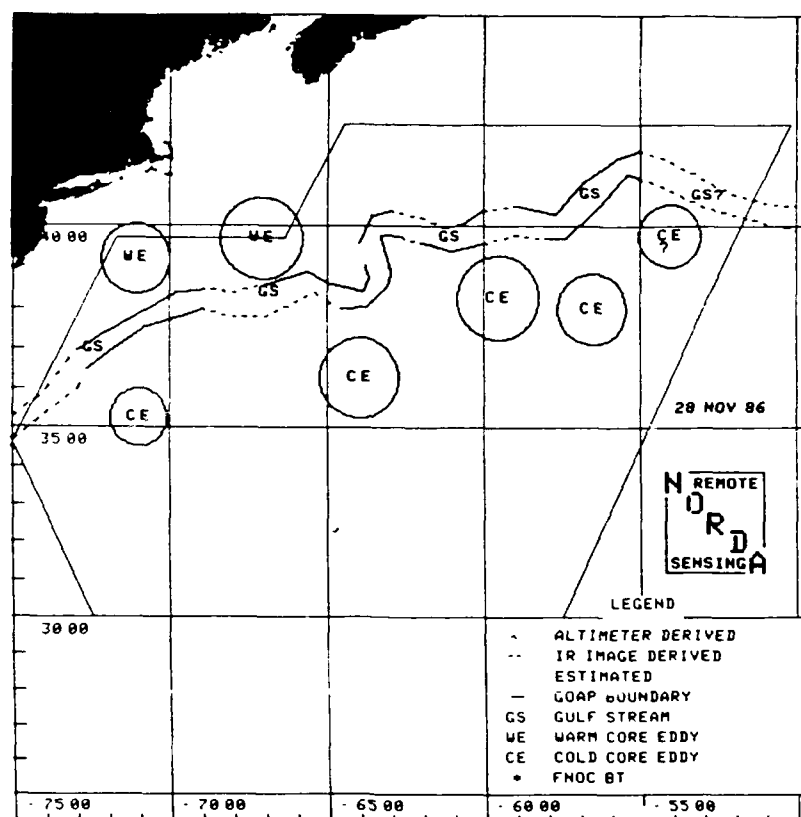


FIG. 14. The GOAP mesoscale map for 28 November 1986.

no 15°C water is found or if it is above 100 m in summer, then slope water is assumed to be present. If 15°C water is present between 200 and 460 m and if the position is south of the Gulf Stream, then a CCR is indicated. A warmer profile north of the Gulf Stream suggests a WCR. This information is used to verify the existence of and locate features indicated by SSH residual data. Figure 14 shows a sample GEOSAT mesoscale map.

FNOCT also makes the GOAP mesoscale product information available to NEOF, the regional oceanographic center whose area of responsibility includes the GOAP mesoscale test area. NEOF has found the information to be helpful, particularly as an indication of possible CCR activity in locations where surface thermal signatures are not visible in IR imagery. On several occasions, the GOAP product located a cold eddy that was subsequently verified by satellite imagery

or BT data. Generally, NEOF finds that more eddies, both warm and cold, are evident in the GOAP product than are revealed by IR imagery alone.

5. Results

a. Winds, waves, ice

Shuhay et al. (1987) and Dobson et al. (1987) present information on the accuracy of GEOSAT wind and wave data. Tables 1 and 2, which contain information from Dobson et al. (1987), summarize some of the results.

Tables 1 and 2 show that the prelaunch accuracy targets for wind and wave measurements have been met or exceeded. It is more difficult to obtain quantitative assessments of the accuracy of the ice-edge data. However, comparisons with IR and visible satellite imagery are favorable.

TABLE 1. Wind speed accuracy (Buoys within 50 km and 0.75 deg pointing error).

	Goal	Measured
Rms	1.8 m s ⁻¹	1.7 m s ⁻¹
Mean	0 m s ⁻¹	0.3 m s ⁻¹

TABLE 2. Significant wave height accuracy (43 open-ocean buoys within 50 km of nadir tracks).

	Goal	Measured
Rms	0.5 m or 10%	0.49 m
Mean	0 m	0.36 m

Pickett et al. (1987) illustrate GEOSAT wave data. FNOC incorporates GEOSAT significant wave height data into a Visual Sea Height Analysis (Clancy 1987), which attempts to provide an accurate synoptic representation of global significant wave height. It uses the Fields by Information Blending (FIB) analysis technique (Holl et al. 1979) to map SWH observations less than 6 hours old into a Global Spectral Ocean Wave Model first-guess wave field (Clancy 1987). The FIB technique weights the wave height observations by time and grid point distance relative to the first-guess field and spreads their influence accordingly.

Hawkins and Lybanon (1989) provide details on the GEOSAT ice products and NPOC's use of them. The altimeter's all-weather capability has been an important addition to the NPOC databases, since cloud cover can drastically curtail visible and IR viewing, and passive microwave data has coarser resolution. Hawkins and Lybanon (1989) present several illustrations that show GEOSAT along-track ice index values superimposed on satellite images. They clearly indicate the ice index's ability to delineate the ice edge, and suggest that the index may be sensitive to ice concentration or ice type. Ongoing NORDA research efforts are aimed at investigating this possibility, and at extracting additional sea-ice information from the altimeter waveform data (e.g., Chase and Holyer 1988).

b. Mesoscale results

The GOAP mesoscale analyses comprise a large dataset, from which statistics on Gulf Stream and ring positions and velocities can be obtained. Comparisons with other datasets tend to confirm the accuracy of the GOAP results. The relative contributions of altimetry, IR, and analyst estimates to the GOAP mesoscale analyses vary, but average about one-third each. Altimetry contributes as much information as IR imag-

ery, so it is clearly an important addition to the analyst's list of information sources. Some of the problems encountered in using altimeter data are summarized later in this section.

The mean, standard deviation, and extreme positions of the Gulf Stream during the period March 1986 through November 1987, as derived from the GOAP mesoscale analyses, are presented in Fig. 15. The data are consistent with data recently published by Auer (1987). The two-tiered Gulf Stream shows east-west trends along 38°N from 71° to 65°W and along 40°N from 62° to 50°W. The Gulf Stream's northward movement occurs in the wake of the New England Seamount Chain.

The mesoscale products have been compared qualitatively with similar products from NEOC. Portions of the Gulf Stream pass over inverted echo sounder (IES) installations maintained by the Regional Energetics Experiment (REX) (Mitchell et al. 1987). There were two IES arrays, deployed across the historical mean Gulf Stream path near 67° and 58°W. Teague and Hallock (1989) used the IES measurements to estimate the Gulf Stream's position. Their analysis was based on a procedure used by Watts and Johns (1982). Preliminary results of a comparison of IES and GOAP analyses are presented in Table 3. "Good agreement" means within 20 km; "favorable agreement" means 20–50 km displacement. This table shows at least favorable agreement between the IES and GOAP analyses in 79 percent of the overall data, with 75 percent agreement east of the New England Seamounts and 83 percent agreement west of the seamounts.

Table 4 contains information that shows the relative importance of altimetry, IR, and estimates for determining the position of the Gulf Stream's north wall. The monthly percentages were derived from the Navy messages prepared at NORDA (the alphanumeric mesoscale products), which include latitudes and longi-

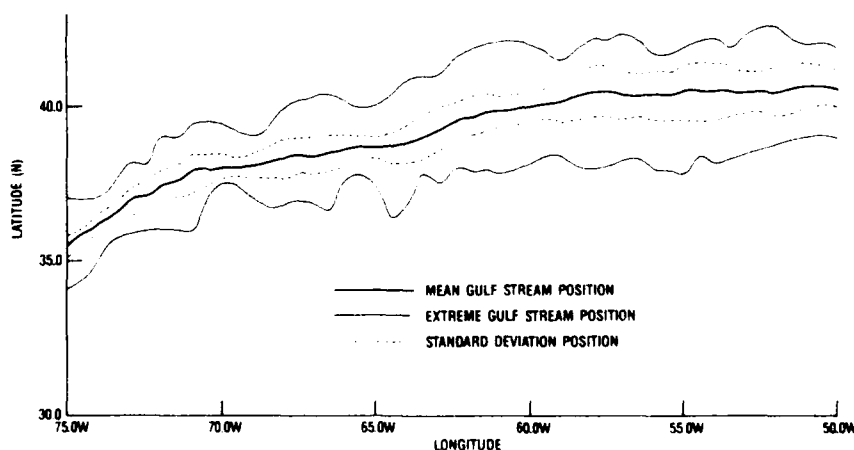


FIG. 15. Gulf Stream mean position with standard deviation and extremes. The results shown are derived from the GOAP mesoscale analyses.

TABLE 3. Comparison of GEOSAT Ocean Applications Program and Inverted Echo Sounder analyses*.

	West	East	Total
Good agreement	70%	31%	51%
Favorable agreement (features displaced)	13%	44%	28%
Bad agreement	17%	25%	21%

* Information courtesy of W. J. Teague.

tudes of points on the Gulf Stream north wall from 75° to 50°W. Table 4 lists the percentage of points in 1 month's messages derived from IR imagery, altimetry, or estimates. The values do not directly give percentages of Gulf Stream length identified by each technique.

The altimeter consistently contributed to the preparation of the mesoscale product: the relative size of the contribution depended on the quantity of cloud-free IR imagery available and the amount of altimetry data recovered. Due to changes in GEOSAT that occur as the spacecraft travels from darkness into sunlight, the altimeter occasionally does not acquire lock on its return signal until after it passes the GOAP demonstration area. (This problem primarily affected descending tracks in the Northern Hemisphere.) The altimeter's contribution to the mesoscale product was relatively constant at about one-third of the information, but varied from a low of 24 percent in June and July 1987 to a high of 38 percent in May 1986. The contribution from IR imagery had a higher variability, from 23 percent in February 1987 to 54 percent and 55 percent in July 1987 and June 1986, respectively.

Although atmospheric frontal passages tend to leave clear, dry areas as they pass, during the winters of 1986 and 1987 the fronts appeared to stall before leaving the GOAP area, causing portions of the Gulf Stream to be cloud-covered for long periods and decreasing the contribution of the IR imagery to the mesoscale product. During the summer, clouds and high atmospheric water-vapor content hamper the computation of accurate sea-surface temperature values. Nevertheless, atmospheric conditions change fast enough to give the analyst more information from the IR imagery during summer than winter. Although exact temperatures and minor thermal changes are not visible, the Gulf Stream's north wall can be located. The amount of information provided by IR imagery to a mesoscale product averaged approximately one-third of the total.

The "estimated" portion of the mesoscale product also depended on the amount of IR imagery. During periods when more IR images were available the estimated portion decreased, and vice versa. A single altimeter point located on the Gulf Stream north wall helped the analyst to estimate how the Gulf Stream moved in a cloudy area.

The GEOSAT orbit's ground-track laydown does not provide synoptic coverage, as discussed in section 4e and illustrated by Fig. 3. It is entirely possible for the altimeter to miss mesoscale rings for days or even weeks, and even if the altimeter observes a feature the ground-track pattern may not intersect that feature again for an extended period. So, there may be only one cross section, through any part of the feature, as evidence for the feature when the analysis is performed.

As Figs. 11 through 13 illustrate, the mesoscale features do not always appear as obvious choices to the analyst. Section 4e pointed out that much variability in signal similarity arises from the angle at which the GEOSAT pass crosses the Gulf Stream. Water vapor may also affect the selection of mesoscale features. The appearance of an individual CCR or WCR also varies depending on the portion of the ring that the pass crosses. Crossing a ring edge results in a smaller signal (in both extent and amplitude) than crossing a ring center. Because a ring's size and strength change with age, the SSH signal also varies with a ring's age. It is important to note that young rings include moving water around their perimeters, reflected in the SSH as part of the ring, which does not have the same properties as water in the ring's true interior. Geoid errors also distort the altimetric signal, as the frequent presence of clouds diminishes the utility of IR images.

During the first 18 months of GEOSAT the ground tracks defined a tightly spaced global mesh, but the nonrepeating ground track pattern did not allow the clear separation of the geoid from the instantaneous topographic components of sea level, except in areas where a gravimetric geoid was known. One reason for

TABLE 4. Gulf Stream north wall monthly statistics from GEOSAT mesoscale maps.

Month	Number of products	Percent from		
		IR	ALT	EST
(1986)				
Mar	8	26	31	43
Apr	9	40	31	29
May	7	33	38	29
Jun	7	55	26	19
Jul	6	40	29	31
Aug	8	33	34	33
Sep	4	26	26	48
Oct	(Satellite moved to ERM orbit.)			
Nov				
Dec	8	30	33	37
(1987)				
Jan	4	29	30	41
Feb	6	23	27	50
Mar	7	37	25	38
Apr	9	33	26	41
May	9	44	25	31
Jun	9	49	24	27
Jul	9	54	24	22

the choice of the GOAP mesoscale test area was the existence of a high-quality geoid for the northwest Atlantic Ocean. The satellite's ground track repeats almost exactly every 17 days during the ERM, so an analyst can use an along-track ensemble mean "surface" where no precise geoid is available.

6. Conclusions

The GEOSAT altimeter's all-weather capabilities and its received pulse's relationship to several geophysical parameters make it a desirable sensor for oceanographic and meteorological investigations. Surface wind speed and significant wave height are produced with minimal processing from the shape and power of the return microwave pulse. An ice index related to the presence or absence of ice, and therefore the sea ice edge, can also be generated from the reflected microwave pulse. Significant ocean currents produce a variable sea surface topography that is easily measured by the GEOSAT altimeter.

The GEOSAT altimeter's microwave pulse is affected by atmospheric water, but the degradation is not so great that Gulf Stream mesoscale features are not identifiable. Although atmospheric water vapor signals are indistinguishable from the oceanographic signal, they are smaller than the signals that oceanographic features produce in the GOAP area. In other areas this would not be the case, and a water vapor correction would probably be needed (Phoebus and Hawkins 1990). If clouds are present, the SSH residuals may yield the only certain mesoscale feature positions in the mesoscale map.

An added capability of the SSH residual is the ability to detect the surface topographic manifestation of mesoscale features having no surface IR expression. Cheney (1982) points out that dynamic height is largely a function of thermocline depth, and found that there is a high correlation between dynamic height and the depths of the 15°C isotherm, the 17.5°C isotherm, and the temperature at 350 m. The possibility of inferring subsurface thermal structure from sea surface topography was also noted by Khedouri et al. (1983).

During the GOAP operational demonstration, significant wave height and surface wind speed were processed and transmitted automatically to FNOC to be used as input data and quality control information. Ice index values were plotted and the graphics transmitted to the Joint Ice Center in Suitland, Maryland, to aid in the identification of the sea ice edge. Sea surface height residuals were processed daily and analyzed twice each week to generate a Gulf Stream region mesoscale map.

The validity of the mesoscale map is based on the interpretation of SSH residual patterns as oceanographic features. The effectiveness of the interpretation is presented in numerous comparisons of SSH residuals

and satellite IR imagery. In fact, the SSH residuals and IR imagery are used in concert with in situ temperature profiles to generate the most accurate mesoscale map possible. Statistics from a time series of these mesoscale maps indicate that satellite IR imagery and GEOSAT SSH residuals each contribute approximately one-third of the information for any mesoscale map. The remaining one-third is analyzed subjectively.

Oceanographic information derived from GEOSAT altimetry has already proven to be of value in depicting mesoscale circulation and significantly increasing the quantity of ice edge information available. The altimeter's ability to provide oceanographic information when other sensors suffer from impaired viewing further increases its value. NORDA is beginning to extend the techniques developed for GOAP to other portions of the world ocean, and is developing assimilation techniques to use altimeter data more directly in numerical models. Many other researchers are reporting a variety of work with GEOSAT data. The research studies and applications based on GEOSAT data clearly demonstrate the altimeter's usefulness as a tool to collect timely, accurate oceanographic information.

Acknowledgments. This document has been reviewed and is approved for public release; distribution is unlimited. NORDA Contribution Number JA321: 015:89.

The authors are glad to acknowledge the many contributions that made this project and this paper possible. Y. Crook and N. Koenenn performed image processing and numerous other tasks during GOAP; the former also provided many of this paper's illustrations. H. Beresford and E. McNutt assisted with analyses of the product output data. S. Peckinpaugh developed much of the analysis software. J. Mitchell contributed scientific advice. W. Teague provided information on the accuracy of the GOAP mesoscale products. C. Kilgus and J. MacArthur provided information about the GEOSAT spacecraft, altimeter, and ground processing. J. Hawkins, D. Johnson, and L. Jenkins provided critical readings of the manuscript and made several helpful suggestions. The anonymous referees made a number of suggestions during the review process that resulted in an improved manuscript. The work was directly supported by the Satellite Applications and Techniques (SAAT) Program. A. E. Pressman, Program Manager.

REFERENCES

- Auer, S. J., 1987: Five year climatological survey of the Gulf Stream system and its associated rings. *J. Geophys. Res.*, **92**, 11 709-11 726.
- Bisagni, J. J., 1976: Passage of anticyclonic Gulf Stream eddies through deepwater dumpsite 106 during 1974 and 1975. NOAA Dumpsite Eval. Rep. 76-1.
- Born, G. H., M. A. Richards and G. W. Rosborough, 1982: An empirical determination of the effects of sea state bias on SEASAT altimetry. *J. Geophys. Res.*, **87**, 3221-3226.

- Brooks, R. L., W. J. Campbell, R. O. Ramseier, H. R. Stanley and H. J. Zwally, 1978: Ice sheet topography by satellite altimetry. *Nature*, **274**, 539-543.
- Brown, G. S., H. R. Stanley and N. A. Roy, 1981: The wind speed measurement capability of spaceborne radar altimeters. *IEEE J. Oceanic Eng.*, **25**, 59-63.
- Chase, J. R., and R. J. Holyer, 1988: Estimation of sea-ice type and concentration by linear unmixing of GEOSAT altimeter waveforms. *Proceedings of IGARSS '88 Symposium*, Edinburgh, Scotland, 13-16 Sept. 1988, ESA Publications Division, ESTEC, Noordwijk, The Netherlands, 1127-1128.
- Cheney, R. E., 1982: Comparison data for SEASAT altimetry in the western North Atlantic. *J. Geophys. Res.*, **87**, 3247-3253.
- , and P. L. Richardson, 1976: Observed decay of a cyclonic Gulf Stream ring. *Deep-Sea Res.*, **23**, 143-155.
- , and J. G. Marsh, 1981: SEASAT altimeter observations of dynamic topography in the Gulf Stream region. *J. Geophys. Res.*, **86**, 473-483.
- Clancy, R. M., 1987: Real-time applied oceanography at the Navy's global center. *Mar. Tech. Soc. J.*, **21**, 33-46.
- Cole, T. D., 1985: GEOSAT—A data users' ground system interface control document (ICD). Rep. 7692-9510 (Rev. 1). The Johns Hopkins University, Applied Physics Laboratory, Laurel, MD 20707, 75 pp.
- Doblar, R. A., and R. E. Cheney, 1977: Observed formation of a Gulf Stream cold-core ring. *J. Phys. Oceanogr.*, **7**, 944-946.
- Dobson, E., F. Monaldo, J. Goldhirsh and J. Wilkerson, 1987: Validation of GEOSAT altimeter-derived wind speeds and significant wave heights using buoy data. *J. Geophys. Res.*, **92**, 10 719-10 731.
- Dwyer, R. W., and R. H. Godin, 1980: Determining sea ice boundaries and ice roughness using GEOS-3 altimeter data. NASA Contractor Rep. 156862, 47 pp.
- Eppler, D. T., 1982: Possible applications of GEOSAT—A radar altimeter data to ice forecasting in polar regions. Technical Note 177, Naval Ocean Research and Development Activity, NSTL, MS 39529, 16 pp.
- Fuglister, F. C., 1972: Cyclonic rings formed by the Gulf Stream 1965-1966. *Studies in Physical Oceanography: A Tribute to George Wüst on his 80th Birthday*, A. Gordon, Ed., Gordon and Breach, 137-168.
- Gallagher, N. C., Jr., and G. L. Wise, 1981: A theoretical analysis of the properties of median filters. *IEEE Trans. Acoustics, Speech, & Signal Processing*, **AASP-29**, 1136-1141.
- Gothardt, G. A., 1973: Observed formation of a Gulf Stream anticyclonic eddy. *J. Phys. Oceanogr.*, **3**, 237-238.
- , and G. J. Potocsky, 1974: Life cycle of a Gulf Stream anticyclonic eddy observed from several oceanographic platforms. *J. Phys. Oceanogr.*, **4**, 131-134.
- Halliwell, G. R., Jr., and C. N. K. Mooers, 1979: The space-time structure and variability of the shelf water-slope water and Gulf Stream surface temperature fronts and associated warm-core eddies. *J. Geophys. Res.*, **84**, 7707-7725.
- Hallock, Z. R., J. L. Mitchell and J. D. Thompson, 1989: Sea surface topographic variability near the New England seamounts: An intercomparison among in situ observations, numerical simulations, and Geosat altimetry from the regional energetics experiment. *J. Geophys. Res.*, **94**, 8021-8028.
- Hansen, D. V., and G. Maul, 1970: A note on the use of sea surface temperature for observing ocean currents. *Remote Sens. Environ.*, **1**, 161-164.
- Hawkins, J. D., and P. M. Smith, 1986: Effects of atmospheric water vapor on the detection of mesoscale oceanographic features from GEOSAT. Rep. 126, Naval Ocean Research and Development Activity, NSTL, MS 39529, 21 pp.
- , and M. Lybanon, 1989: GEOSAT altimeter sea-ice mapping. *IEEE J. Oceanic Eng.*, **14**, 139-148 (invited paper).
- Holl, M. M., M. J. Cuming and B. R. Mendenhall, 1979: The expanded ocean thermal structure analysis system: A development based on the fields by information blending methodology. Tech. Rep. M-241, Meteorology International Inc., Monterey.
- Hollinger, J. P., 1980: SEASAT altimeter atmospheric range correction. Memo. Rep. 4342, Naval Research Laboratory, Washington, DC, 26 pp.
- Horton, C. H., 1984: Observations of a near-surface Gulf Stream eddy and of changes in the surface-subsurface frontal separation. *J. Phys. Oceanogr.*, **14**, 1407-1414.
- Kelly, K. A., and S. T. Gille, 1990: Gulf Stream surface transport and statistics at 69°W from the GEOSAT altimeter. *J. Geophys. Res.*, **95**(C3), 3149-3161.
- Khedouri, E., C. Szezechowski and R. E. Cheney, 1983: Potential oceanographic applications of satellite altimetry for inferring subsurface thermal structure. *Proceedings, OCEANS '83 Conference*, San Francisco, California, 29 August-1 September 1983.
- Kilgus, C. C., 1989: Gulf Stream dynamic topography measured from space (Meeting Report). *Eos Trans. Amer. Geophys. Union*, **70**, 709.
- Lai, D. Y., and P. L. Richardson, 1977: Distribution and movement of Gulf Stream rings. *J. Phys. Oceanogr.*, **7**, 670-683.
- Leitao, C. D., N. E. Huang and C. G. Parra, 1979: A note on the comparison of radar altimetry with IR and in situ data for the detection of the Gulf Stream surface boundaries. *J. Geophys. Res.*, **84**, 3969-3973.
- Lybanon, M., and R. L. Crout, 1987: The NORDA GEOSAT ocean applications program. *Johns Hopkins APL Tech. Dig.*, **8**, 212-218.
- MacArthur, J. L., 1978: SEASAT—A radar altimeter design description. Rep. SDO-5232, The Johns Hopkins University, Applied Physics Laboratory, Laurel, MD 20707, 156 pp.
- , P. C. Marth, Jr., and J. G. Wall, 1987: The GEOSAT Radar Altimeter. *Johns Hopkins APL Tech. Dig.*, **8**, 176-181.
- McConathy, D. R., and C. C. Kilgus, 1987: The Navy GEOSAT Program: An overview. *Johns Hopkins APL Tech. Dig.*, **8**, 170-175.
- Mitchell, J. L., 1989: The estimation of geoid profiles in the NW Atlantic from simultaneous satellite altimetry and AXBT sections. *J. Geophys. Res.*, in press.
- , Z. R. Hallock and J. D. Thompson, 1987: REX and GEOSAT: Progress in the first year. *Johns Hopkins APL Tech. Dig.*, **8**, 234-244.
- Monaldo, F., 1988: Expected differences between buoy and radar altimeter estimates of wind speed and significant wave height and their implications on buoy-altimeter comparisons. *J. Geophys. Res.*, **93**, 2285-2302.
- Morgan, C. W., and J. M. Bishop, 1977: An example of Gulf Stream eddy-induced water exchange in the Mid-Atlantic bight. *J. Phys. Oceanogr.*, **7**, 472-479.
- Newton, C. W., 1961: Estimates of vertical motions and meridional heat exchange in Gulf Stream eddies and a comparison with atmospheric disturbances. *J. Geophys. Res.*, **66**, 853-870.
- Olson, D. B., 1980: The physical oceanography of two rings observed by the cyclonic ring experiment. Part II: Dynamics. *J. Phys. Oceanogr.*, **10**, 514-528.
- Phoebus, P. A., and J. D. Hawkins, 1990: The impact of wet tropospheric correction on the interpretation of altimeter-derived ocean topography in the Northeast Pacific. *J. Geophys. Res.*, **95**(C3), 293-295.
- Pickett, R. L., D. A. Burns and C. H. Johnson, Jr., 1987: Ocean waves monitored by Navy satellite. *Mar. Tech. Soc. J.*, **21**, 62-63.
- Richardson, P. L., 1983: Gulf Stream rings. *Eddies in Marine Science*, A. R. Robinson, Ed., Springer-Verlag, 65-68.
- Robinson, A. R., J. R. Luyten and F. C. Fuglister, 1974: Transient Gulf Stream meandering. Part I: An observational experiment. *J. Phys. Oceanogr.*, **4**, 237-255.
- , M. A. Spall and N. Pinardi, 1988: Gulf Stream simulations and the dynamics of ring and meander processes. *J. Phys. Oceanogr.*, **18**, 1811-1853.

- Sailor, R. V., and A. R. LeSchack. 1987: Preliminary determination of the GEOSAT radar altimeter noise spectrum. *Johns Hopkins APL Tech. Dig.*, **8**, 182-183.
- Schwiderski, E. W., and L. T. Szeto. 1981: The NSWC global ocean tide data tape (GOTD), its features and application, random-point tide program. Tech. Rep. TR 81-254, Naval Surface Weapons Center, Dahlgren, VA, 43 pp.
- Shuh, J. L., M. R. Grunes, E. A. Uliana and L. W. Choy. 1987: Comparison of GEOSAT and ground-truth wind and wave observations: Preliminary results. *Johns Hopkins APL Tech. Dig.*, **8**, 219-221.
- Stommel, H., 1965: *The Gulf Stream: A Physical and Dynamical Description*. 2nd edition, University of California Press, Berkeley.
- Tapley, B. D., J. B. Lundberg and G. H. Born. 1982: The SEASAT wet tropospheric range correction. *J. Geophys. Res.*, **87**, 3213-3220.
- , R. S. Nerem, C. K. Shum, J. C. Ries and D. N. Yuan. 1988: Circulation from a joint gravity field solution determination of the general ocean. *Geophys. Res. Lett.*, **15**, 1109-1112.
- Teague, W. J., and Z. R. Hallock. 1990: Gulf Stream path analysis near the New England Seamounts. *J. Geophys. Res.*, **95**(C2), 1647-1662.
- Tracey, K. L., and D. R. Watts. 1986: On Gulf Stream meander characteristics near Cape Hatteras. *J. Geophys. Res.*, **91**, 7587-7602.
- U.S. Department of Commerce, NOAA. 1982: Standard formats for weather data exchange among automated weather information systems. Rep. FCM-S2-1982, Federal Coordinator for Meteorological Services and Supporting Research, Washington, DC, 99 pp.
- Warm-Core Rings Collection (special section), 1985: *J. Geophys. Res.*, **90**, 8801-8951.
- Watts, D. R., and W. E. Johns. 1982: Gulf Stream meanders: observations on propagation and growth. *J. Geophys. Res.*, **87**, 9467-9476.

The Impact of the Wet Tropospheric Correction on the Interpretation of Altimeter-Derived Ocean Topography in the Northeast Pacific

PATRICIA A. PHOEBUS¹ AND JEFFREY D. HAWKINS

*Ocean Sensing and Prediction Division, Naval Ocean Research and Development Activity,
Stennis Space Center, Mississippi*

Atmospheric water vapor data derived from the special sensor microwave imager (SSM/I) are used to make time-coincident, wet tropospheric range corrections to Geosat altimeter data in the northeast Pacific. The original and corrected sea surface height residuals along numerous tracks are examined to determine the impact of water vapor on the altimeter signal. Mesoscale feature analyses of corrected and uncorrected altimeter data are used to assess the impact of water vapor path lengthening in areas of low sea surface height variability. Results indicate that the horizontal spatial variations in the water vapor height corrections are frequently similar to true oceanographic gradients. Interpretation of altimeter data is affected in several ways. The unaccounted-for presence of atmospheric water vapor may mimic or mask the true ocean features, and even small changes in the water vapor over short spatial scales can enhance a partially obscured feature. Analyses of all Geosat tracks crossing the area of interest in September 1987 clearly illustrate that water vapor frequently contaminates the ocean topography measurements, making the water vapor adjustment critical before the altimeter data can be successfully used to locate and identify mesoscale ocean features. Furthermore, the SSM/I and Geosat data must be closely matched in both space and time, a difficult task since it takes 3.5 days to obtain global SSM/I coverage with one operational sensor. To optimize the mesoscale oceanographic application of altimeter data, a bore-sighted radiometer should be included on all altimeter spaceborne platforms.

INTRODUCTION

The U.S. Navy launched a radar altimeter aboard the Geosat platform on March 12, 1985. Its primary mission was to provide the data needed to precisely map the Earth's geoid over the oceans [McConathy and Kilgus, 1987]. However, because the altimeter measures the ocean topography and other parameters along its track, it also provides important and useful oceanographic data. For example, the Naval Ocean Research and Development Activity (NORDA), through the Geosat Ocean Applications Program (GOAP), used the sea surface height (SSH) data to successfully locate mesoscale fronts and eddies in the Gulf Stream region [Lybanon and Crout, 1987]. Nevertheless, significant mesoscale oceanographic features are found in many parts of the world. We want to determine whether or not mesoscale altimeter data analysis can be extended to areas where the SSH variability is not as pronounced.

One such area is the northeast Pacific. There are several weak fronts in this area with dynamic height perturbations of 5–15 cm over 100–300 km [Roden and Robinson, 1988]. NORDA is involved in an extensive northeast Pacific (NEPAC) research project coupling real-time data analysis, remote sensing, and ocean prediction and acoustic modeling efforts. Our role in this project is to determine the usefulness of remotely sensed data (both infrared imagery and altimeter data) for locating mesoscale fronts and eddies. Because the SSH gradients in this area are weak, the potential altimeter error sources are more critical. Of these, the main error that is unaccounted for is the apparent path lengthening created

by the columnar atmospheric water vapor, also referred to as the vertically integrated water vapor or precipitable water (hereinafter referred to as WV). This error potentially occurs over the same length scale as mesoscale ocean features.

The presence of WV increases the time it takes the radar pulse to pass through the atmosphere to the ocean's surface and return. Since the distance to the surface is computed as a function of this transit time, when WV is present the ocean surface appears farther away than it actually is, resulting in a SSH estimate that is too low. Furthermore, if sharp horizontal gradients are present in the WV distribution, the apparent shape of the ocean's surface along the altimeter track may be significantly altered, and WV gradients may be mistakenly interpreted as actual mesoscale ocean features. In contrast, if abrupt WV changes occur at approximately the same location as the ocean features of interest, then the WV gradients may counteract the slope of the ocean topography, thereby masking or obscuring the true feature's signal. Early results from a few selected cases suggest that the presence of WV may seriously hinder the application of altimeter data for mesoscale oceanography in areas of relatively weak ocean signals [Phoebus and Hawkins, 1988]. Thus the purpose of this paper is to look in more detail at high-resolution WV data in the NEPAC region and determine how the WV alters the true mesoscale ocean signal and affects detection and interpretation of ocean features.

Columnar water vapor data have been provided by satellite passive microwave sensors since the launch of Nimbus 5 in 1972. Measurements from the electrically scanning microwave radiometer provided information with an estimated accuracy of 4.2 kg m^{-2} for the derived WV [Staelin *et al.*, 1976]. WV data from the scanning multichannel microwave radiometer (SMMR), launched on Nimbus 7 in 1978, provided observations at a horizontal resolution of 50 km with a swath width of 800 km. Advancement in algorithm development and sensor performance resulted in rms errors of

¹Now at Naval Oceanographic and Atmospheric Research Laboratory, Atmospheric Directorate, Monterey, California.

This paper is not subject to U.S. copyright. Published in 1990 by the American Geophysical Union.

Paper number 89JC03093

$2.1 \text{ kg m}^{-2} \text{ kg m}^{-2}$ when compared with independent radiosonde observations [Chang *et al.*, 1984]. A SMMR was also flown on board Seasat, which during its short life (3 months) provided the only same-track measurements of ocean topography and WV data. Finally, the special sensor microwave imager (SSM/I) on board the polar-orbiting Defense Meteorological Satellite Program (DMSP) platform has provided WV measurements at 25-km resolution within 1394-km swaths since June 1987. This is by far the most comprehensive spatial coverage of the global atmospheric moisture data available to date. The accuracy of these data is estimated at 2.4 kg m^{-2} globally [Alishouse *et al.*, 1990]. While this accuracy is slightly worse than that specified for the SSMR, the SSM/I has been in orbit a much shorter time and thus has a smaller data base from which to determine the accuracy of the observations.

Many studies have used remotely sensed WV data to describe atmospheric moisture fields over large space and time scales [Chang *et al.*, 1980; Chelton *et al.*, 1981; Njoku and Swanson, 1983; Short and Prabhakara, 1984]. While these types of studies are useful for climatic and modeling applications, they do not address our specific needs. Only a few efforts have been made to analyze WV using the temporal and spatial scales appropriate for oceanographic mesoscale applications. Askne *et al.* [1986] used atmospheric modeling techniques to estimate the altimeter path delay due to WV. Hawkins and Smith [1986] used Seasat SMMR data to show that the change in the altimeter path length due to WV alone can be 20–40% as large as the Gulf Stream front and eddy signals and that these gradients can occur over the same time and space scales as the features themselves. More recently, Monaldo [this issue] extensively analyzed Seasat SMMR WV gradients over spatial scales from 100 to 300 km for much of the world's oceans, while Bisagni [1989] used a limited data set to compare model-predicted WV [after Saastamoinen, 1972] with data from rawinsondes in the area near 69°W , 27°N at spatial scales up to 500 km. Both Monaldo and Bisagni concluded from their statistical studies that WV height corrections do not play a major role in the interpretation of mesoscale ocean features on their scales of interest, primarily for signals of at least 10 cm per 100 km. Furthermore, neither of these studies rigorously attempted to relate the presence of atmospheric frontal systems to the WV gradients.

Our study takes a somewhat different approach by looking at the impact of actual wet tropospheric corrections made to real altimeter SSH residuals. We pay particular attention to the relationship between the atmospheric fronts and the associated WV fields, focusing on changes in the oceanographic signal that are as small as 5 cm per 100 km. Since our interest is in the near-real-time location of mesoscale ocean features, our primary concern is how the wet tropospheric correction alters the interpretation of individual tracks. In this regard, our study is unique, which may explain why our conclusions differ from previous studies.

To satisfy the need for high-resolution WV data, we compute precipitable water from the SSM/I brightness temperatures, which provide a nearly instantaneous picture of the WV variability within an individual swath. The WV data are objectively analyzed along individual Geosat tracks and are used to make realistic wet tropospheric range corrections to the altimeter SSH measurements. Evaluation of the WV corrections along each track allows us to identify large WV

gradients, classify them according to their magnitude and range, and determine the frequency with which they occur on the same time and space scales as the ocean feature of interest. In addition, by analyzing the SSH data both before and after the wet tropospheric correction is applied, we can quantify how frequently the presence of WV changed the physical interpretation of the altimeter data. The data sources, analysis methods, results, and conclusions are presented in the following sections.

SATELLITE DATA SOURCES

Altimeter Data

The March 1985 Geosat launch represented the first U.S. altimeter in space since the short-lived Seasat mission. Numerous Seasat studies had looked into various aspects of oceanographic mesoscale and monthly signals and variability [Cheney, 1982; Bernstein *et al.*, 1982; Menard, 1983; Thompson *et al.*, 1983], but they were limited due to the 3-month data base. Geosat (similar in most respects to the Seasat altimeter) thus provided the extended time series required to determine the long-term basin-scale oceanic changes. More importantly for this study, it provided a continuous ground track of reliable SSH measurements that could be used to help locate ocean fronts and eddies. Unfortunately, Geosat is a single-sensor satellite that provides measurements of ocean topography only and, unlike Seasat, does not produce coincident WV measurements.

The GOAP at NORDA was the first effort to routinely process and analyze altimeter data in real time and follow up the natural evolution begun with earlier Seasat Gulf Stream work [Cheney, 1982]. Figure 1a exhibits the 17-day repeat track spacing available as part of the Geosat Exact Repeat Mission. Altimeter data along these tracks were used in the GOAP study in conjunction with satellite infrared imagery and available in situ observations to extract Gulf Stream front and eddy information [Lybanon and Croux, 1987]. Weekly maps of ocean frontal features were generated by extracting the 30- to 150-cm signals associated with warm- and cold-core rings and the north and south wall of the Gulf Stream.

Error sources (Table 1 [after Lybanon and Croux, 1987]) were not normally a significant hurdle to overcome, since Gulf Stream ocean signals were dominant in magnitude within the mesoscale spatial domains. Some problems were noted with ring detection [Hawkins and Smith, 1986], particularly older cold-core rings that maintained faint signals and rings that were sampled near their edges rather than across their centers. However, sufficient corrections were generally made to permit accurate interpretation of the data, especially in this major western boundary current regime. However, the main purpose of this paper is to report the impact of wet tropospheric corrections on SSH values in a region of very weak ocean frontal signatures, particularly, for the NEPAC area along the Geosat tracks shown in Figure 1b. Since it is generally accepted that the altimeter SSH measurements exhibit an engineering noise level near 3 cm [Sailor and LeSchack, 1987], it should be possible to detect ocean features that exhibit weaker signals than those in western boundary currents, particularly if the correction for the WV can be made.

The Geosat data are telemetered to the Earth-receiving

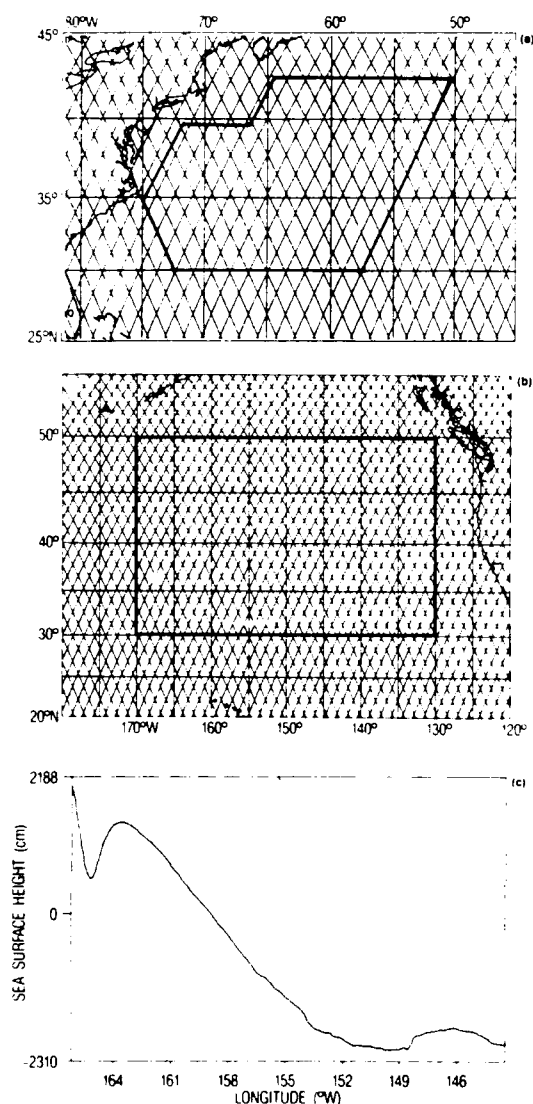


Fig. 1. Geosat 17-day repeat tracks from the Exact Repeat Mission. (a) The GOAP research area is outlined in the northwest Atlantic. (b) Geosat tracks in the NEPAC research area. (c) Mean surface profile computed along Geosat track A58.

station at the Applied Physics Laboratory Johns Hopkins University, twice daily. Minor processing is done before the data records are transmitted to NORDA and the Naval Oceanographic Office at Stennis Space Center. Minimal processing produces ocean surface wind speed, significant wave height, and sea ice products that are relayed to the Fleet Numerical Oceanography Center in Monterey, California. More accurate ephemeris data from the Navy Astronautics Group arrive within 24 hours and are then incorporated to help produce SSH height values. The mean surface along a repeat track is determined by averaging data from multiple passes along the same track (usually over a period of at least 1 year). The mean surface is then subtracted from the individual tracks to form SSH residuals. Corrections are also made for orbit errors, and the tilt and bias are removed from the SSH residual data before they are used for mesoscale interpretation.

Note that the computation of residuals by subtracting a mean surface from the altimeter data removes not only the

TABLE 1. Geosat Measurement Uncertainty

Error Source	Uncertainty (σ)		
	Baseline Mission, cm	Extended Mission, cm	Wavelength of Error, km
<i>Altimeter</i>			
Instrument noise	2.0	2.0	
Bias drift	2.0	2.0	many days
Time tag	0.2	0.2	20,000
Tracker bias	2.0	2.0	200–1,000
<i>Media</i>			
Electromagnetic bias	2.0	2.0	200–1,000
Skewness	1.0	1.0	200–1,000
Troposphere (dry)	0.7	0.7	1,000
Troposphere (wet)	6.0	3.0	200
Ionosphere	4.0	4.0	<1,000
<i>Orbit</i>			
Gravity	80.0	50.0	>10,000
GM	2.0	2.0	10,000
Atmospheric drag	10.0	10.0	10,000
Troposphere	1.0	1.0	10,000
Solar radiation pressure	10.0	5.0	10,000
Earth albedo	2.0	1.0	10,000
Earth or ocean tides	1.0	1.0	10,000
Station or spacecraft clocks	10.0	10.0	10,000
Higher-order ionosphere	5.0	5.0	10,000
Root Sum of Squares	83.0	54.0	

Major assumptions for the baseline mission are (1) TRANET tracking system, 40 stations; (2) TRANET ground station oscillators perform to specifications; (3) altimeter data averaged over 1 s; (4) $H_{1/3} = 2$ m, wave skewness = 0.1; (5) limited tuning of gravity field with Geosat TRANET data; (6) 800-kilometer altitude; (7) No anomalous data and no rain; (8) ± 3 mbar surface pressure from weather charts; and (9) 100- μ s spacecraft clock. Major assumptions for the extended mission are the same as for the baseline mission, but with (1) improved gravity, station location, and drag models based on Geosat tracking and (2) use of water vapor correction from SSM/I.

geoid but also the mean circulation. This does present the possibility that the residual circulation signal is somewhat reduced if it coincides with the mean circulation in the area. How often this actually occurs, we cannot say. However, this method for computing the residuals seems to be the least worrisome. If two collinear tracks were differenced, then we would have to be concerned about the effect of WV path lengthening on both tracks; if a synthetic geoid were used, then we would need to address the errors in the model used to produce the geoid. An example of the mean surface in the NEPAC area is shown in Figure 1c. Note that the scale of the gradient associated with this mean surface is several orders of magnitude larger than that used to distinguish ocean fronts in this area.

Water Vapor Data

The SSM/I is a seven-channel, four-frequency (19, 22, 37, and 85 GHz), passive microwave sensor flown aboard the polar-orbiting DMSP platform [Hollinger, 1989]. The 1394-km swath (roughly twice that of preceding sensors) and high-resolution spot sizes (Table 2) indicate several advantages this sensor has over the SMMR flown on Seasat and Nimbus 7. However, even the large SSM/I scan requires 3–5 days to fully cover the global oceans, thus leaving data gaps over shorter time frames.

TABLE 2. SSM I Channel Spatial Resolutions

Channel Frequency, GHz	Polarization	Effective Field of View, km	Scene Station Spacing, km
19.350	vertical	55.2	25.0
	horizontal	55.1	25.0
22.235	vertical	48.6	25.0
	horizontal	32.2	25.0
37.000	vertical	32.7	25.0
	horizontal	14.8	12.5
85.500	vertical	14.8	12.5
	horizontal	14.8	12.5

The SSM I can measure many atmospheric and oceanographic environmental parameters: sea ice (edge, concentration, and distinction between first-year and multiyear ice), WV, surface wind speed, cloud liquid water, rain rate, etc. The SSM I channels are particularly well suited to retrieve total columnar or vertically integrated WV as noted by the long heritage of similar space sensors. The SSM I's superior 25-km resolution should permit the best depiction yet of the horizontal variations in the WV distribution associated with atmospheric frontal systems.

Past efforts to validate satellite-derived WV retrievals have focused on the use of ocean weather ship and island radiosondes [Taylor *et al.*, 1981; Lipes, 1982; Chang *et al.*, 1984; Tapley *et al.*, 1984]. This data base is typically small and requires special efforts to gather enough temporal and spatial matchups to represent a significant statistical sample. Most studies include less than 100 radiosonde versus satellite sensor comparisons, but they typically indicate that the quality of the remotely sensed WV closely matches that of the radiosonde values. The accuracy of the radiosonde measurements is of the order of 1.7 kg m^{-2} [Taylor *et al.*, 1981].

Progress in sensor and algorithm development is shown by improved performance over the last 12 years and is reflected in the high-quality DMSP SSM I retrievals. As stated, the latest findings of Alishouse *et al.* [1990] show that a global algorithm now provides WV to an accuracy of 2.4 kg m^{-2} . Similar findings were made by F. Wentz (personal communication, 1989), who has processed over 1 year of SSM I data for NASA projects and computed the accuracy of the WV values as approximately 3.0 kg m^{-2} .

The Wentz data are incorporated in our study, since they represent the first lengthy SSM I data set available to test the capabilities of this sensor's wide swath and high spatial resolution in defining WV gradients that may adversely impact altimeter SSH studies. The brightness temperatures at 19 and 22 GHz were combined to derive the precipitable water. These WV measurements (in kilograms per square meter) were converted to altimeter wet tropospheric corrections by multiplying by the scalar quantity, $0.00636 \text{ m}^3 \text{ kg}^{-1}$ [Tapley *et al.*, 1982]. Further refinements of this conversion factor by comparison with a larger radiosonde data set indicated little change in the value selected, especially in mid-latitudes [Tapley *et al.*, 1984]. Thus the individual SSM I measurements of the precipitable water, ranging from under 10 kg m^{-2} to over 60 kg m^{-2} , were changed into altimeter path length corrections expressed in centimeters, extending from near 0 to almost 40 cm.

There is only a small error inherent in this method

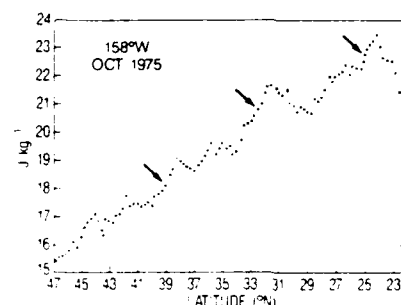


Fig. 2. Sea surface dynamic height perturbations (relative to 1500 dbar) from north to south along 158°W, derived from in situ cruise data in October 1975 [after Roden, 1977]. A 1 kg m^{-2} perturbation is equivalent to 10 cm of sea surface height. Arrows indicate mesoscale ocean features.

Multiplying the rms WV error (3.0 kg m^{-2}) by 0.00636 generates a SSH correction error near 1.9 cm. This measurement inaccuracy is well within the tolerance needed to map the 0- to 40-cm WV correction within the NEPAC grid sector. Also, since the conversion factor is a constant, a direct linear relationship exists between the wet tropospheric correction gradients and the actual gradients in the atmospheric WV.

DATA ANALYSIS

The NEPAC area is a suitable location for testing the limits on the use of altimeter data for detecting mesoscale ocean features. Figure 2, an example of the SSH variability in this area, was derived from in situ cruise data [Roden, 1977]. Several fronts can be identified by the rather sharp increase in the height perturbations (from north to south) of less than 10 to near 30 cm over 100–200 km. Thus the SSH variability here is small compared with that found near the Gulf Stream, which typically contains signals of 50–150 cm over the same distance.

To determine how WV path lengthening affected the usefulness of the altimeter data, we obtained SSM I WV data for July–September 1987 and also for portions of February 1988. This data set provided observations from summer, early fall, and winter. Several cases were selected for study by using the sea level–pressure surface analyses from the National Meteorological Center (NMC) to identify days when a strong atmospheric front was present in the area of interest. The largest WV gradients are normally associated with such atmospheric frontal systems [McMurdie and Katavrov, 1985], so the selected days provided an initial look at potential worst case scenarios.

After converting the WV data to WV corrections, the corrections were objectively analyzed to produce a uniformly gridded, two-dimensional field at 1.0° resolution. The area encompasses 30° to 50°N and from 130° to 170°W. This area coincides with the area for which the mean surface has been computed. A simple objective analysis scheme was used for the interpolation, where the weight of each data point was first determined, following Cressman [1959], from

$$w = \frac{R^2 - d^2}{R^2 + d^2} \quad (1)$$

where R is the specified data search radius, d is the distance of each data point from the analysis grid point, and w is the

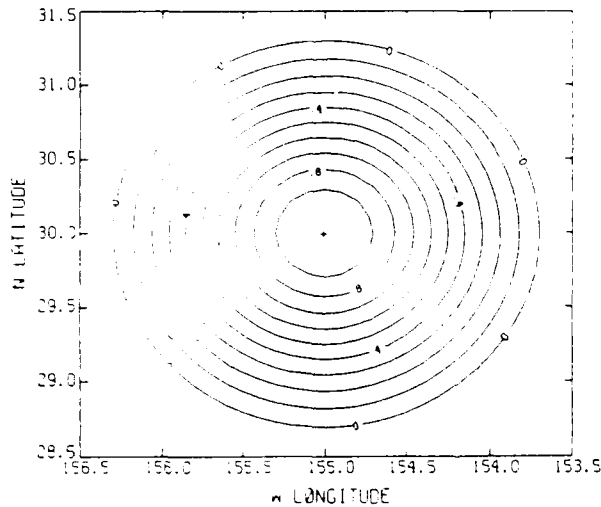


Fig. 3. Weighting function chosen for the data analysis scheme $w = (R^2 - D^2)/(R^2 + D^2)$. Contours represent the weight w computed as a function of distance D from a sample analysis point at 30°N, 155°W, given a search radius R of 1.3.

relative weight assigned to each data point. The final weights W_i are computed by normalizing the relative weights:

$$W_i = \frac{w_i}{\sum_{i=1}^N w_i} \quad (2)$$

where N is the number of data points within a distance R of the grid point. The analyzed WV correction V at the grid point is then determined from the linear combination

$$V = \sum_{i=1}^N W_i v_i \quad (3)$$

where v_i is the computed correction and W_i is its associated weight computed in (2).

Newer, more sophisticated analysis techniques, such as optimum interpolation, are difficult to apply to this problem. Use of optimum interpolation, for example, requires knowledge of the proper correlation function and spatial correlation scales of the target field. Although meteorologists have used this technique for years to analyze atmospheric moisture (in the form of relative or specific humidity), they use wind speed and wind direction fields to specify the necessary statistical functions [DiMego, 1989]. Since access to this kind of information was not readily available, we chose the simple scheme described above, which is basically a nonlinear inverse distance-weighting scheme (Figure 3).

As long as R is chosen intelligently, this type of objective scheme will produce interpolated fields that are smoother than the original observations. For the two-dimensional analysis, R was selected to be 1.3 times the grid increment of 1.0°. This value allows sufficient overlap of the data search areas at adjacent grid points and thus does not induce subgrid-scale features into the data. Rather than simply extrapolate the nearest one or two measurements to the given location, many observations are incorporated into the analytical solution. Thus the amount of random noise is reduced, and the resulting fields are representative of the grid scale being analyzed.

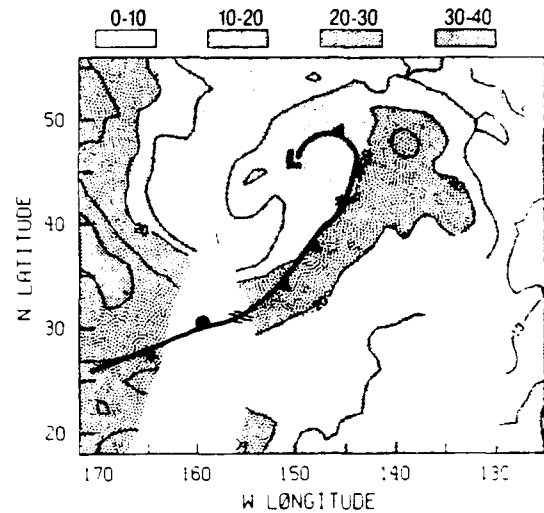


Fig. 4. Water vapor (WV) correction field analyzed using SSM/I vapor data from 0200 UT to 1600 UT, August 1, 1987. Contours are every 5 cm. Darker shades represent higher WV content. The atmospheric frontal position is valid at 0000 UT on the same day.

To qualitatively validate the analysis scheme, the two-dimensional WV correction fields were plotted and compared with the NMC surface atmospheric frontal positions closest in time to the SSM/I data. In all cases, agreement between the maximum WV gradient locations and the positions of the atmospheric fronts was extremely close. An example (Figure 4) shows a band of moist air along the cold front, which wraps around and behind the low pressure center and which contrasts sharply with the cold, dry air behind the front. This pattern is exactly what would be expected, given Bjerknes' [1919] classical cyclone model definition. Similar patterns have also been shown quite clearly in studies by McMurdie and Katsaros [1985], Katsaros and Lewis [1986], and McMurdie et al. [1987]. This relationship between the atmospheric systems and the maximum WV content and variability was observed repeatedly in our data. Thus we are confident that the analyzed WV corrections are indicative of the real-time synoptic atmospheric moisture patterns.

Within a given 24-hour period, three ascending and three descending SSM/I swaths passed either completely or partially through the NEPAC region. While the exact times vary somewhat, the data provided by descending passes were from around 0200 UT to 0700 UT and the ascending passes were between 1400 UT and 1900 UT (Figures 5a and 5b). The time separation of the swaths is approximately 1.5 hours. As illustrated, there are data coverage gaps as far north as 54°N. Although the analysis scheme partially fills in the data-void areas, it cannot extrapolate information any farther than the specified search radius, which is approximately 145 km. Thus in some cases, data from both the ascending and descending swaths were blended by the analysis, with no change in the data weights as a function of time. This procedure improves the amount of coverage in the area (Figure 5c) but can create other problems, particularly if the atmospheric system is rapidly moving.

Figure 5 demonstrates significant differences between the ascending and descending swaths analyzed separately and the sets blended together. The most notable difference is in the position and shape of the maximum WV correction

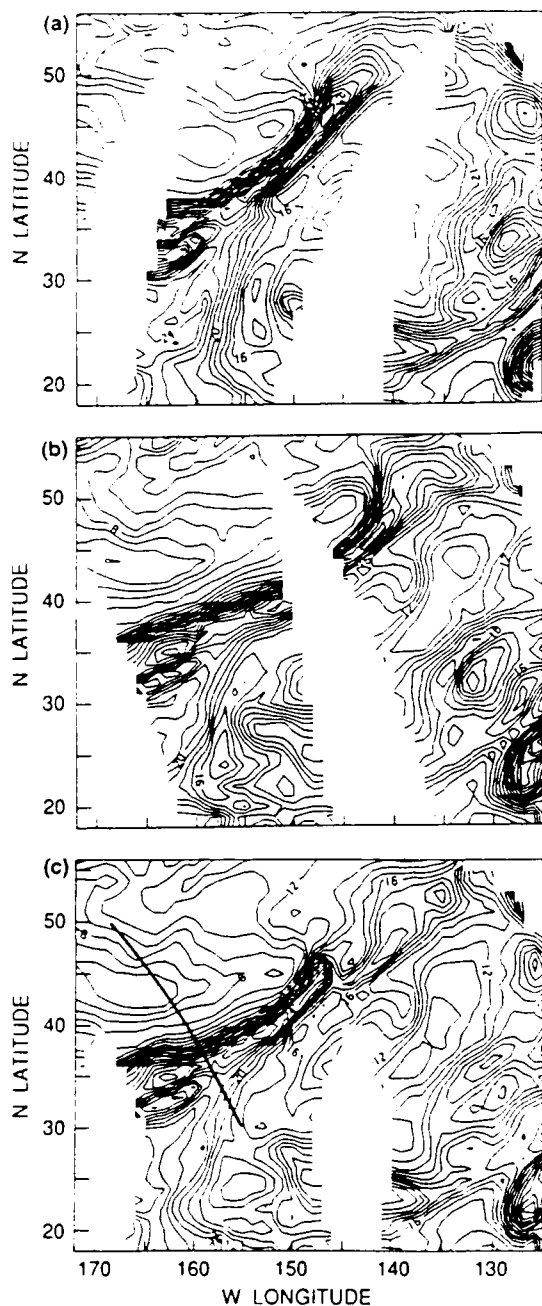


Fig. 5. WV correction fields analyzed using SSM/I data on July 12, 1987. Contours are every 1 cm. (a) Descending swaths only, from 0300 to 0700 UT. (b) ascending swaths only, from 1400 to 1800 UT. (c) descending and ascending swaths blended together. The 1900 UT Geosat track is shown crossing the strong gradient in the field.

gradient as the sharp gradient associated with the cold front around 150°W, 45°N, shifted southeastward as the front advanced to the east (Figures 5a and 5b). The northern portion of the front near the low pressure center moved more rapidly than the trailing end of the front. As a result, the northern edge of the blended WV correction field introduced a false gradient around 148°W, 45°N, while oversmoothing the gradient north of this point (Figure 5c). This problem will be addressed more thoroughly in the next section.

The original SSM/I data, not the previously analyzed two-dimensional field, were used to compute the WV cor-

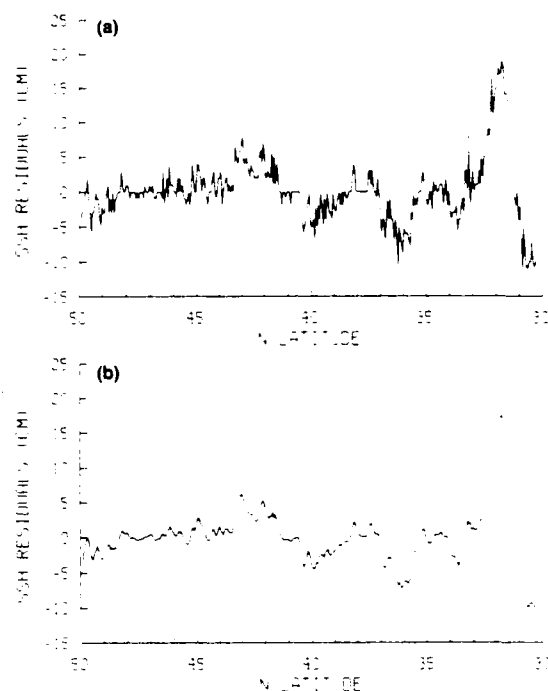


Fig. 6. Altimeter sea surface height (SSH) residuals along the 1900 UT Geosat track on August 1, 1987. (a) Original unsmoothed SSH data. (b) Smoothed SSH data.

rections along a given altimeter track. The same analysis technique was applied, but the analysis points in this case were positioned at exactly the same location as each altimeter footprint. The average distance between altimeter points is approximately 7 km, while the SSM/I data has a resolution of 25 km; therefore a search radius considerably larger than the separation of the analysis points was necessary. A 50-km search radius was selected to allow several SSM/I measurements to be included in the analysis at any one point, while still showing more detail in the one-dimensional WV correction curve than in the two-dimensional analysis.

Before the altimeter SSH residuals were corrected for WV, they were smoothed using a five-point filter (Figure 6). Thus each measurement was replaced by the average of the original value and the four closest measurements. This smoothing reduced the noise in the signal sufficiently without removing the features of interest. The wet tropospheric adjustment was then made by adding the analyzed path length correction at each footprint to the smoothed SSH value. In each case, the WV correction curve analyzed along the track was plotted in conjunction with the original and the corrected SSH data, allowing an easy visual comparison between the features in each representation.

The SSH data along a given track were examined to determine if the observed signal indicated the presence of an ocean front. This type of analysis is performed routinely as part of the NEPAC project, using the techniques described by Lybanon and Crout [1987]. Both infrared sea surface temperature data and altimeter data were used. Ongoing analyses have demonstrated that NEPAC fronts are characterized by an increase of 5–20 cm in the altimeter SSH residual (looking from north to south) over spatial scales of 100–200 km. Thus corrected and uncorrected SSH data for

each track were contrasted to identify the changes in the strength and location of the apparent ocean features. The results will be discussed in the next section.

INTERPRETATION OF RESULTS

The WV corrections plotted along the altimeter tracks generally fell into one of three categories. Some of the correction curves were relatively constant, exhibiting little change in WV along the track (Figure 7c). This was much more common in descending than ascending tracks (8 out of 11 flat tracks were descending), since the descending tracks more often parallel rather than cross the typical southwest to northeast orientation of the atmospheric cold fronts (Figures 7a and 7b). Other correction curves showed only broad gradients, where the change in WV was substantial but occurred over large spatial scales (Figure 8). This type of WV field did not affect the appearance of an individual ocean feature within the altimeter data under most circumstances. The third category includes those cases where the WV fluctuations are large, that is, where the analyzed WV correction increases or decreases rapidly over small spatial scales.

Here we defined a significant WV gradient as one where the wet tropospheric correction changed by at least 2.5 cm over 0.5° latitude, which is approximately 5 cm per 100 km. This gradient is comparable to the weak ocean frontal gradients that have been observed in the NEPAC region. We have also seen comparable gradients in the WV correction fields in numerous cases, which has several implications.

First, an apparent mesoscale ocean feature in the original altimeter SSH data may actually be due to abrupt changes in the WV field. An example is shown in Figure 9, where the front seen at 44°N in the original data is absent in the corrected altimeter data (Figure 9b). This apparent feature was due to the large WV gradients at 44°N (Figure 9a). Second, the WV may conceal the true ocean signal enough to completely mask the ocean front or eddy (see Figure 10). Note the front present at $39^\circ\text{--}40^\circ\text{N}$ in the corrected data that was not manifested in the original SSH data (Figure 10b). The front was suppressed by the presence of a strong WV gradient at the same location (Figure 10a). Third, the presence of WV may suppress the signal by a few centimeters, making it difficult to positively identify a feature. In the original altimeter data shown in Figure 11b, there is a possible front at 41°N . Once the wet tropospheric correction (Figure 11a) is applied to the data, this feature is more clearly identifiable.

As was already mentioned, one concern was the time difference between the altimeter measurements and the SSM/I data used to make the height correction. Since the largest WV gradients are associated with the atmospheric frontal system, the location of these gradients can be expected to change. Since the atmospheric fronts often move rapidly through this area, at speeds up to 40 km h^{-1} , there may be little continuity between the ascending and descending SSM/I passes (Figure 5). Furthermore, the WV field will undergo modification as the atmospheric system develops or ages [McMurdie and Katsaros, 1985]. Thus in most cases, the ascending swaths were analyzed separately from the descending swaths, and the resulting two-dimensional fields were compared with the correction field produced by blending both sets of swaths. The same altimeter track was also

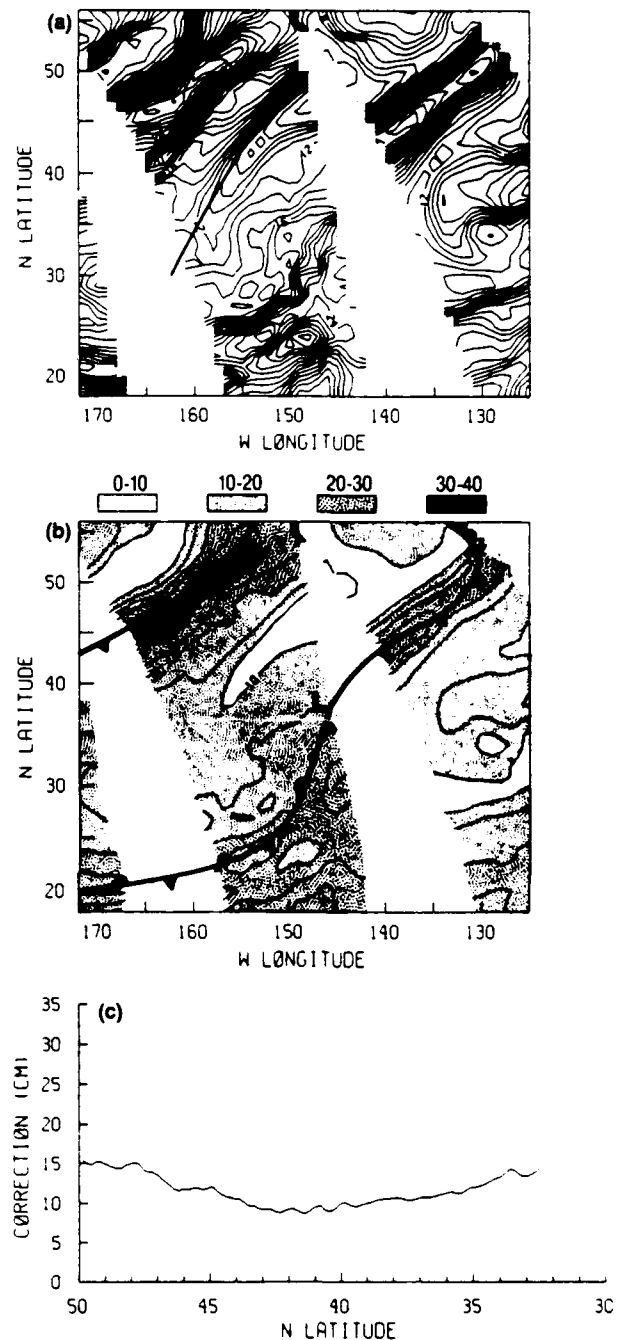


Fig. 7. WV corrections analyzed using SSM/I data on September 1, 1987. (a) Two-dimensional field, contoured at 1-cm intervals, with position of 2100 UT Geosat track shown. (b) Two-dimensional field, contoured and shaded at 5-cm intervals, showing the 1800 UT position of the atmospheric frontal systems. (c) One-dimensional correction curve analyzed along the 2100 UT Geosat track, using SSM/I data between 1600 and 1700 UT on the same day.

corrected using these different combinations of analyzed SSM/I data.

When the atmospheric fronts were either stationary or slowly moving, the 24-hour blended field closely resembled the two-dimensional fields produced from the different passes (Figures 12a, 12b, and 12c). In such cases, objectively combining both the ascending and descending swaths provided better data coverage, left fewer gaps in the cor-

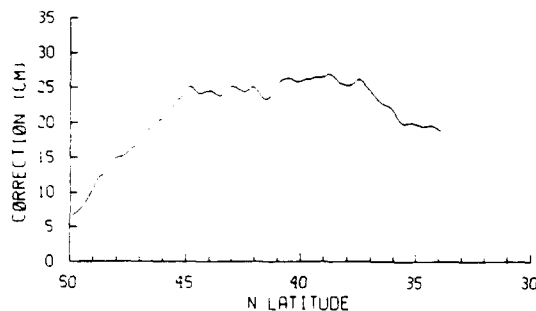


Fig. 8. WV corrections, in centimeters analyzed along the 0600 UT Geosat track on September 12, 1987, using SSM/I data between 0400 and 0500 UT.

rected altimeter data, and had little effect on the interpretation of the mesoscale features present. However, if the weather systems move rapidly or change characteristics, as was the case on September 8–9, 1987 (Figures 13a–13d), then the blending of WV data from multiple passes becomes highly questionable.

For example, the bottom curve in Figure 14c shows the original altimeter data measured along a track at 0700 UT on September 8 (Figure 14a). The top curve in Figure 14c represents the SSH, where the wet tropospheric correction was made using SSM/I data (Figure 14b) taken between 0400 UT and 0500 UT on the same day, almost coincident with the altimeter data. The broad, depressed area between 48°N and 42°N is not present in the corrected data, nor is the apparent front at 42°N. The broad depression in the SSH data was due

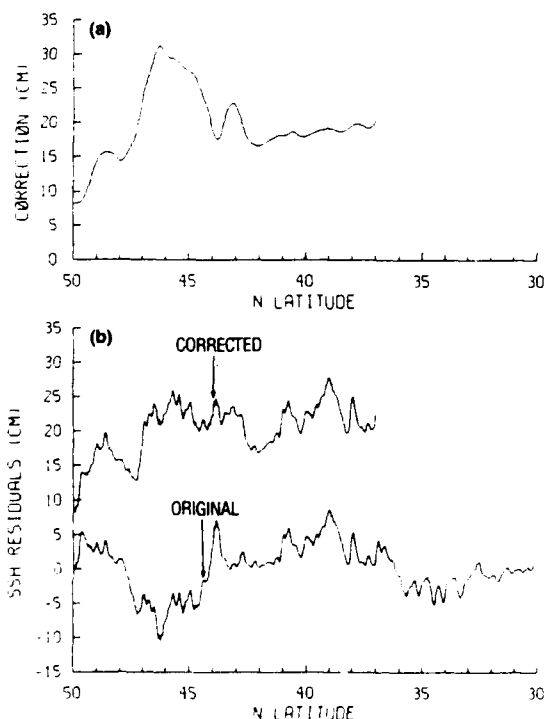


Fig. 9. WV correction applied to the 0700 UT Geosat track on September 9, 1987. (a) WV corrections (in centimeters) analyzed along the track using SSM/I data between 0500 UT and 0600 UT. (b) Altimeter SSH residuals, in centimeters, before and after the WV correction is made. Notice how the WV mimics an ocean feature at 44°N.

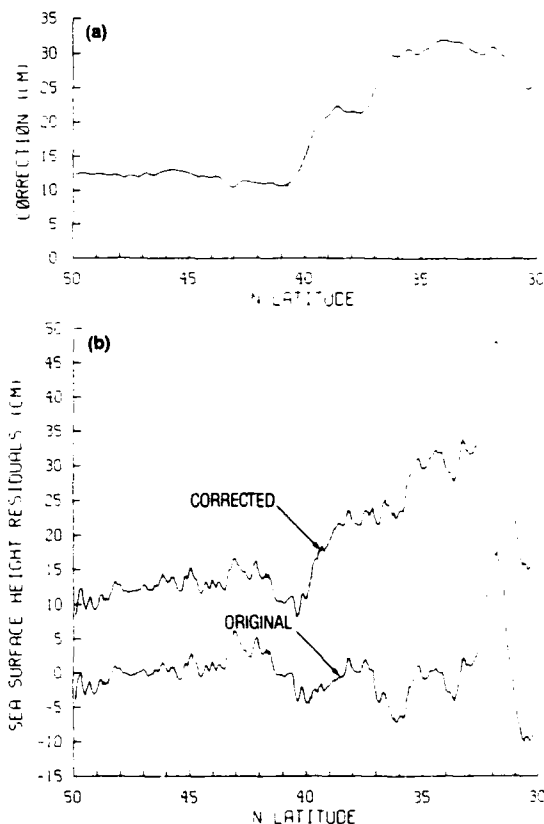


Fig. 10. WV correction applied to the 1900 UT Geosat track on August 1, 1987 (position plotted in Figure 12c). (a) WV corrections (in centimeters) analyzed along the track using SSM/I data between 0500 and 1200 UT. (b) Altimeter SSH residuals (in centimeters) before and after the WV correction is made. Notice how the WV masks an ocean feature at 39°N.

entirely to the band of moisture that was present along the stationary front (Figure 13a). The corrected data show an enhanced feature at 40.5°N, while the apparent feature at 42°N is greatly suppressed.

The same track was corrected using the SSM/I WV data sampled between 0400 UT and 0500 UT on the next day. By this time, the broad band of moisture had narrowed considerably (Figure 15a), and the maximum WV gradient had moved southeastward as the next cold front approached from the northwest (Figure 13c). Thus the peak in the WV correction along the track has both narrowed and shifted (Figures 15b and 14b). The resulting SSH data corrected with the September 9 WV data (Figure 15c) show significant differences from those corrected using near-real-time data. In fact, the wet tropospheric correction induced a strong signal between 43°N and 45°N. This feature is not present in the near-real-time correction (Figure 14c). Thus it is a false signature due entirely to the use of nonsynoptic WV data to make the wet tropospheric range correction.

These examples clearly indicate that the error in the altimeter signal due to the presence of WV is potentially a serious problem affecting the detection and interpretation of NEPAC mesoscale fronts. To determine the frequency of the problem, the data were analyzed for September 1987, at the transition from summer to fall. During this time, the contrasts between the cold, dry air masses and the warmer, moist air masses in the mid-latitudes are very strong. Thus

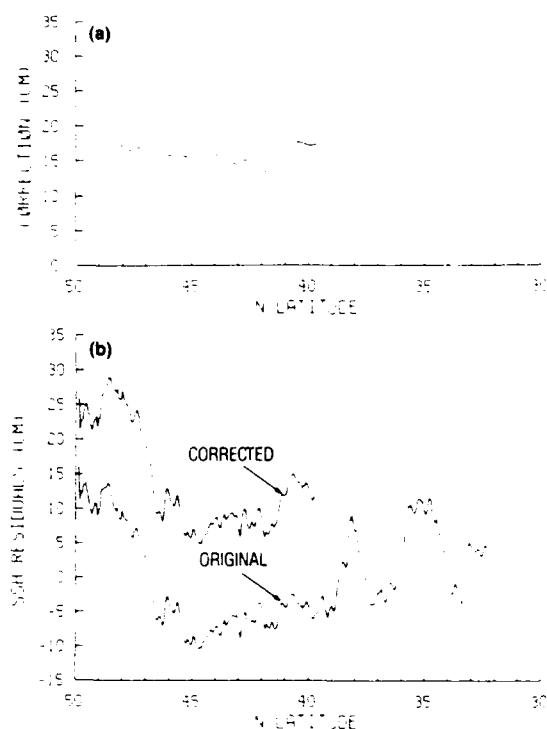


Fig. 11. WV correction applied to the 2200 UT Geosat track on September 17, 1987. (a) WV corrections (in centimeters) analyzed along the track using SSM I data between 0900 UT and 1600 UT. (b) Altimeter SSH residuals (centimeters) before and after the WV correction is made. Notice how the WV correction enhances an ocean feature at 41°N.

we expected that large WV gradients would accompany the meteorological systems. Furthermore, we noted that the surface pressure analyses revealed at least one atmospheric front within the NEPAC grid every day of the month. Once again, the positions of these fronts were compared with the objectively analyzed, two-dimensional, WV correction fields, and the atmospheric systems were consistently associated with the largest WV correction gradients.

Geosat tracks that passed through the NEPAC grid area during September 1987 were processed, and the SSM I WV data were used to make the wet tropospheric correction. On the basis of visual inspection, each track was classified according to the strength of the maximum WV correction gradient along the track. Three general categories were defined: correction curves with flat gradients, broad gradients, and significantly strong gradients. The last category was further divided into three classes, representing the magnitude of the change computed in reference to 1.0° latitude (roughly 100 km). These classes were 5.0–10.0 cm, 10.0–20.0 cm, and greater than 20.0 cm. Thus each track was assigned to one of five categories. The results are shown in Figure 16. Note that of the 65 tracks processed in September, almost 75% of the tracks were associated with WV correction gradients defined as strong enough in strength to warrant concern.

This analysis differs from that made by *Monaldo* [this issue] because we studied the WV correction curve for each track and selected the endpoints over which the more abrupt changes were observed. The wet tropospheric correction gradient was initially computed over this selected distance.

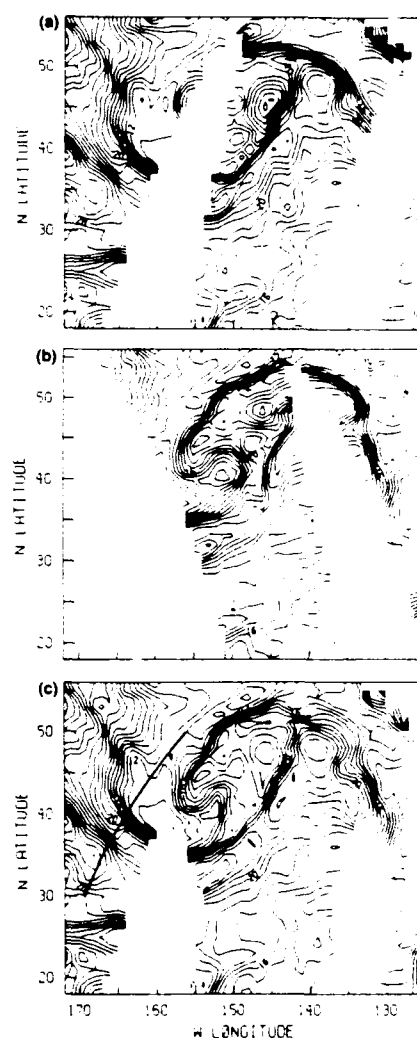


Fig. 12. WV correction fields analyzed using SSM I data on August 1, 1987. Contours are every 1 cm. (a) Descending swaths only, from 0200 to 0700 UT. (b) ascending swaths only, from 1400 to 1800 UT. (c) descending and ascending swaths blended together. The position of the 1900 UT Geosat track is shown crossing the strong gradient in the field. (See Figure 10 for correction of track.)

Each measured gradient was subsequently converted to a magnitude relative to 100 km for comparison purposes. *Monaldo* arbitrarily divided the tracks into fixed increments of 100–1000 km and computed the gradients over those fixed intervals. It is unlikely that this technique would capture the true WV gradient strengths, since the gradients of interest could easily extend across the fixed endpoints or fall completely in between them. Furthermore, *Monaldo* based his conclusions on altimeter signals that were stronger than 10 cm per 100 km, but gradients of 5 cm per 100 km may be important in some areas.

Our study identified the potentially significant gradients in each correction curve: 128 measured gradients in the 65 tracks. When classified according to strength, 76% of the gradients were in the 5.0–10.0 cm per 100 km range, with 23% in the 10.0–20.0 cm per 100 km range (Figure 17). Only two gradients exhibited signatures stronger than 20.0 cm relative to 100 km. In addition to computing the gradients relative to 100 km, the gradients in each class were grouped

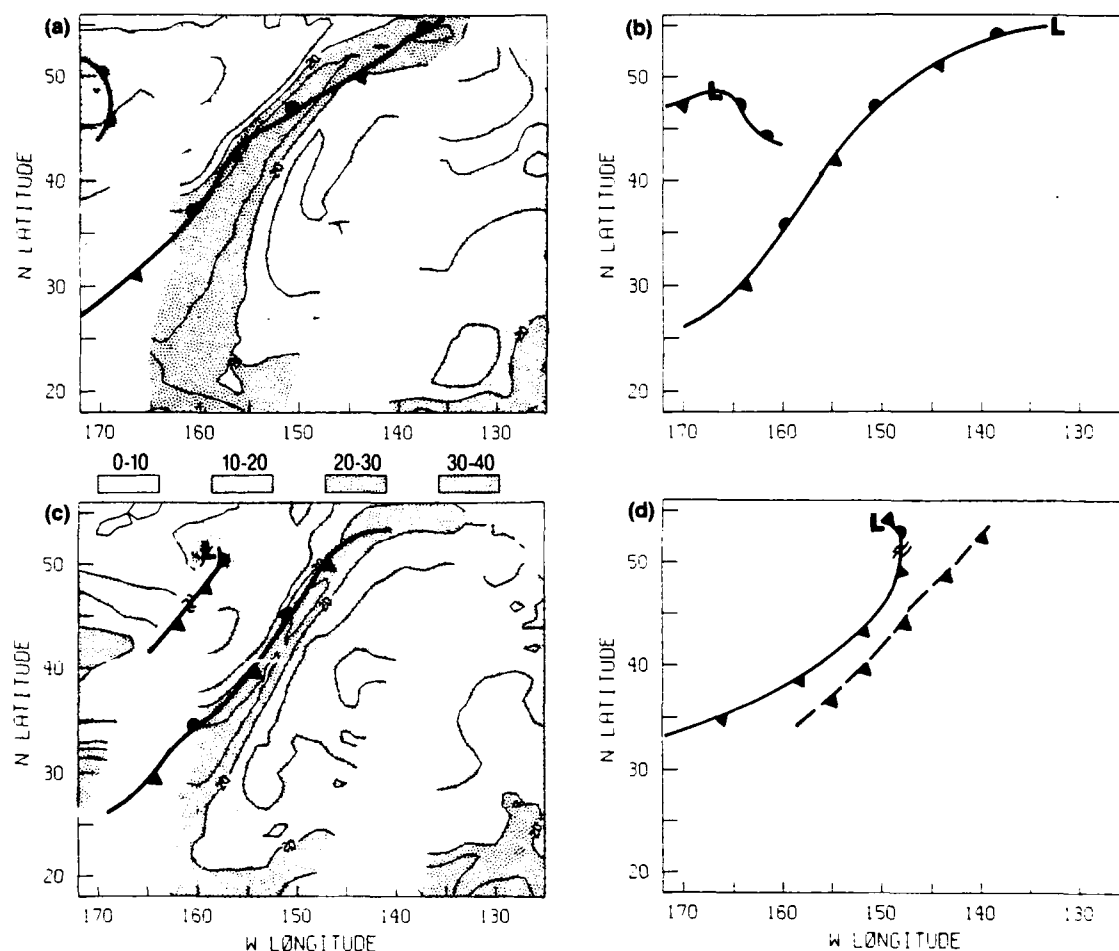


Fig. 13. Movement of atmospheric frontal systems as depicted by the NMC's surface pressure analyses. Background fields are SSM/I WV corrections from descending swaths on same day, contoured and shaded at 5-cm intervals. Darker shades represent higher WV content. (a) September 8, 1987, 0600 UT. (b) September 8, 1987, 1800 UT. (c) September 9, 1987, 0600 UT. (d) September 9, 1987, 1800 UT.

according to the distance over which the gradient strength was maintained, that is, the original measured distance. Table 3 illustrates that the majority of the WV correction gradients were sustained over 50 to 150 km, well within the range considered significant for ocean mesoscale features in the NEPAC region.

The final stage of the analysis is qualitative. Since the ultimate goal of the project is to use the altimeter data to locate the mesoscale ocean features, the impact of the wet tropospheric correction on the interpretation of the altimeter data is crucial. Thus each SSH residual track was subjectively analyzed to locate mesoscale fronts, which are generally characterized by a rise in the SSH residual proceeding from north to south along the altimeter track. Each apparent feature was noted, and the corrected and uncorrected SSH data along each track were compared. The observed differences in the apparent fronts were classified in one of three ways. If the feature was present in the original SSH data but not in the corrected data, then it was labeled a "false" signal. That is, the WV mimicked an ocean feature that was not really there. If the feature was not present in the original altimeter data but was identified in the corrected data, then it was classified as a "true ocean front" that was masked by the presence of atmospheric WV. If some hint of the feature was present initially and the feature was clearly identifiable

in the corrected SSH data, then it was classified as an "enhanced" feature.

Of the 65 tracks processed, 31% contained false signals. At least one feature was completely masked by WV gradients in 35% of the tracks, and ocean signals were enhanced in 46% of the tracks (Table 4). When each feature was tallied individually, a total of 221 potential fronts were noted in the 65 tracks. Of these, approximately 128 features were not significantly contaminated by WV. However, 93 features (44% of the total) were interpreted differently as a result of making the wet tropospheric correction to the track. Of these, 22% were mimicked features, 28% were masked features, and 50% were enhanced features (Table 5). Thus if masking and enhancing are considered to be the same process and differ only in the magnitude of the change, then it appears that the obfuscation of the true ocean signal by the WV gradients is more of a problem than the so-called false signal, where the WV gradient is mistakenly interpreted as an ocean front or eddy.

Some studies [e.g., Monaldo, this issue] have been interested only in gradients that are equally as strong as the ocean signal. Thus the situation where the WV gradient is mimicking an ocean feature is of more concern. Masking of features is addressed only indirectly. That is, the WV correction gradient would have to occur at exactly the same strength

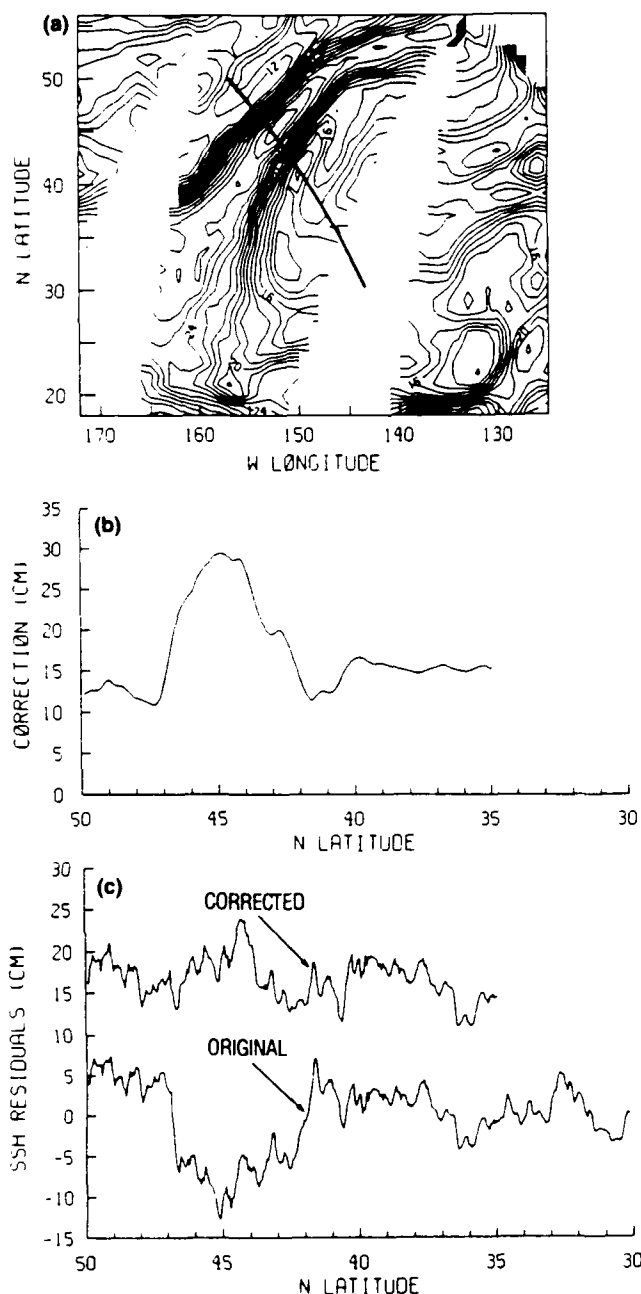


Fig. 14. WV correction applied to the 0700 UT Geosat track on September 8, 1987, using SSM/I data between 0400 and 0500 UT on the same day. (a) Two-dimensional correction field, contoured every 1 cm, showing the position of the track. (b) WV corrections (centimeters) analyzed along the track. (c) SSH residuals before and after the WV correction is made. The apparent ocean front at 42°N was largely induced by the WV.

and at exactly the same location as the SSH gradient to be considered significant. Granted, the latter situation would happen infrequently. For example, in our study, if we compare the number of mimicked and masked features to the total number of 221 observed features, we find that WV gradients mimicked ocean SSH gradients in 9% of the cases, while features were masked 12% of the time. These figures indicate that significant gradients in the WV corrections were approximately collocated with the ocean frontal gradients about 20% of the time.

However, when we include not only the coincident situa-

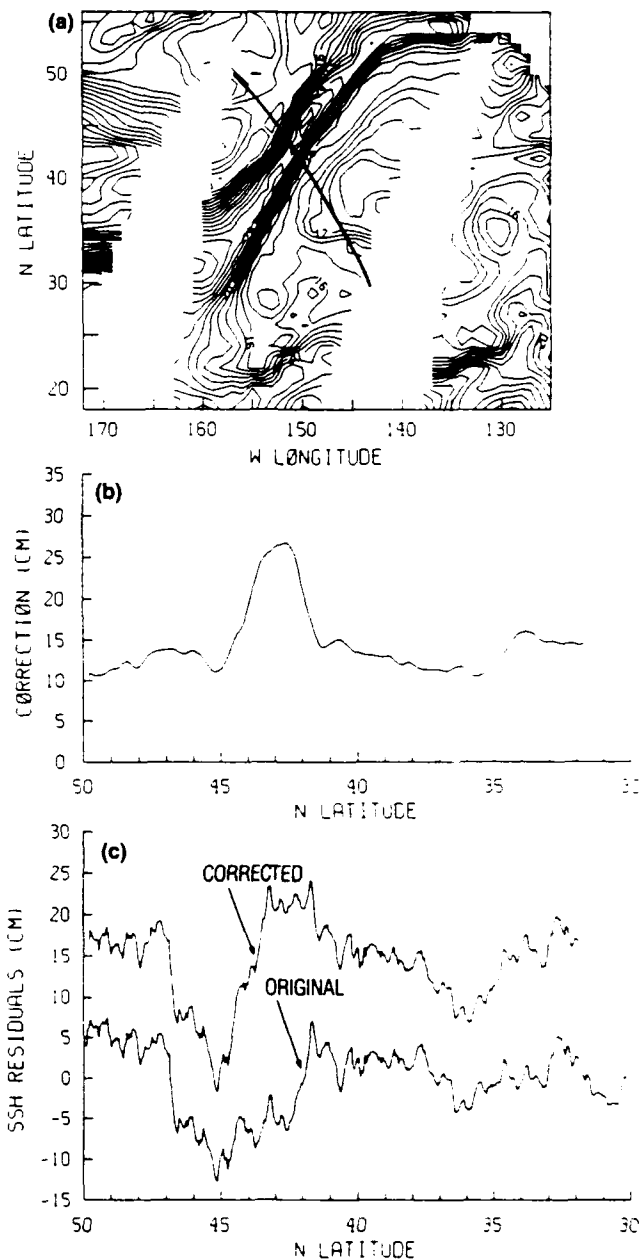


Fig. 15. WV correction applied to the same track as in Figure 14, but using SSM/I data between 0400 and 0500 UT on the next day, September 9, 1987. (a) Two-dimensional correction field, contoured every 1 cm, showing the position of the track. (b) WV corrections (centimeters) analyzed along the track. (c) SSH residuals before and after the WV correction is made. Notice how the corrected track differs from the one in Figure 14c. The WV data have induced a false ocean feature at 43–45°N.

tions but also those cases where the WV corrections modify the altimeter signal enough to alter the interpretation of the SSH data, the result is more far-reaching. Partly because we are using a fixed limit for determining the significant cases, features can be suppressed or enhanced by less than a 5-cm gradient in the WV correction. Thus changes in feature interpretation do not necessarily imply co-location of the strongest water vapor gradients with the strongest SSH gradients. Even an apparently insignificant WV correction

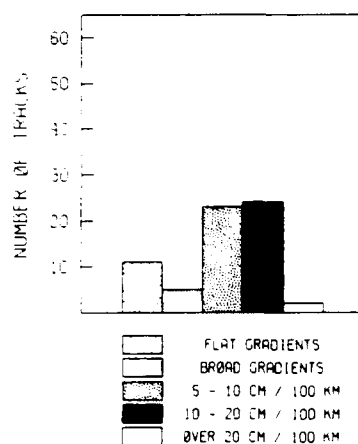


Fig. 16. Classification of the 65 total altimeter tracks into five categories based on the strength of the maximum WV correction gradient in the track. The number of tracks in each category is illustrated. The last three categories are considered significant, representing 75% of the total tracks.

gradient can alter feature identification. The large number of features affected by the WV is not surprising, considering that there are up to four weak ocean fronts in the NEPAC region, making it likely that at least one front will be affected by some portion of the atmospheric system.

CONCLUSIONS

Altimeter SSH data have proven to be a valuable tool for locating mesoscale fronts and eddies, particularly in western boundary current regimes where the SSH gradients are large. These data are especially useful when clouds inhibit the use of infrared imagery and when the ocean feature is submerged or does not have a strong SST signature. In the Geosat Exact Repeat Mission each location is viewed only once every 17 days. The distance between tracks is approximately 165 km at the equator. Thus for real-time oceanographic operations and applications, the information in each track is important. In an effort to extend the use of altimeter data to other areas where the SSH signal and variability are much lower, we have attempted to determine the importance of the wet tropospheric correction as a source of altimeter data error.

We used high-resolution (25 km) WV data from the DMSP SSM/I sensor to analyze WV correction fields for numerous Geosat tracks in the NEPAC region. This study is unique because it is the only work that has made time-coincident, wet tropospheric range corrections to actual SSH measurements along extended segments of altimeter tracks. The

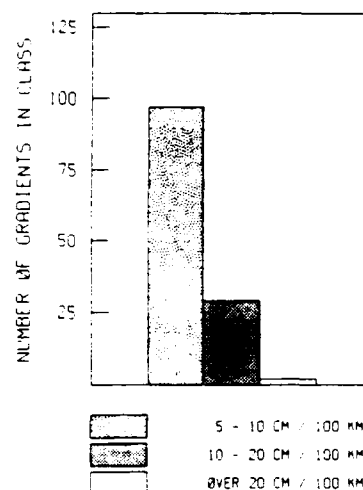


Fig. 17. Classification of the 128 significant WV correction gradients according to the gradient strength. The number of gradients measured in each class is illustrated.

interpretation of the resulting differences clearly shows that in the NEPAC area the WV correction can significantly alter the apparent positions of the mesoscale ocean features in the altimeter data.

In the NEPAC region we found that the WV gradients associated with atmospheric frontal systems are comparable in strength to the signals of the ocean fronts in this area, where changes as small as 5–10 cm over 100 km are considered significant. What this implies, of course, is that the WV gradient may mimic or mask the mesoscale ocean features of interest. Thus the interpretation of the altimeter SSH data in this region is uncertain without the wet tropospheric correction. Even a 2- to 3-cm enhancement of the SSH gradient could mean the difference between locating or not locating a particular feature. The situation is further complicated by the number of weak oceanographic fronts in this area, making it more likely that the WV gradient will affect at least one of the fronts. It also appears that the ascending tracks are affected more often than the descending tracks, since the ascending tracks cross the normal southwest to northeast orientation of the atmospheric cold fronts.

We have shown that the timeliness of the data is critical. Because the atmospheric fronts and their associated WV fields may move rapidly through this area, blending data from multiple passes can oversmooth or offset the gradients in the water vapor field, reducing the true impact of the WV on the ocean signal. Using SSM/I data that are too far removed in time from the altimeter data can also introduce

TABLE 3. Sustained Strength of Significant Water Vapor Gradients

Gradient Magnitude, cm/100 km	Spatial Scale of the Measured Gradient									
	0–50 km		50–100 km		100–150 km		>150 km		Total	
	Number*	Percent†	Number*	Percent†	Number*	Percent†	Number*	Percent†	Number*	Percent†
5–10	6	6.2	41	42.3	40	41.2	10	10.3	97	100
10–20	4	13.8	9	31.0	12	41.4	4	13.8	29	100
>20	0	0.0	1	50.0	0	0.0	1	50.0	2	100

*Out of 128 total measured gradients

†In reference to the total number of gradients of this magnitude

TABLE 4. Tracks with features Altered by Water Vapor

Type of Change	Number of Tracks*	Percent†
Enhanced features	30	46.2
Masked features	23	35.4
Mimicked features	20	30.8

*Out of 65 total tracks used for this study.

†In reference to total of 65 tracks.

false signals into the SSH data, which may be incorrectly interpreted as true ocean features. The scientific community would be best served by having a radiometer and an altimeter on the same satellite. With coincident measurements of WV and sea surface topography, we believe that the utilization of altimeter data can be extended to cases where the mesoscale ocean signals are weaker than those typically found in western boundary currents. The future European Remote Sensing Satellite (ERS-1) and Ocean Topography Experiment (TOPEX)/Poseidon altimeters both have bore-sighted radiometers that will permit this capability.

This study has concentrated on the NEPAC area, but the results shown here can likely be extended to other areas. Care must be taken, however, to assure that both the oceanographic and atmospheric conditions are similar; that is, the SSH gradients are weak and the atmospheric frontal systems are characterized by large air mass contrasts. Such areas might include, for instance, the north central and eastern Atlantic. A preliminary look at WV gradients in the northern Atlantic indicates that the wet tropospheric correction may be an unexpected source of error even at more northern latitudes [May and Hawkins, 1990]. But the relationship between the atmospheric and oceanographic conditions has been inadequately addressed in previous works. This question is particularly relevant in the Bisagni [1989] paper, since the study was limited to a small area in tropical latitudes east of a major continent.

Future work will pursue similar analyses for additional periods. This study concentrated on the month of September 1987, which is marked by strong air mass contrasts in the mid-latitudes. Data from other seasons may exhibit different properties. The winter season may be particularly interesting, as the capacity of the atmosphere to contain water vapor is diminished. Figure 18 illustrates a wintertime situation in the NEPAC sector. Note that significant gradients are still present in the WV correction field, even though the maximum is somewhat reduced and shifted southward from those seen during the summer-fall transition period. However, there is enough variability to encourage further study with a wintertime series of analyses.

TABLE 5. Ocean Features Altered by Water Vapor

Type of Change	Number of Features	Percent of Altered Features	Percent of Observed Features
Enhanced features	47	50.5	21.3
Masked features	26	28.0	11.8
Mimicked features	20	21.5	9.0
Total altered features	93	100.0	42.1
Total unaltered features	128		57.9
Total observed features	221		100.0

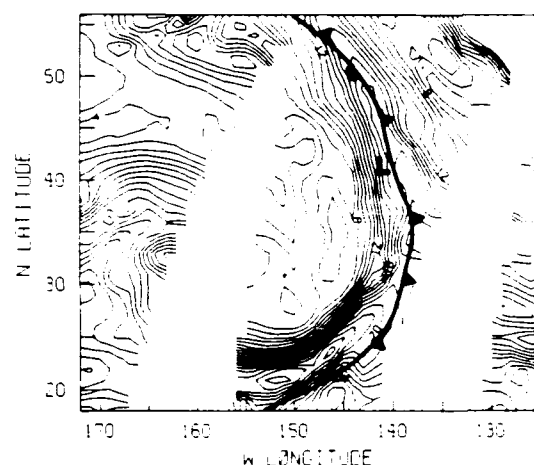


Fig. 18. Two-dimensional WV correction field analyzed using SSM/I data from 0200 UT to 0600 UT on February 23, 1988. The position of the atmospheric frontal system is valid at 1200 UT on the same day.

Since SSM/I WV data are the best available source for our current needs, more work needs to be done to evaluate their real potential. For example, we need to determine the temporal limits that should be placed on the use of SSM/I wet tropospheric corrections. These limits may be affected by the future launch of another DMSP platform with an SSM/I on board. Conceivably, data from two SSM/I could be available as soon as spring 1990. For the NEPAC research project, we have implemented software to access the Fleet Numerical Oceanography Center SSM/I data base and make near-real-time corrections to the altimeter SSH residuals before the data are used for frontal analysis in the NEPAC area. However, this solution is not fully satisfactory. Since we do not feel justified using WV data that are more than a few hours removed from the altimeter data, large portions of the tracks cannot be corrected.

We have made several assumptions in our data processing, which may or may not affect our conclusions. First, we have assumed that the formation of SSH residuals by subtracting a mean surface does not consistently reduce the signal of the mesoscale ocean features beyond detection. While the mean surface typically contains longer wavelengths, this assumption may not be valid for each individual case. Furthermore, we believe the objective techniques used to smooth and analyze both the altimeter SSH residuals and the SSM/I WV measurements reduce the random noise present in the original data while still showing the signals of interest. Thus our interpretations assume that the analyzed data accurately represent the physical phenomena. Finally, we are looking for ocean signals that are near the noise level of the altimeter. While we know that such weak features are present, we acknowledge that we are pushing the generally accepted limits of ocean feature detection.

These things considered, we still feel that the presence of WV is a serious hindrance to the use of altimeter data for mesoscale feature detection in areas where the ocean signal is weak and the SSH variability is low. We have shown that the wet tropospheric correction dramatically alters the appearance of the SSH residuals along Geosat tracks in the NEPAC region. While we have not shown that the corrected data are any more accurate than the uncorrected data,

intuition tells us that removing a known source of error from the original measurements will result in a more accurate product. Thus we leave it to a future study to make use of independent data sources, such as recently gathered bathythermograph measurements, to perform an extensive verification of the frontal positions in the corrected tracks.

Acknowledgments. Many people have contributed their time and ideas to this project. The SSM/I geophysical data were processed by Frank Wentz of Remote Sensing Systems, Santa Rosa, California. The SSM/I water vapor corrections were computed locally from the Wentz data by Nita Chase of NORDA and by Fred Abell, Sylvia Seal, and Bobby Grant of Sverdrup Technology. The Geosat altimeter data were processed by Conrad Johnson, NORDA, and Natalie Koennen, Sverdrup Technology. We must recognize our colleagues who have participated in the GOAP and NEPAC remote sensing efforts: Jim Mitchell, Matt Lybanon, and Doug May. Finally, we would like to thank Richard Crout of Planning Systems, Incorporated, for providing us with the benefit of his experience in analyzing altimeter data and for assisting in interpreting of the NEPAC altimeter SSH residuals. This work was supported by the Chief of Naval Operations (OP-096) and the Naval Space and Warfare Command under program element 63704N, Satellite Applications and Techniques (SAAT), A. E. Pressman, Program Manager, NOARL contribution JA 321:044:89. NORDA is now known as the Naval Oceanographic and Atmospheric Research Laboratory. This document has been reviewed and is approved for public release.

REFERENCES

- Alishouse, J., S. Synder, J. Vongsathorn, and R. Ferraro, Determination of oceanic total precipitable water from the SSM/I, *IEEE J. Geosci. Remote Sens.*, in press, 1990.
- Askne, J., G. Elgered, and H. Nordius, Atmospheric water vapour corrections for altimetry measurements, Proceedings of the International Geoscience and Remote Sensing Symposium, 1986, *Eur. Space Agency Spec. Publ., ESA SP-254*, vol. 3, 1543-1548, 1986.
- Bernstein, R., G. Born, and R. Whritner, Seasat altimeter determination of ocean current variability, *J. Geophys. Res.*, **87**, 3261-3268, 1982.
- Bisagni, J., Wet tropospheric range corrections for satellite altimeter-derived dynamic topographies in the western North Atlantic, *J. Geophys. Res.*, **94**, 3247-3254, 1989.
- Bjerknes, J., On the structure of moving cyclones, *Geophys. Publ.*, **1**(2), 1-8, 1919.
- Chang, H., T. Wilheit, and P. Gloersen, Global maps of atmospheric water vapor, cloud water, and rainfall derived from Nimbus-7 scanning multichannel microwave radiometer data: A case study, in *Proceedings, Oceanography From Space Symposium*, pp. 683-689, Plenum, New York, 1980.
- Chang, H., P. Hwang, T. Wilheit, A. Chang, D. Staelin, and P. Rosenkranz, Monthly distributions of precipitable water from the Nimbus 7 SMMR data, *J. Geophys. Res.*, **89**, 5328-5334, 1984.
- Chelton, D., K. Hussey, and M. Parke, Global satellite measurements of water vapour, wind speed and wave height, *Nature*, **294**, 529-532, 1981.
- Cheney, R., Comparison data for Seasat altimetry in the western North Atlantic, *J. Geophys. Res.*, **87**, 3247-3253, 1982.
- Cressman, G., An operational objective analysis system, *Mon. Weather Rev.*, **87**, 367-374, 1959.
- DiMego, G., The National Meteorological Center regional analysis system, *Mon. Weather Rev.*, **116**, 977-1000, 1989.
- Hawkins, J., and P. Smith, Effects of atmospheric water vapor on the detection of mesoscale oceanographic features from Geosat, *NORDA Rep. 126*, 21 pp., Nav. Ocean Res. and Develop. Activity, Stennis Space Center, Miss., 1986.
- Hollinger, J., DMSP special sensor microwave imager calibration validation, final report, 158 pp., Nav. Res. Lab., Washington, D. C., 1989.
- Katsaros, K., and R. Lewis, Mesoscale and synoptic scale features of North Pacific weather systems observed with the scanning multichannel microwave radiometer on Nimbus 7, *J. Geophys. Res.*, **91**, 2321-2330, 1986.
- Lipes, R., Description of Seasat radiometer status and results, *J. Geophys. Res.*, **87**, 3385-3395, 1982.
- Lybanon, M., and R. Crout, The NORDA Geosat ocean applications program, *Johns Hopkins APL Tech. Dig.*, **8**(2), 212-218, 1987.
- May, D., and J. Hawkins, Altimeter height corrections due to atmospheric water vapor in the Greenland-Iceland-United Kingdom (GIUK) gap (abstract), *Eos Trans. AGU*, **71**, 127, 1990.
- McConathy, D., and C. Kilgus, The Navy Geosat mission: An overview, *Johns Hopkins APL Tech. Dig.*, **8**(2), 170-175, 1987.
- McMurdie, L., and K. Katsaros, Atmospheric water distribution in a mid-latitude cyclone observed by the Seasat scanning multichannel microwave radiometer, *Mon. Weather Rev.*, **113**, 584-598, 1985.
- McMurdie, L., G. Levy, and K. Katsaros, On the relationship between scatterometer-derived convergences and atmospheric moisture, *Mon. Weather Rev.*, **115**, 1281-1294, 1987.
- Menard, Y., Observations of eddy fields in the northwest Atlantic and northwest Pacific by Seasat altimeter data, *J. Geophys. Res.*, **88**, 1853-1866, 1983.
- Monaldo, F., Path length variations caused by atmospheric water vapor and their effects on the measurement of mesoscale ocean circulation features by a radar altimeter, *J. Geophys. Res.*, this issue.
- Njoku, E., and L. Swanson, Global measurements of sea surface temperature, wind speed and atmospheric water content from satellite microwave radiometry, *Mon. Weather Rev.*, **111**, 1977-1987, 1983.
- Phoebus, P., and J. Hawkins, The use of SSM/I water vapor data to correct altimeter sea surface height measurements (abstract), *Eos Trans. AGU*, **69**, 1281, 1988.
- Roden, G., On long wave disturbances of dynamic height in the North Pacific, *J. Phys. Oceanogr.*, **7**, 41-49, 1977.
- Roden, G., and A. Robinson, Subarctic frontal zone in the north-eastern Pacific: Mesoscale structure and synoptic description, *Rep. in Meteorol. and Oceanogr.*, **31**, 71 pp., Div. of Appl. Sci., Harvard Univ., Cambridge, Mass., 1988.
- Saastamoinen, J., Atmospheric correction for troposphere and stratosphere in radio ranging of satellites, in *The Use of Artificial Satellites for Geodesy, Geophys. Monogr. Ser.*, vol. 15, edited by S. W. Henriksen, A. Mancini, and B. H. Chovitz, pp. 247-251, AGU, Washington, D. C., 1972.
- Sailor, R., and A. LeSchack, Preliminary determination of the Geosat radar altimeter noise spectrum, *Johns Hopkins APL Tech. Dig.*, **8**(2), 182-183, 1987.
- Short, D., and C. Prabhakara, Satellite derived atmosphere water vapor as a tracer of large scale interactions between the atmosphere and ocean, in *Proceedings Satellite Remote Sensing and Applications Conference*, pp. 143-148, American Meteorological Society, Boston, Mass., 1984.
- Staelin, D., K. Kunzi, R. Pettyjohn, R. Poon, R. Wilcox, and J. Waters, Remote sensing of atmospheric water vapor and liquid water with the Nimbus 5 microwave spectrometer, *J. Appl. Meteor.*, **15**, 1204-1214, 1976.
- Tapley, B., J. Lundberg, and G. Born, The Seasat altimeter wet tropospheric range correction, *J. Geophys. Res.*, **87**, 3213-3220, 1982.
- Tapley, B., J. Lundberg, and G. Born, The Seasat altimeter wet tropospheric range correction revisited, *Mar. Geod.*, **8**, 221-248, 1984.
- Taylor, P., K. Katsaros, and R. Lipes, Determinations by Seasat of atmospheric water and synoptic fronts, *Nature*, **294**, 737-739, 1981.
- Thompson, J., G. Born, and G. Maul, Collinear-track altimetry in the Gulf of Mexico from Seasat: Measurements, models, and surface truth, *J. Geophys. Res.*, **88**, 1625-1636, 1983.
- J. D. Hawkins, Naval Oceanographic and Atmospheric Research Laboratory, Ocean Sensing and Prediction Division, Stennis Space Center, MS 39529.
- P. A. Phoebus, Naval Oceanographic and Atmospheric Research Laboratory, Atmospheric Directorate, Monterey, CA 93943.

(Received May 31, 1989;
accepted July 28, 1989)

GEOSAT Altimeter Sea-Ice Mapping

JEFFREY D. HAWKINS AND MATTHEW LYBANON

Reprinted from
IEEE JOURNAL OF OCEANIC ENGINEERING
Vol. 14, No. 2, April 1989

GEOSAT Altimeter Sea-Ice Mapping

JEFFREY D. HAWKINS AND MATTHEW LYBANON

(Invited Paper)

Abstract—Polar sea-ice measurements are reduced to a fraction of those required for accurate sea-ice analyses and forecasts by the harsh environment (intense cold, clouds, remoteness) encountered. This severe operational data void is now being partially filled by the U.S. Navy GEODetic SATellite (GEOSAT) active microwave altimeter.

The 12 March 1985 GEOSAT launch enabled satellite oceanographers to continue the earlier sea-ice monitoring shown to be feasible with the GEOS-3 and SEASAT altimeters [1]. The large difference in return signals from a 13.5 GHz pulse over water versus over sea-ice permits the generation of an ice index that responds abruptly to sea-ice edges.

Sample Arctic and Antarctic operational sea-ice index plots are shown, depicting the current effort within the Remote Sensing Branch at the Naval Ocean Research and Development Activity (NORDA). This NORDA program provides graphical ice-index displays along GEOSAT nadir tracks to the Navy/National Oceanic and Atmospheric Administration (NOAA) Joint Ice Center (JIC) for assimilation into their sea-ice data bases. The altimeter's all-weather capability has been an important addition to the JIC data bases, since cloud cover can drastically curtail visible and infrared viewing, and passive microwave data has coarser resolution.

Ongoing research efforts are aimed at extracting additional sea-ice parameters from the altimeter waveform data, which contain information on the reflecting surface. Possibilities include discrimination between water, land, ice, combination water/ice, and water/land, as well as distinguishing various ice concentrations and possibly ice types. Coincident airborne passive microwave and synthetic aperture radar (SAR) data have been collected to test several methods which appear to be promising.

Keywords—sea ice, satellite altimetry, remote sensing, GEOSAT.

I. INTRODUCTION

THE TASK encompassed in accurately mapping sea-ice characteristics has always suffered from a critical lack of observational data. The polar regions are severely undersampled by planes on routine patrol. Those patrols are supplemented only by a few point source reports from ships and drifting buoys. Thus, overcoming the data base shortage is obviously a satellite remote-sensing problem since large domains can be affordably scanned at reasonable spatial and temporal resolutions.

Satellite visible and infrared (IR) imagery have been hand-analyzed for years by operational ice analysts. Excellent results are possible in cloud-free scenes, but such conditions do not normally persist for the desired time frame. Wintertime and spring Arctic imagery can provide excellent viewing opportunities in many regions, but summertime photos are

typically quite poor because cloudiness increases markedly and therefore dramatically limits cloud-free zones within images.

Passive microwave data have been used to partially alleviate this cloud problem, with more success noted for ice-concentration values. However, the coarse resolution (50 km with Nimbus-7 data), trouble with ice-type classification and retrievals during melt and freeze periods, and problems with atmospheric storm contamination have left holes in the sea-ice data base. All three areas of difficulty are under review with the newer Special Sensor Microwave/Imager (SSM/I) data.

It has been demonstrated that active microwave radar altimeter data from SEASAT and GEOS-3 can be used to retrieve sea-ice characteristics and thus partially fill data bases. Dwyer and Godin [1] obtained good results by taking advantage of the huge signal change that occurs when the altimeter's field of view traverses from open water to sea ice (i.e., ice edge). Validation efforts in the Bering Sea went quite well but did not extend to other areas and seasons because of the spotty nature of the GEOS-3 data and the premature failure of SEASAT.

The Navy recognized this verification shortfall when they identified a secondary mission for the U.S. Navy GEODetic SATellite (GEOSAT) program centering on the altimeter's oceanographic measuring capabilities. This paper will detail the efforts to use GEOSAT data to refine an ice index that is applicable to widely varying ice conditions. The following sections will detail more fully the sea-ice mapping requirements, the present Navy ice-index operational utilization, and ongoing and future work that promises to provide additional sea-ice measurement capabilities.

II. JOINT ICE CENTER

The Joint Ice Center (JIC) at Suitland, Maryland, is a combined Navy and National Oceanic and Atmospheric Administration (NOAA) effort begun in 1976. Its duties are to map the ice edge, concentration, and type throughout both the Arctic and Antarctic Oceans as well as the Great Lakes, and to provide advance sea-ice forecasts. This joint effort permits both civilian and military agencies to plan for safer operations within this environmentally hostile region and combine severely limited resources.

The Naval Polar Oceanography Center (NPOC) represents the Navy's portion within this cooperative team. NPOC is responsible for satisfying the operational Department of Defense (DoD) polar sea-ice analysis and forecasting needs [2]. This function must be done by combining a variety of data sources in order to generate a host of products.

Fig. 1 is just one example of the many JIC Arctic sea-ice

Manuscript received May 1, 1988; revised September 20, 1988. This work was supported by the Satellite Applications and Technology (SAT) Program of the NORDA Remote Sensing Branch's Applications Development Section by Chief of Naval Operations, CNO-OP-96, under Program Element 63708N. This is NORDA contribution no. 321.061.88.

The authors are with the Remote Sensing Branch, Naval Ocean Research and Development Activity, Stennis Space Center, MS 39529-5004.

IEEE Log Number 8825748.

products. The ice edge in the eastern Arctic is delineated throughout the area, and ice concentration and type are noted using the International Egg Code nomenclature [3]. Note that dashed lines represent estimates due to lack of reliable data. This chart covers half the Arctic basin and is updated once per week.

To map sea ice over such vast, remote regions, the JIC relies heavily on polar-orbiting environmental satellites because of their large spatial swaths and frequent repeat-times each day. However, each data platform/sensor has a number of advantages and disadvantages which either enhance or limit its contributions to the total sea-ice data base. Table I outlines the major sea-ice data sources available to the ice analysts and illustrates the major factors associated with each one.

Visible and IR imagery from the NOAA Advanced Very High Resolution Radiometer (AVHRR) and Defense Meteorological Satellite Program (DMSP) Operational Line Scanner (OLS) have long been the cornerstones of the JIC data bases. The continuous effort to keep these families of satellites operationally available (i.e., NOAA-5, -6, -7, -8, -9, -10, -11, and DMSP F-5, -6, -7, -8, -9) has provided the long-term access required to satisfy many ice mapping needs. Both the AVHRR and OLS offer very good spatial resolution and excellent swath coverage, but these benefits have been limited because all imagery is analyzed in hardcopy (not digital) form. This limitation will be rectified when the JIC receives its digital ice forecast and analysis system (DIFAS) in January, 1989.

Hardcopy imagery, used extensively by trained ice analysts to detect sea-ice conditions throughout the polar regions, provides excellent data when the images are cloud-free. However, persistent cloud cover can rapidly render this data type useless over varying periods and thus negate the fine resolution. It should be noted that many instances occur when the open-water areas near the ice edge are obscured by clouds while the sea ice itself is cloud-free and readily viewed.

Passive microwave satellite data (Table I) have been used for many years to penetrate cloudy atmospheric conditions and permit "all-weather" sensing of polar sea ice. The Nimbus Electrically Scanning Microwave Radiometer (ESMR) and Scanning Multichannel Microwave Radiometer (SMMR) have for many years significantly enhanced the JIC sea-ice mapping capabilities, but their poor spatial resolution has been a persistent problem [4], [5]. The problem is especially severe for ice edge, polynya, and near-shore sea-ice mapping where resolution is critical.

Problems with the geophysical algorithms applied to the passive microwave data have also prevented ESMR and SMMR data from realizing their potential. Heavy rain and winds have earlier contaminated sea-ice retrievals, but vigorous efforts using multiple channels indicate that significant progress has been made. While ice concentration algorithms have done quite well, efforts to discriminate between first-year and multi-year ice have met with only partial success [6]. These limitations will be improved upon greatly when the SSM/I uses validated operational algorithms.

A variety of other data sources such as drifting buoys, airborne reconnaissance with ice observers and sensors, ships,

and data from other countries round out the available information used to generate sea-ice maps. However, even after incorporating all these data sources, gaps still remain in our ability to map present conditions (nowcasts), thus affecting the initial conditions for forecasts via numerical models.

III. GEOSAT OCEAN APPLICATIONS PROGRAM

GEOSAT's primary mission was to provide the dense global grid of altimeter data required to improve the determining of the earth's gravitational field. However, the Oceanographer of the Navy also formulated the GEOSAT Ocean Applications Program (GOAP), whose goal was to conduct an operational demonstration of the altimeter's usefulness to gather all-weather ocean environmental data. For over two years NORDA's Remote Sensing Branch has analyzed this data for GOAP [7].

Data collected by the altimeter are received by the only ground station, at the Johns Hopkins Applied Physics Laboratory (APL), and are processed into NORDA Data Records (NDR's). The NDR's, which contain sensor-corrected altimeter data, corrections for satellite and instrument errors, and orbit information, are transmitted promptly to NORDA over a 9600-baud, dedicated telecommunications circuit.

NORDA then processes this data to provide information on mesoscale ocean features, surface wind speed, significant wave height, and sea-ice edge. Arctic and Antarctic products based on the sea-ice edge are provided daily to NPOC. The altimeter's all-weather capability has helped to make these products useful, especially since cloud cover frequently renders other sensors useless.

IV. GEOSAT ALTIMETER

The U.S. Navy GEOSAT was built by the APL and launched on March 12, 1985. The satellite carries a single instrument, a 13.5-GHz nadir-looking pulse compression radar altimeter. It is similar to the SEASAT altimeter in its mechanical, thermal, and electrical interfaces, but includes some engineering changes intended to extend its lifetime and reduce its noise level [8]. The reflected pulses provide three basic types of information: the satellite altitude above the surface, the significant wave height, and the wind speed along the satellite track (the last two refer to returns from open water).

Fig. 2 illustrates the illumination of the surface for the case in which the surface relief is small compared to the transmitted pulse width. This figure shows the surface area illuminated at time increments equal to the duration of the transmitted pulse width and illustrates how the reflected signal received by the altimeter changes with time for the case of diffuse scattering, as from the sea surface. The mean received power, which increases linearly with time to a plateau, eventually falls off because of the finite antenna beam width and off-nadir scattering. (Increasing the surface relief, as in the case of higher waves in open ocean, increases the rise time and decreases the slope of the leading edge of the return pulse.)

The return pulses from sea ice have a significantly different shape than returns from the ocean [9], [10]. Fig. 3 illustrates that difference. Ice, unlike water, tends to produce specular reflection so that a much larger portion of the impinging

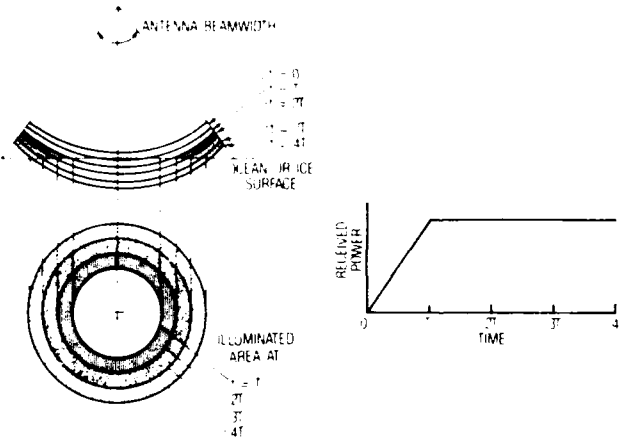


Fig. 2 Illumination of the earth's surface by an altimeter pulse of width T .

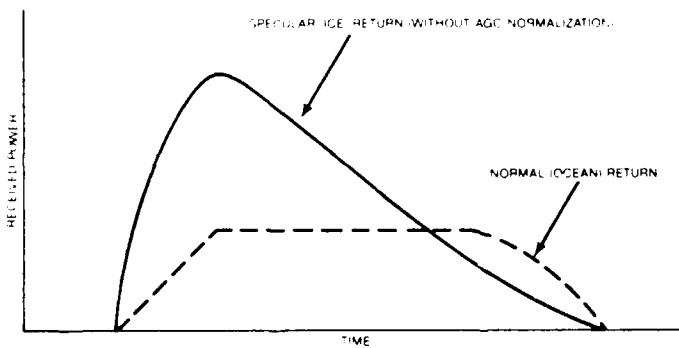


Fig. 3 Ice and ocean altimeter return waveforms.

energy at any angle will reflect off the ice surface at an angle equal to the angle of incidence. Thus the early return (that received from nadir) is much stronger than the latter part of the return (that received at angles off-nadir). So both the signal strength and the shape of the reflected pulse are modified. Dwyer and Godin [1] developed a semiempirical algorithm for the GEOS-3 altimeter that measures strength and shape differences. The algorithm is

$$\text{Index} = [(100 + AGC)/(100 \times AASG)] - 10 \quad (1)$$

where AGC = automatic gain control signal, and $AASG$ = average attitude/specular gate signal [1].

The Dwyer-Godin algorithm as modified for GEOSAT is

$$\text{Index} = [(100 + AGC)/(100 \times VATT)] \quad (2)$$

where

$$VATT = [(ATTG - ATTGE)/(AGCG - ATTGE)] \quad (3)$$

and the intermediate quantities are functions of the 60 basic waveform samples (the sample indexing is the same as for the SEASAT altimeter [11]): $ATTG$ = mean of last eight samples, $ATTGE$ = mean of first eight samples, and $AGCG$ = mean of center 48 samples (not including the track point gate).

$VATT$ is known as "voltage proportional to attitude" and is used in corrections for off nadir pointing errors in the computation of several ocean parameters. The GEOSAT ice index is a number in the range 0.6 to 0.7 over water, and over

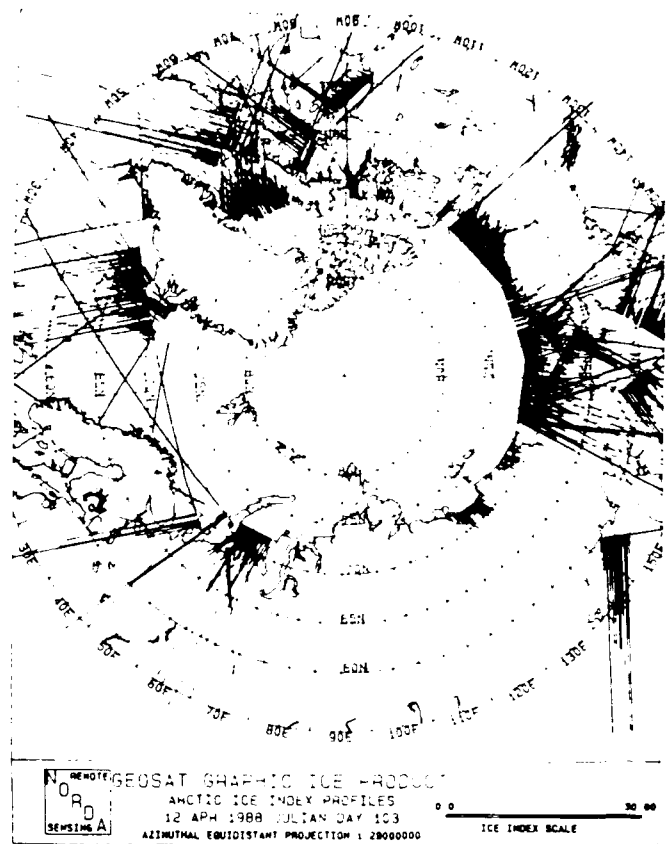


Fig. 4. Sample GEOSAT ice-index graphic product for the Arctic. Ice indexes are plotted perpendicularly to the track according to the scale in the lower-right corner. All index values < 1 have been suppressed.

ice is greater than 1. Thus, water-ice transitions are evident in the time history of the ice index.

The GEOSAT altimeter provides dense, all-weather measurements along the satellite's nadir track, but the "swath" width is only a few kilometers. The inclination of the satellite's orbit limits coverage to between 72° N and S latitudes. Within these limits, however, GEOSAT is able to provide a valuable data source that significantly increases the available sea-ice information. Ice-index values are plotted on charts made to the same scale and projection as NPOC's master working charts. These plots show ice-index profiles over water, with the satellite's nadir tracks as base lines. Figs. 4 and 5 are sample ice-index plots for the Arctic and Antarctic regions.

V. GEOSAT COVERAGE

GEOSAT was initially injected into an 800-km altitude, 108° inclination orbit that generated a three-day near-repeat ground track. During October, 1986, the satellite was moved into an exact repeat mission (ERM) orbit that was slightly adjusted to repeat exactly every 244 revolutions (17.05 days).

Figs. 6 and 7 depict a typical track "laydown" for one day during the ERM, which is scheduled to continue until 1991 or 1992. The Navy has funded ground operations in anticipation of a "healthy" sensor and data during this time frame. Extended operation into the 1990's would enable it to overlap with the next environmental satellite carrying an altimeter, the European Space Agency (ESA) Remote Sensing Satellite (ERS-1).

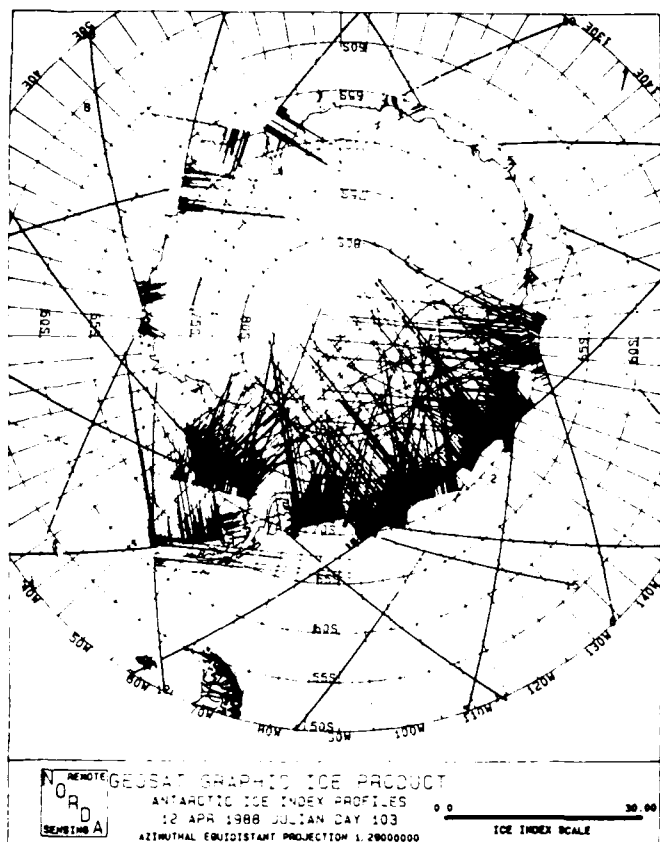


Fig. 5 Sample GEOSAT ice-index graphic product for the Antarctic.

The track plots readily reveal several pluses and minuses for GEOSAT sea-ice mapping. Immediately apparent is the data void poleward of 72° latitude. The realization that the swath is the same size as the sensor footprint (2–4 km) also suggests many problems associated with temporal and spatial sampling deficiencies. It is thus clear that one single-beam altimeter is severely limited and can be counted on only to fill in data gaps.

The Navy is thus using GEOSAT data as an additional all-weather information source. Each major Arctic basin (e.g., East Greenland, Barents, Beaufort, Chukchi, Bering Sea, etc.) is sampled 3 to 4 times daily. Sampling increases dramatically near 72° as the tracks converge. This enables long passes through ice-infested waters and potentially produces numerous sea-ice data points, especially for those areas where ice motion is small and the ice analyst can use more than one day as input. Fig. 8 is a three-day Arctic track plot which shows that a wealth of data can be gathered between 65° N and 72° N as the tracks bend westward. Sea-ice mapping via GEOSAT data is thus enhanced within this section of the world.

Fig. 7 readily exhibits a different picture for Antarctic sampling. Land masses extend toward the equator from 72° S for slightly more than 50 percent of the area enclosed by this latitude band (60° S to 72° S). Such coverage, combined with the fact that the ice edge in the remaining open-water basins (Weddell and Ross Seas) is often within GEOSAT range, makes Antarctic sea-ice mapping via GEOSAT more feasible than in the Arctic. This situation is welcome, since less AVHRR data is available in the Antarctic because direct readout stations are not presently sending data to the JIC

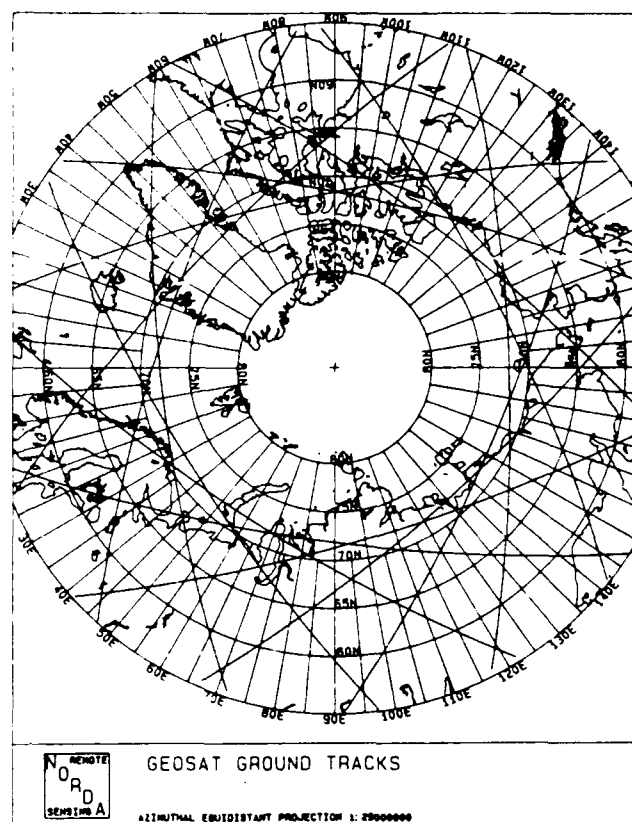


Fig. 6. One day of GEOSAT ERM ground tracks in the Arctic.

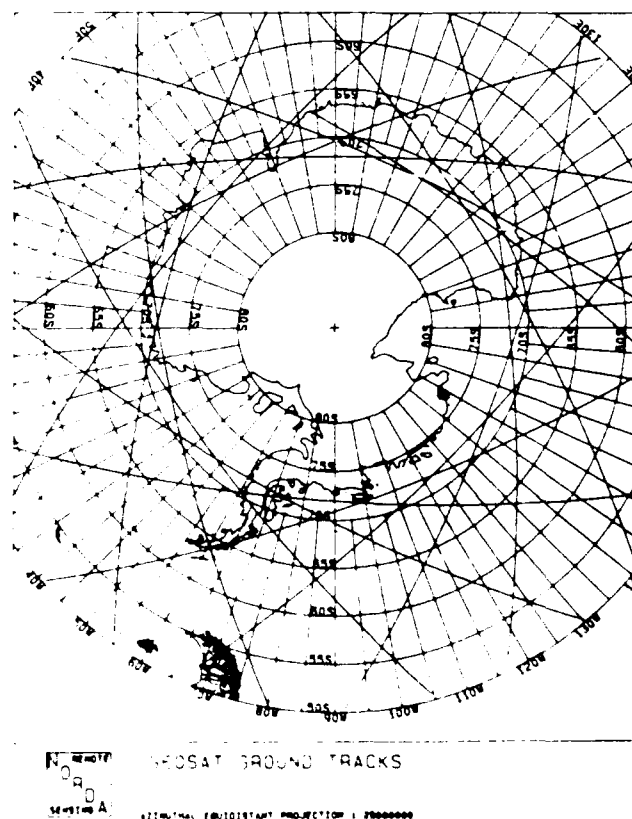


Fig. 7 One day of GEOSAT ERM ground tracks in the Antarctic.

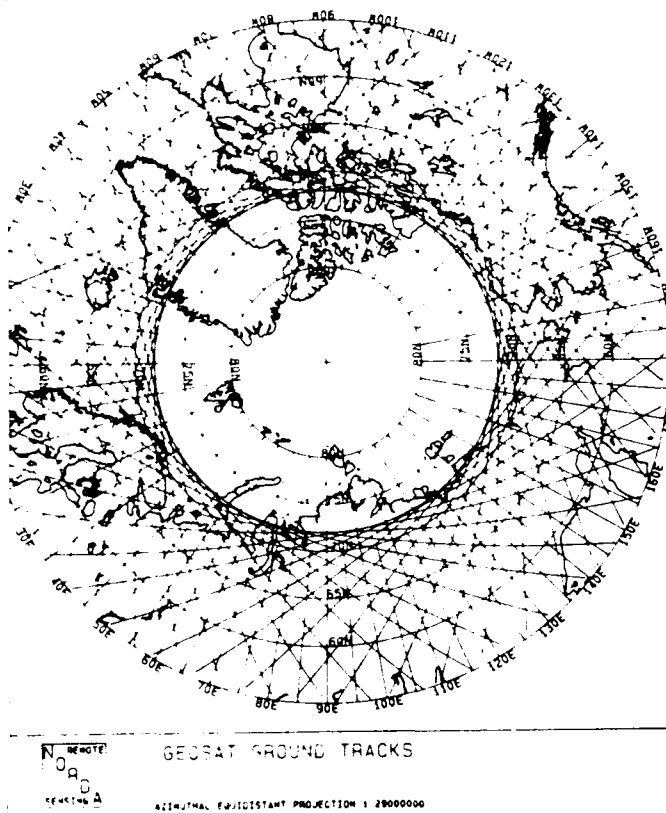


Fig. 8. Three days of GEOSAT ERM ground tracks in the Arctic.

VI. VALIDATION

Mapping sea-ice parameters is difficult to begin with, so verifying them is an extremely arduous task at best. NORDA has enlisted a variety of spaceborne and airborne sensors to determine if GEOSAT-determined ice edges are reasonable. The verification data was obtained by using a combination of AVHRR and airborne passive and active microwave sensors.

NORDA chose NOAA AVHRR data as the prime verification tool because it has the following characteristics: A large swath, frequent repeat times and thus good temporal matchups, 1-km spatial resolution, and multispectral imaging. The majority of comparisons with GEOSAT data involved 1-km visible data in the East Greenland Sea. A more limited data set was collected in the Kara Sea and the Antarctic using 1-km IR data.

The marginal ice zone (MIZ) within the East Greenland Sea takes on a host of shapes and perturbations dependent on the combined wind and current conditions. Very accurate ice-edge boundaries can be defined when wind flow is toward the ice ("on ice"). The MIZ becomes very compact as many loose pieces and floes converge toward a new and well-defined line of demarcation between open water and sea ice. These conditions have been used as much as possible in this study in order to increase the accuracy of AVHRR ice-edge locations.

Sharp ice edges along the MIZ and the fact that numerous GEOSAT tracks cross the Greenland coast between 60° N and 72° N permit the generation of 3 to 4 ice-edge points per day, provided that the cloud conditions are favorable. Generally, in March, April, and May cloud-free viewing is at a maximum and numerous images covering large ice-edge segments are

available for acquisition by NORDA's Satellite Digital Receiving and Processing System (SDRPS). SDRPS can access both Local Area Coverage (LAC—1 km) and Global Area Coverage (GAC—4 km) data.

Fig. 9 represents a typical example of the advantages and disadvantages inherent in the original NORDA GEOSAT sea-ice index. The May 10, 1987, image (AVHRR channel 2, surface reflectance) has been subsampled by two to show the ice edge from 67° N to 72° N. The resultant 2-km resolution image (512 × 512 pixels or about 1000 km on a side) contains a well-delineated MIZ extending along all but the extreme southern sections where clouds obscure the coast and the waters south and west of Iceland.

The image has been calibrated and earth located to 1-pixel accuracy using NORDA's Interactive Digital Satellite Image Processing System (IDSIPS). This set of hardware/software is based on a VAX 8300 computer and an International Imaging System (I²S) display. The polar stereographic projection is labeled with 1° latitude and 5° longitude grid lines, while the land mask is inlaid within a graphics plane. The image has been contrast-stretched to bring out the sea-ice features, while ignoring the thin clouds in the west.

Three ascending and two descending GEOSAT tracks pass over sea ice on May 10, 1987. All ascending tracks intersect the ice edge in a near-perpendicular transect with only the southern one appearing to miss flagging the ice edge correctly, as seen by matching the AVHRR edge location with the first spike in ice-index values. Both descending tracks do quite well on the ice edge, but nonetheless illustrate a frequent problem involving data gaps (i.e., large sections have index values less than 1 or are missing for some reason).

The northernmost track readily exhibits numerous data gaps consisting of 2 to 5 data points. The absence of ice-index values causes the ice analyst confusion—should the data holes be interpreted as open-water segments or simply bad data? A similar situation is also depicted in the descending pass that grazes the MIZ and hits sea ice four separate times. The initial ice edge is marked well in some cases, but poorly in others.

NORDA undertook an effort to explain the data gaps by first looking at the parameters used to compute the ice index, AGC and VATT. These values were plotted along several tracks and quickly exposed a major problem. VATT numbers were often negative, thus causing the ice-index value to be set to zero via a data quality check. Further study revealed that the VATT value being used was not the one directly based on features of the altimeter return waveform (3). The VATT parameter has been adjusted so that tables previously prepared for use in the calculation of off-nadir angle corrections to ocean (water) parameters, based on preflight calibration, could be used without modification. The adjustment was a linear transformation: Multiplication by one constant and the addition of another. This adjustment resulted in the frequent production of negative VATT values for return pulses from ice.

NORDA (with the help of S. Laxon) proceeded to recompute the original VATT values and insert them into the sea-ice index formula (2). The results are dramatically evident in Fig. 10. All the data gaps have been eliminated and two very important facts are clear:

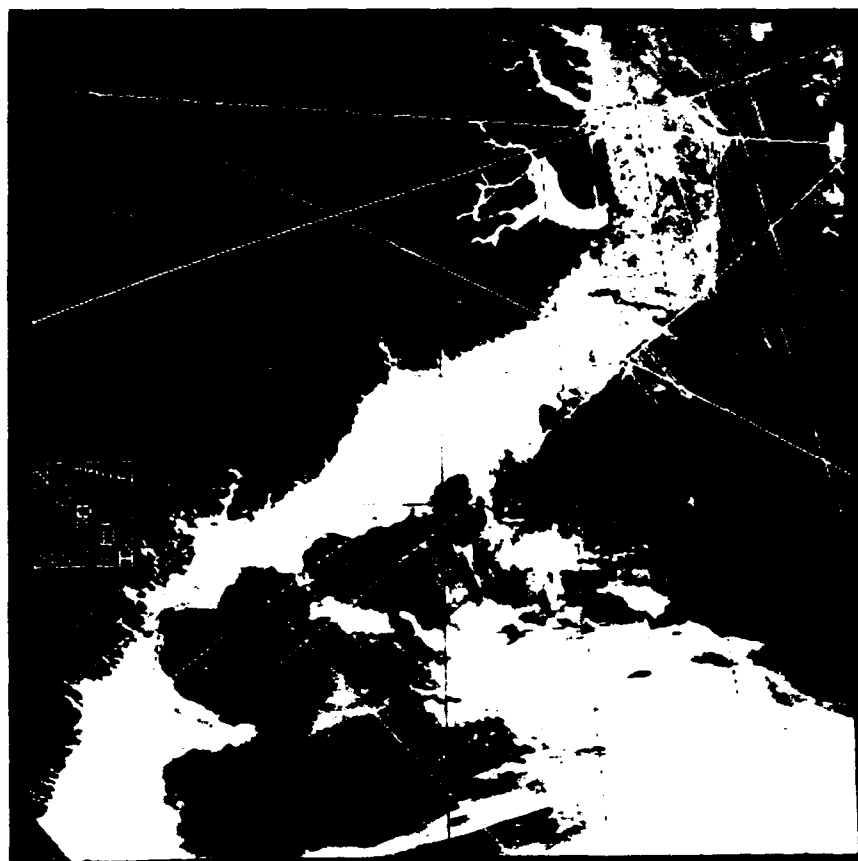


Fig. 9. AVHRR channel 2 (surface reflectance) May 10, 1987, East Greenland Sea image with the original GEOSAT ice-index superimposed. Image enhanced for sea ice.

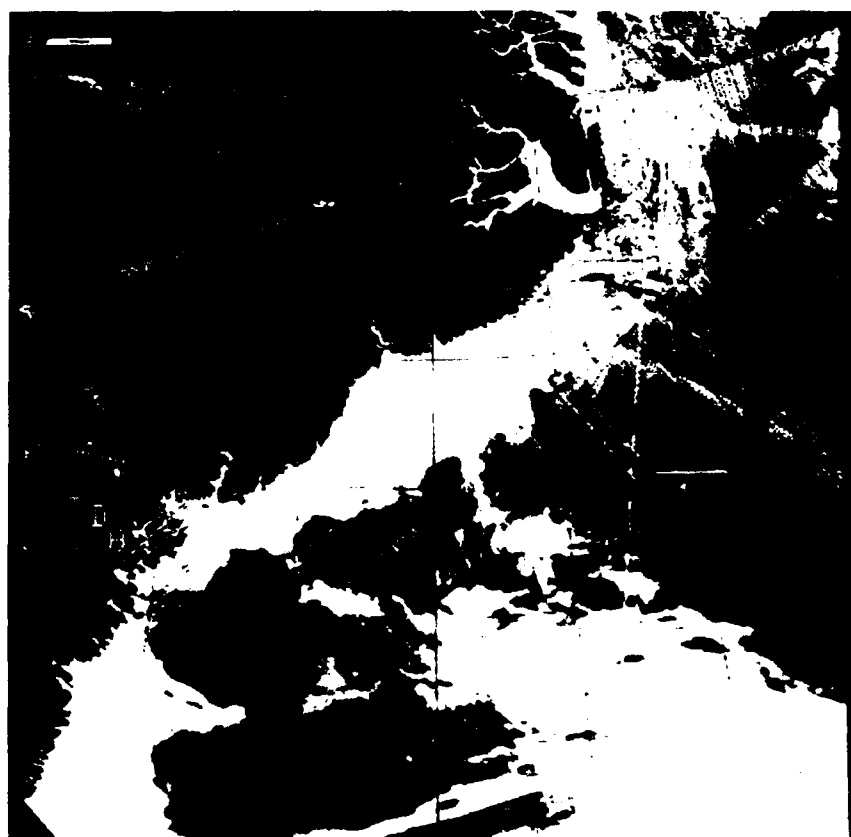


Fig. 10. AVHRR channel 2 (surface reflectance) May 10, 1987, East Greenland Sea image with revised ice-index superimposed. Image enhanced for sea ice.

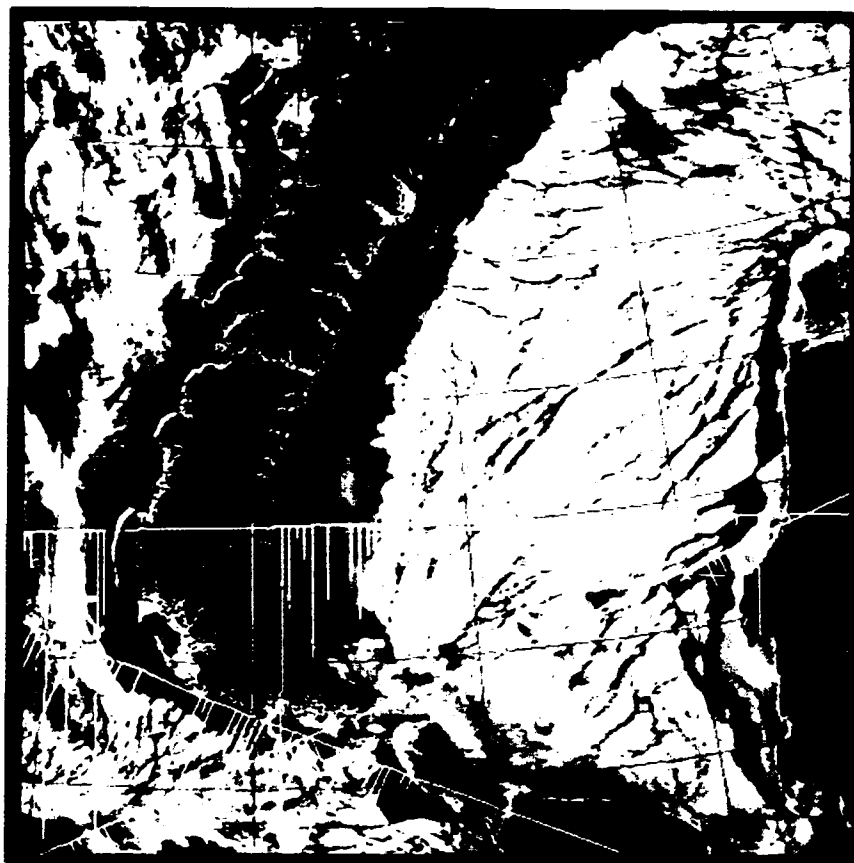


Fig. 11. AVHRR channel 4 (IR) February 21, 1986, Kara Sea image with original GEOSAT ice-index superimposed. Image enhanced to bring out sea-ice detail.

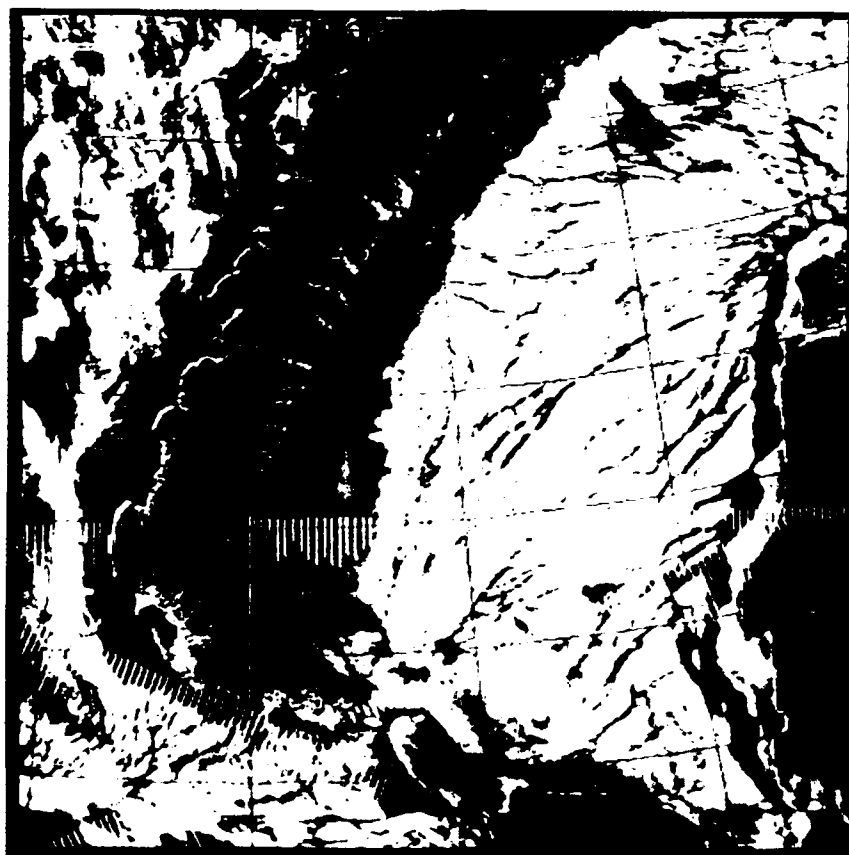


Fig. 12. AVHRR channel 4 (IR) February 21, 1986, Kara Sea image with revised ice-index superimposed. Image enhanced to bring out sea-ice detail.

1) The location of ice-edge positions has been enhanced, as is evident in the much better agreement that now exists for the southernmost track as well as the MIZ transect. The four discrete zones or perturbations eastward of the track are very accurately detected with the new sea-ice index.

2) The removal of data gaps now permits the analyst to map ice *within* the ice edge, whereas data gaps previously limited the interpretation to the edge only.

It is also quite interesting to note the high variability associated with the index values as the sensor traverses from open water, through the MIZ, into the pack ice, and then up onto the fast ice near shore. Thus, the question is whether the ice index is sensitive to ice concentration or some form of ice type manifested in characteristics such as roughness. Subsequent examples will begin to clarify this idea.

We therefore present the data collected on February 21, 1986, in the Kara Sea. Fig. 11 is a full 1-km resolution (512×512) infrared (AVHRR channel 4) image with three superimposed GEOSAT tracks and the accompanying original NORDA sea-ice index. The data gap problem is once again prominent and strictly limits ice-index utilization for this area. However, several other ice-index features are seen for the first time. The Kara Sea is characterized by the presence of two basic ice types. Rough first-year ice covers the largest area and is identified by the bright white (cold) IR signature with numerous leads running among it. Smooth, dark (warm), very young, thin ice is evident in the refrozen polynya to the west and in the refrozen lead located on the far right. These IR-defined ice types are reflected in the original ice index by large, highly variable values over the new ice and much smaller homogeneous values over the high-concentration first-year ice.

Fig. 12 reveals the changes made when the updated ice index is calculated. The data gap problem has been eliminated once again, but the index variability, so readily seen in the revised East Greenland Sea image (Fig. 10) and in the original Kara Sea image (Fig. 11), has been reduced considerably. There is still a factor-of-two increase in index values over the young, thin ice, with some spikes in the refrozen lead, but we have lost much of the sensitivity apparent earlier.

NORDA is presently looking into several means to optimize the combination of AGC and VATT for production of a general purpose (i.e., all regions and seasons) ice index that can be used to detect ice edges and ice types. This goal may not be feasible and an increased regional emphasis may have to be adopted.

VII. FUTURE WORK

Several opportunities exist to help answer some of the questions raised here. NORDA will continue to acquire AVHRR data periodically in both polar regions for direct comparisons with the GEOSAT sea-ice index. Extensive data sets in the Chukchi and Beaufort Seas have been collected and are nearing process completion. NORDA has also collected nine tracks of K-Band Radiometric Mapping System (KRMS, 33-GHz passive microwave) data in March, 1987, within the East Greenland Sea. This scanner underflew 3 to 4 GEOSAT tracks per day as outlined in Fig. 1. The KRMS swath allows

the sensor to straddle the GEOSAT footprint (15 km at 20 000 ft, 7.5 km at 10 000 ft) while still providing very good spatial resolution [12], [13]. This data is now being processed to provide a highly accurate breakdown of ice concentration by ice type within the GEOSAT footprint.

Airborne Synthetic Aperture Radar (SAR) data from the Interra STAR 2 System [14] was also collected for five GEOSAT underflights during April, 1987, at the end of MIZEX-87 [15]. This joint effort with two NORDA programs, the ERS-1 Advanced Sensor Analysis Program and the Satellite Applications and Technology Program, acquired excellent quality high-resolution digital SAR imagery along the altimeter tracks. These transects sampled a variety of ice types and will help greatly in delineating the full potential of the sea-ice index.

Another approach that NORDA deems promising is the application of linear unmixing theory to the extraction of ice types and concentrations from altimeter waveform data. Unmixing theory has been applied for many years to a variety of geology problems [16]. Recent work in unmixing theory [17] has extended these analysis techniques into new areas such as waveform analysis. Application of this method, which treats waveforms as multivariate data vectors formed by variable combinations of pure "end members," is underway for several cases where coincident SAR, photography, passive microwave imagery, or ground truth is available. These data sets should permit a thorough evaluation of the unmixing approach to waveform analysis.

It appears likely that additional sea-ice information can be derived from the waveform data or possibly the ice index itself. Analysis of the coincident airborne data base will be the first step NORDA takes in investigating the potential expansion in applications. This field of study holds promise in increasing our utilization of the limited space platforms now in orbit or soon to be launched (ERS-1 and TOPEX will carry microwave altimeters). Cooperative efforts are encouraged, since polar data collection programs are prohibitively expensive. In this framework, NORDA is actively planning participation in ground truth and algorithm research programs for these environmental platforms.

ACKNOWLEDGMENT

The authors are glad to acknowledge the many contributions that made this effort possible. S. Laxon of the Mullard Space Science Laboratory (MSSL, part of University College, London) efficiently performed the work that greatly improved the GEOSAT ice-index calculation. This progress has opened up new applications. D. Eppler and D. Johnson of NORDA have provided valuable consultation during various research stages and are directly involved in ongoing and future efforts to extract additional sea-ice characteristics from altimetry. C. Johnson (NORDA) has consistently produced superior programming efforts which enabled operational status in spite of a variety of significant problems. Sverdrup Technology employees N. Koenen and Y. Crook generated ice-index overlays, and F. Abell, Jr., processed the AVHRR imagery. T. Bogart, J. Chase, and W. Owens (Sverdrup) produced the ice-index software, while P. Phoebus (NORDA) and several reviewers

considerably helped to refine the original manuscript draft. The compilation of this paper was done by the NORDA Remote Sensing Branch's Applications Development Section and was directly supported under the Satellite Applications and Technology (SAT) Program. A. E. Pressman, Program Manager.

REFERENCES

- [1] R. W. Dwyer and R. H. Godin, "Determining sea ice boundaries and ice roughness using GEOS-3 altimeter data," NASA Contractor Rep. 156862, 1980.
- [2] H. Rosner, "The NPOC capabilities and limitations in sea ice analysis and forecasting," presented at the U.S. Navy Symp. on Arctic Cold Weather Operational Support for Surface Ships, Naval Surface Weapons Ctr., Dahlgren, VA, Nov. 20, 1987.
- [3] WMO Commission for Marine Meteorology, 4th session, working group on sea ice (Geneva), Final Rep. Oct. 25-29, 1982.
- [4] D. T. Eppler, "Assessment of potential SSM/I ice products in light of ESMR and SMMR ice classification algorithms," Naval Ocean Research and Development Activity, NSTL, MS, Tech. Note 220, 1983.
- [5] J. C. Comiso and H. J. Zwally, "Antarctic sea ice concentrations inferred from Nimbus 5 ESMR and Landsat imagery," *J. Geophys. Res.*, vol. 88, no. C8, pp. 5836-5844, 1982.
- [6] J. C. Comiso, "Characteristics of Arctic winter sea ice from satellite multispectral microwave observations," *J. Geophys. Res.*, vol. 91, no. C1, pp. 975-994, 1986.
- [7] M. Lybanon and R. L. Crout, "The NORDA GEOSAT ocean applications program," *Johns Hopkins APL Tech. Dig.*, vol. 8, pp. 212-218, Apr.-June 1987.
- [8] J. L. MacArthur, P. C. Marth, Jr., and J. G. Wall, "The GEOSAT radar altimeter," *Johns Hopkins APL Tech. Dig.*, vol. 8, pp. 176-181, Apr.-June 1987.
- [9] D. T. Eppler, "Possible applications of GEOSAT-A radar altimeter data to ice forecasting in polar regions," Naval Ocean Research and Development Activity, NSTL, MS, Tech. Note 177, 1982.
- [10] L. M. H. Ulander, "Interpretation of SEASAT radar-altimeter data over sea ice using near-simultaneous SAR imagery," *Int. J. Remote Sensing*, vol. 8, no. 11, pp. 1679-1686, 1987.
- [11] J. L. MacArthur, "SEASAT-A radar altimeter design description," The Johns Hopkins Univ., Appl. Phys. Lab., Laurel, MD, Rep. SDO-5232, 1978.
- [12] D. T. Eppler, L. D. Farmer, A. W. Lohanick, and M. C. Hoover, "Classification of sea ice types with single-band (33.6 GHz) airborne passive microwave imagery," *J. Geophys. Res.*, vol. 91, no. C9, pp. 10661-10695, 1986.
- [13] D. T. Eppler and J. D. Hawkins, "NORDA arctic data collection, processing, and interpretation capabilities," Naval Ocean Research and Development Activity, NSTL, MS, Rep. 129, 1985.
- [14] A. D. Nichols, J. W. Wilhelm, T. W. Gaffield, D. R. Inkster, and S. K. Leung, "A SAR for real-time ice reconnaissance," *IEEE Trans. Geosci. Remote Sensing*, vol. GE-24, pp. 383-389, May 1987.
- [15] D. R. Johnson and J. D. Hawkins, "The marginal ice zone experiment: MIZEX-87," *European Sci. Notes* (U.S. Office of Naval Research, London), vol. 41, no. 10, pp. 567-570, 1987.
- [16] R. Ehrlich and W. E. Full, "Sorting out geology—Unmixing mixtures," in *Use and Abuse of Statistical Methods in the Earth Sciences*, W. Size, Ed., New York: Oxford Univ. Press, 1987.
- [17] J. R. Chase and R. J. Holyer, "Estimation of sea-ice type and concentration by linear unmixing of GEOSAT altimeter waveforms," presented at IGARSS '88 (Edinburgh, Scotland), Sept. 13-16, 1988.



Jeffrey D. Hawkins received the B.S. and M.S. degrees in meteorology from the Florida State University, Tallahassee, in 1976 and 1979, respectively.

After graduation, he participated in SEASAT scatterometer validation and air-sea interaction studies near hurricanes while working for the Hurricane Research Division, AOML (Atlantic Oceanographic and Meteorological Lab, Miami, FL). In late 1980 he accepted a position as oceanographer in the Remote Sensing Branch of the Naval

Ocean Research and Development Activity (NORDA, Stennis Space Center, MS). His present duties as Head, Applications Development Section, involve a wide variety of R&D programs aimed at utilizing spaceborne environmental sensors (AVHRR, OLS, GEOSAT altimeter, SSM/I, etc.) to meet specific Navy oceanographic requirements in the areas of sea-surface temperature, sea-surface height, and sea ice.

Mr. Hawkins is a member of the American Geophysical Union, the American Meteorological Society, the Oceanography Society, and the American Society for Photogrammetry and Remote Sensing.



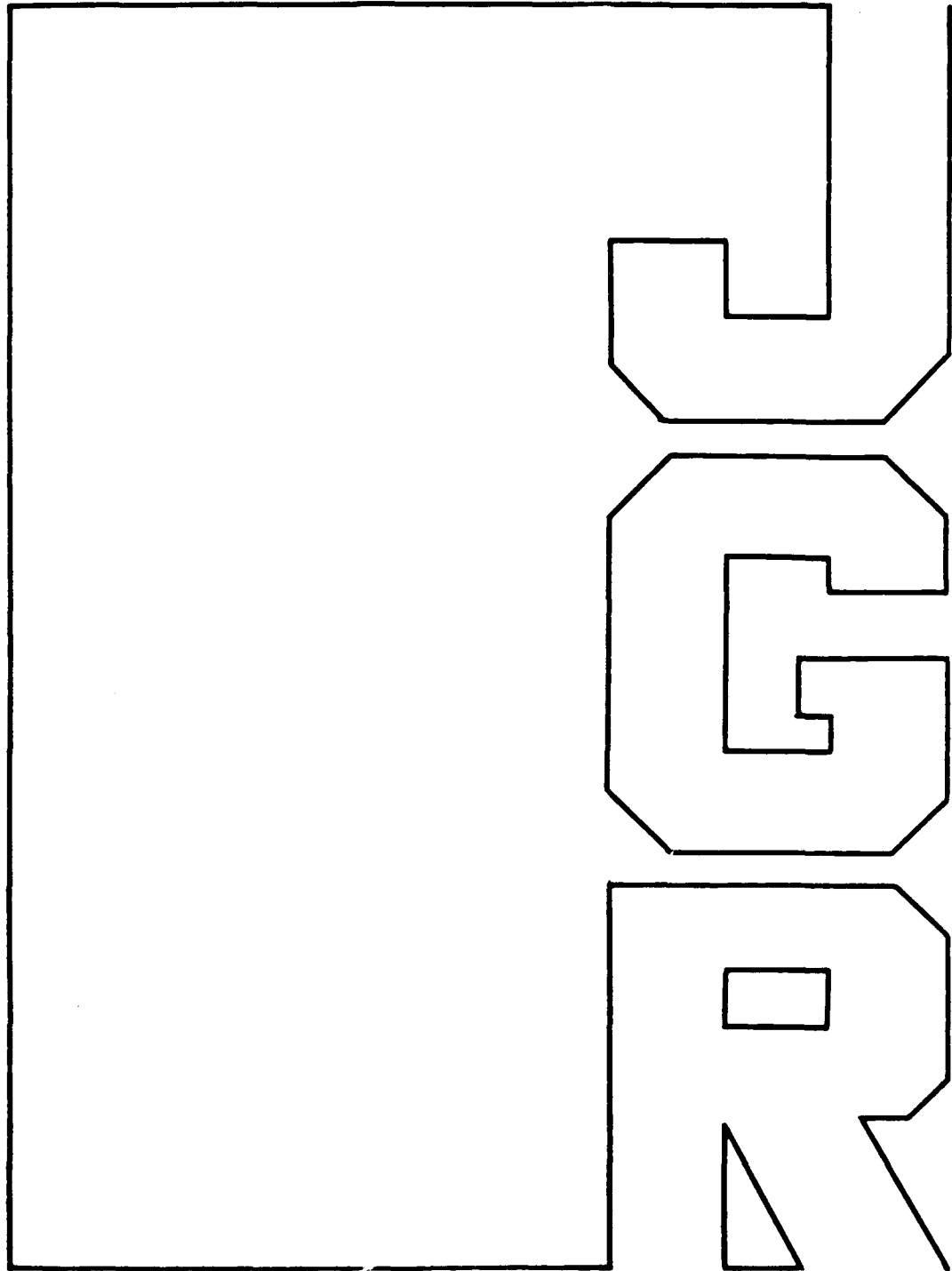
Matthew Lybanon received the B.S. and M.S. degrees in physics from the Georgia Institute of Technology, Atlanta, in 1960 and 1962, respectively.

He conducted research in remote sensing, image processing, and pattern recognition while employed by the Computer Sciences Corporation at NASA's Marshall Space Flight Center and Stennis Space Center (previously called National Space Technology Laboratories). In 1981 he joined the Naval Ocean Research and Development Activity (NORDA), Stennis Space Center, MS. A member of NORDA's Remote Sensing Branch, he has been Principal Investigator for the GEOSAT Ocean Applications Program, for a project to develop knowledge-based techniques for the automated interpretation of oceanographic satellite data, and for other work to provide analysis tools for Navy oceanographic centers. His current professional interests include artificial intelligence, image processing, generalized nonlinear least squares methods, and applications of those topics to the extraction of information on ocean dynamics and sea ice from satellite observations.

Mr. Lybanon is a member of the American Physical Society. He was awarded a NASA commendation for image-processing work to help assess the damage to Skylab's solar panels when they opened prematurely during launching.

Sampling Strategies and Model Assimilation of Altimetric Data for Ocean Monitoring and Prediction

JOHN C. KINDLE



Sampling Strategies and Model Assimilation of Altimetric Data for Ocean Monitoring and Prediction

JOHN C. KINDLE

Ocean Dynamics and Prediction Branch, Naval Ocean Research and Development Activity, NSTL, Mississippi

Numerical forecasts using simulated altimeter data are generated in order to examine the assimilation of altimeter-derived sea surface heights into numerical ocean circulation models. A one-layer reduced gravity primitive equation circulation model of the Gulf of Mexico is utilized; the Gulf of Mexico is chosen because of its amenability to modeling and the ability of low vertical mode models to reproduce many of the observed dynamical features of gulf circulation. The simulated data are obtained by flying a hypothetical altimeter over the model ocean and sampling the model sea surface in a manner similar to a real altimeter. The data are used to examine spatial sampling requirements for accurate resolution of oceanic eddies and, in forecast mode, the assimilation of asynoptic altimeter data into numerical models. Results indicate that for a stationary circular eddy, approximately two tracks (either ascending or descending) across the eddy are sufficient to ensure adequate spatial resolution. An irregularly shaped eddy may require three or four tracks. In addition, the study reveals that if the track spacing is sufficient to resolve the height field of an eddy, the along-track geostrophic velocity component is determined with equivalent accuracy to that of the cross track component. Simulated Gulf of Mexico circulation forecasts suggest that the numerical model can effectively assimilate asynoptic altimeter measurements. Optimum sampling strategies for a single beam altimeter and intermittent updating of the nowcast forecast are examined.

1. INTRODUCTION

The satellite radar altimeter offers the most promising capability of routinely providing timely global observations suitable for initializing an ocean circulation forecasting model [for example, *Hurlburt*, 1984]. Other informative reviews on the use of satellite altimetry to study the ocean circulation are provided by *Wunsch and Gaposchkin* [1980] and *Fu* [1983]. The determination of absolute geostrophic velocities adequate for ocean prediction requires the measurement of sea surface topography relative to the geoid to an accuracy of 5–10 cm (see the reviews mentioned above). Although the altimeter measurement of sea surface topography can be performed with this precision (see *Tapley et al.* [1982] for a discussion of Seasat accuracy), the publicly available geoid is too noisy to satisfy this requirement [*Zlotnicki*, 1984]. However, improved analysis techniques and satellite missions such as GRAVSAT are expected to reduce the uncertainty of the geoid to the extent that ocean monitoring and prediction using altimeter data are realistic goals [*Committee on Geodesy*, 1985; *Thompson*, this issue].

In addition to the observational accuracy requirements and an accurate knowledge of the geoid, a viable oceanic nowcast forecast will also depend on an innovative development of sampling strategies, four-dimensional data assimilation techniques, and initialization methods. The assimilation problems presented by noisy, asynoptic data and the vertical transfer of surface observations into useful subsurface information are nontrivial. For example, the difficulty of a single nadir beam altimeter to provide a truly synoptic measurement that adequately resolves the mesoscale eddy field, major current systems, and fronts poses a significant challenge to the development of skillful forecasting ability. Hence the thrust of this report is an examination of spatial and temporal sampling strategies that optimize the usefulness of asynoptic altimeter-derived sea surface heights in ocean monitoring and predic-

tion. In order to isolate the effects and problems of asynoptic data, perfect (i.e., uncontaminated by geoid, tide, or noise) simulated altimeter data will be used in conjunction with a one-layer reduced gravity numerical model. In particular, this work will attempt to determine the track spacing that resolves the detectable meandering current systems and eddies and to investigate the ability of numerical circulation prediction models to fill in the resulting temporal gaps. In related studies, *Hurlburt* [this issue] examines the dynamic transfer of synoptic altimeter data into subsurface information and *Thompson* [this issue] uses a Gulf of Mexico model with realistic basin geometry and bottom topography to assess the effects of geoid uncertainty and contaminated data on the numerical prediction.

A one-layer reduced gravity primitive equation circulation model of the Gulf of Mexico [*Hurlburt and Thompson*, 1980] is utilized to examine the methodology of incorporating asynoptic satellite altimeter data into ocean forecasting models. Simulated altimeter measurements of sea surface height are obtained by (1) integrating the model to statistical equilibrium, (2) flying a hypothetical altimeter over the model ocean, and (3) objectively mapping the perfect data onto a numerical grid. The model is initialized and restarted using the "observed" field, and the subsequent forecast (up to several months) is compared to the true solution. Additional experiments are performed in which the simulated altimeter data are periodically inserted into the numerical solution on a track by track basis. This approach permits an investigation of the maximum track spacing for mesoscale mapping, the optimum sampling period track spacing for repeat orbits, four-dimensional data assimilation methods, initialization schemes, and techniques for updating the forecast. In section 2, the numerical model and the Gulf of Mexico (GOM) simulations are described. Section 3 examines the track spacing required to resolve isolated stationary eddies and the associated geostrophic velocity field. Section 4 begins the study of incorporating asynoptic altimeter data into numerical models for the purpose of generating accurate nowcasts and forecasts. In section 5 the asynoptic assimilation studies are continued but for a more difficult GOM simulation; the model ocean is characterized by much greater temporal and spatial varia-

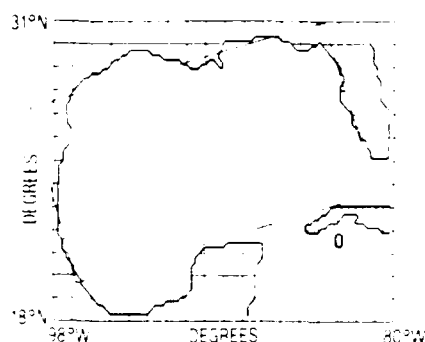


Fig. 1 Rectangular model basin superimposed on a map of the Gulf of Mexico.

bility. The assimilation experiments described herein focus on the problems of spatial resolution and asymptotic data, given accurate dynamic sea surface heights derived from a single-beam radar altimeter.

2. THE GULF OF MEXICO MODEL

The Gulf of Mexico has been chosen for this study for several reasons. As a semiencllosed sea with well-defined inflow and outflow ports, it is highly amenable to modeling. The basin is small enough to permit a relatively large number of experiments with fine resolution and is large enough to exhibit the dynamical features found in larger ocean basins. The primary forcing in the gulf is the intense Loop Current, which enters through the Yucatan Straits and exits through the Florida Straits. Approximately once per year, the Loop Current sheds an anticyclonic eddy that propagates westward. Both the Loop Current and the associated eddies have large sea surface signatures (~ 30 – 75 cm). In addition, the eddies propagate slowly (~ 3 cm/s) and have large horizontal scales (200–500 km in diameter). These attributes make the Gulf of Mexico an especially attractive region for the study of oceanic prediction during the extended GEOSAT mission with a 17-day repeat orbit.

The numerical simulations use the one-layer reduced gravity version of the *Hurlburt and Thompson* [1980] model of the Gulf of Mexico circulation. This formulation represents the ocean as two incompressible homogeneous layers; the lower layer is infinitely deep and motionless. The governing equations are

$$\frac{\partial \mathbf{V}}{\partial t} + (\mathbf{V} \cdot \nabla + \mathbf{V} \cdot \nabla) \mathbf{V} + \hat{k} \times f \mathbf{V} = -h \nabla P + \tau \rho + A \nabla^2 \mathbf{V} \quad (1)$$

TABLE 1. Model Parameters

Parameter	Value
f_0	$5 \times 10^{-5} \text{ s}^{-1}$
q	980 cm s^{-2}
h	3 cm s^{-1}
H	200 m
β	$2 \times 10^{-11} \text{ cm}^{-1} \text{ s}^{-1}$
ρ	1 g cm^{-3}
τ	0
Domain size	$1600 \times 900 \text{ km}$
Southern port width	160 km
Eastern port width	150 km
Upper layer inflow transport	$20 \times 10^6 \text{ m}^3 \text{ s}^{-1} (2 \text{ Sv})$
Angle of inflow from x axis	90°

where

$$\nabla = \frac{\partial}{\partial x} \hat{i} + \frac{\partial}{\partial y} \hat{j} \quad \tau = \tau^x \hat{i} + \tau^y \hat{j}$$

$$P = g(h - H) \quad \mathbf{V} = h\mathbf{v} = h u \hat{i} + v \hat{j}$$

$$q = q \Delta \rho / \rho \quad f = f_0 + \beta(y - y_0)$$

Figure 1 shows the model domain superimposed on a map of the Gulf of Mexico. The 20° counterclockwise rotation of the Gulf of Mexico is neglected. The model is driven from rest by prescribed inflow through the Yucatan Straits (southern port) and compensated by outflow through the Florida Straits. No wind forcing is included in the experiments discussed below. The momentum equation in the lower layer is

$$q \nabla^2 \xi = -g \nabla h \quad (2)$$

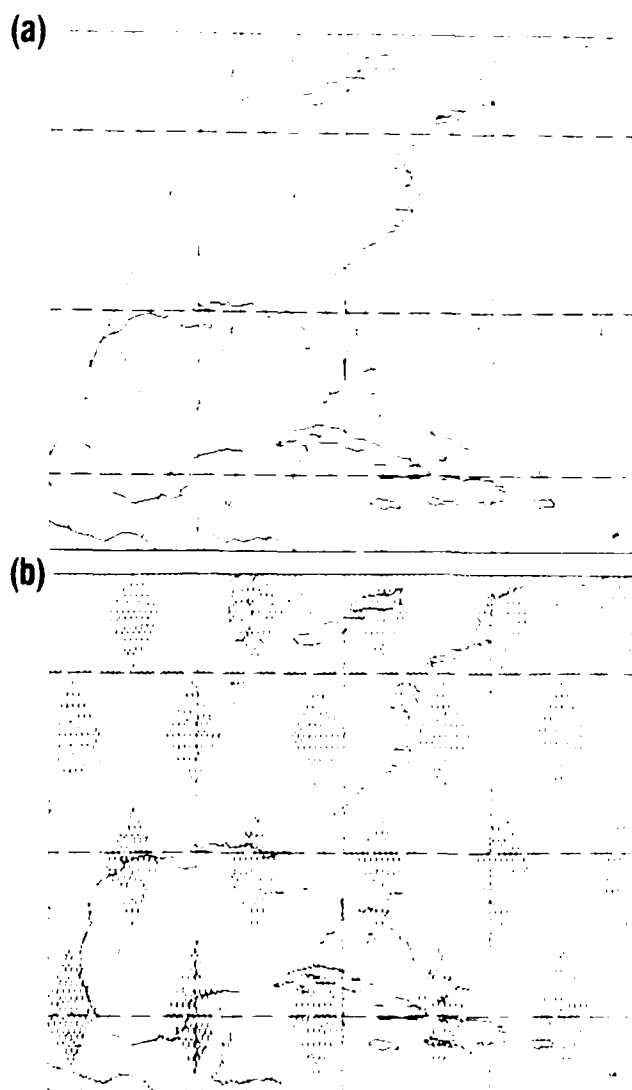


Fig. 2. Ascending and descending tracks during the nominal geosynchronous mission of GEOSAT. (a) Coverage after three days. At this point adjacent tracks in the Gulf of Mexico are 1 day apart and separated by approximately 900 km. (b) Track pattern after 30 days. The tracks fill the open regions from left to right. Adjacent tracks are three days apart and separated by approximately 36 km in the Gulf of Mexico. About 70 days are required for the entire pattern to fill in (courtesy of Z. Hallock, Naval Ocean Research and Development Activity (NORDA)).

where ξ is the free surface anomaly. Definitions for all symbols are provided in the notation section. Hence the interface (model pycnocline) slope is an inverted representation of the surface height field. This is an advantageous formulation for altimeter applications because the internal pressure field is uniquely determined by the sea surface height variations. In spite of its simplicity the model has demonstrated a remarkable ability to reproduce such observed features as the shedding of eddies from the Loop Current with realistic diameters, amplitudes, and westward propagation speeds [Hurlburt and Thompson, 1980].

Two numerical simulations of the Gulf of Mexico circulation have been chosen to serve as the model ocean. These "true" simulations will be sampled in order to obtain the simulated altimeter data; the results of the experiments that use the simulated measurements will be compared to the true solutions to assess optimum sampling and assimilation techniques. The first control simulation is experiment RG8 from Hurlburt and Thompson [1980]. The grid spacing is 20 km and the lateral eddy viscosity coefficient is $300 \text{ m}^2 \text{ s}^{-1}$. The values of other parameters are given in Table 1. In this simulation the period of the eddy shedding from the Loop Current has an average value of 366 days with a standard deviation of 37 days. The anticyclonic eddy, which is quite circular in shape,

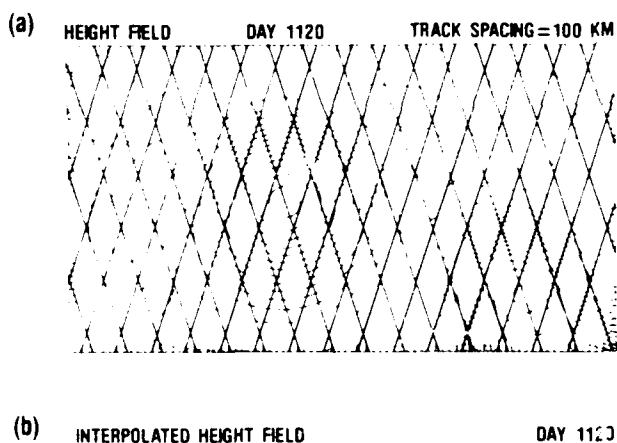


Fig. 3. (a) Ascending and descending tracks (separation equals 100 km) of an hypothetical altimeter superimposed on the GOM simulation at day 1120. The model is a one active layer reduced gravity formulation in which the slopes of the model interface and surface are related by $\partial \eta / \partial x = -\partial \xi / \partial x$. Hence the contours may be viewed as the deviation of the model interface (surface) from its initial flat position with a contour interval of 10 m ($\approx 3 \text{ cm}$). Solid lines denote a depression (rise) of the pycnocline (surface) and dashed lines represent a pycnocline (surface) rise (depression). The solution is treated as stationary during the sampling process. (b) A reconstruction of the numerical solution at day 1120 from the values sampled along the tracks in (a).

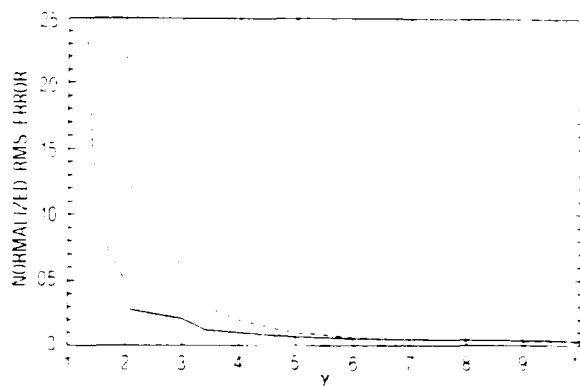


Fig. 4. The RMS error difference between the interpolated field and the true numerical solution of an isolated, stationary eddy as a function of the ratio γ of eddy diameter to track separation. The solid line is the RMS error when both ascending and descending tracks are used, whereas the dashed line is the same calculation utilizing only ascending or descending tracks. The RMS error is normalized by the standard deviation of the true solution.

propagates westward at an approximate speed of 4 cm s^{-1} . The interface deviation associated with the eddy has a maximum value of approximately 130 m, which corresponds to a surface signature of 39 cm. The eddy diameter is nearly 600 km, and maximum current speeds within this region are of the order of 70 cm s^{-1} . In the second control simulation the grid spacing and eddy viscosity are reduced to 10 km and $100 \text{ m}^2 \text{ s}^{-1}$, respectively; the values of other model parameters are unchanged. Although the essential features of the two solutions are similar, there are a few important differences. Among them are that in the 10-km experiment, the anticyclonic eddies which break from the Loop Current are noncircular, have larger amplitudes, and exhibit a much more irregular behavior pattern than in the 20-km case. In this simulation, the anticyclonic eddy is approximately the same size but much more irregularly shaped. The amplitude of the interface deviation is nearly 170 m ($\approx 50 \text{ cm}$ surface signature), and the westward propagation speed is about 4 cm s^{-1} . The eddy shedding period is slightly greater than 1 yr but has a much greater variability. Moreover, the behavior of the 10-km grid simulation is much more nonlinear and irregular than that of the 20-km grid case.

3. STATIONARY SAMPLING

An important parameter in the design of a sampling strategy is the minimum number of tracks across an eddy to ensure accurate mapping. The inverse relationship between track spacing and repeat period suggests that oversampling the eddy field with track spacing narrower than required may result in poor temporal resolution. The sampling dilemma is well illustrated in the Gulf Stream region by Cheney and Marsh [1981] and Cheney [1982] in whose work Seasat tracks are shown relative to the observed warm and cold core rings. Clearly, the spacing of the 17-day quasi-repeat track pattern is not sufficient to map all the eddies, but narrower spacing might not yield a sufficiently synoptic measurement.

As a first step in designing an optimum sampling strategy for mesoscale modeling and forecasting, the track spacing required to adequately resolve a stationary eddy is examined. The simulated altimeter measurements in this report are based on the orbital parameters (i.e., altitude, inclination, and track sequence) of the GEOSAT mission. The satellite track sequence during the first 18 months of GEOSAT is shown in Figure 2. The pattern produces an equatorial track separation

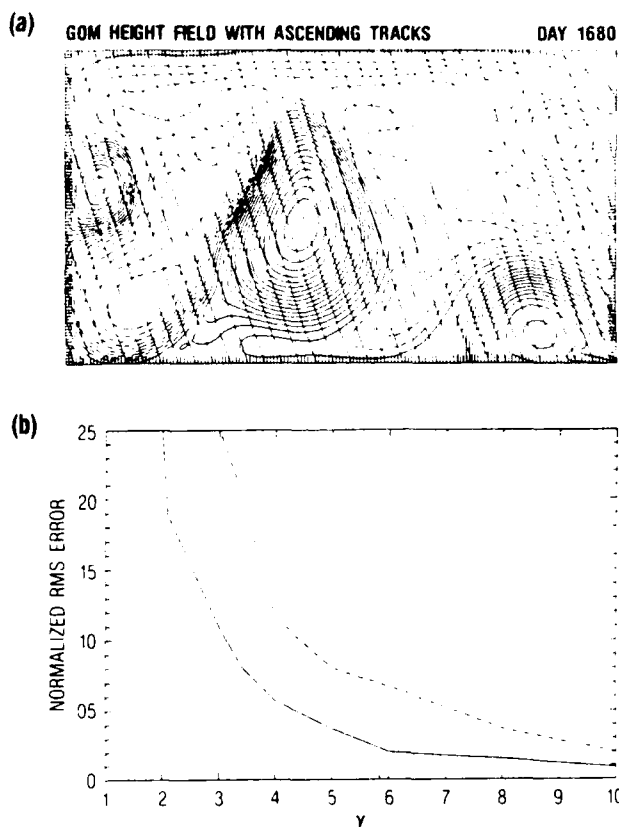


Fig. 5. Synoptic sampling of 10 km grid simulation. (a) Solution at day 1680 of fine resolution model ocean superimposed with ascending tracks (spacing equals 50 km). (b) Normalized RMS error as a function of ratio of eddy diameter to track spacing. Solid and dashed lines are as in Figure 4.

of 40 km with global coverage in approximately 70 days. (After GEOSAT was launched, the equatorial track separation was determined to be 117 km with global coverage in approximately 24 days (M. Lybanon, personal communication, 1985).) The tracks, however, do not repeat; the geodetic portion of GEOSAT will be followed by an extended mission with exactly repeating tracks and a shorter repeat track period [Mitchell *et al.*, 1985].

Track spacing is defined as the east-west distance between adjacent tracks aligned in the same direction. The poleward variation of the separation distance, which converges towards higher latitudes, is neglected in this study. This convergence is given, approximately, by the cosine of the latitude; hence the track separation at 25°N would only be reduced by about 10% from the equatorial value. Figure 3a shows the ascending and descending tracks with a separation of 100 km superimposed on the numerical solution at day 1120 of the 20-km experiment. The inclination angle of the tracks is the same as in Figure 2 (i.e., 72° for the descending tracks and 108° for the ascending tracks). The track sequence is not pertinent because the model ocean is assumed to be stationary. The values of the model pycnocline depth, which for a one-layer reduced gravity model are directly related to the free-surface elevation (equation (2)), are sampled approximately every 20 km along the tracks. Although a real altimeter samples much more frequently than every 20 km, the data are usually averaged in time to reduce observational noise. Typically, a 1-s average is used [for example, Cheney, 1982], which for satellites at the altitude of Seasat or GEOSAT yields an along-track sampling

interval of 7 km. Hence the 20-km sampling density used in these experiments is a coarse (although not unrealistic) sampling interval. Because, in general, the locations of the observation points do not coincide with the model grid points, the observation is an interpolated value from the numerical solution. The measurement locations are determined by the intersection of the altimeter tracks with lines of constant latitude passing through the height field points of the numerical grid. Hence an observation is a linear interpolation from the numerical solution of the two height field points on either side (E-W) of the measurement position. Bilinear interpolation was utilized to map the "observed" data back to the numerical grid.

Clearly, a track separation of 100 km is sufficient to determine the height field of Figure 3a very accurately; the RMS error difference between the height fields of Figures 3a and 3b is less than 1%. In order to determine the variation of the RMS error as a function of track spacing, the same calculations were performed for a variety of track separation values. The error is calculated only within a square circumscribing the large anticyclonic eddy and is normalized by the standard deviation of the true solution within the square. The error is presented as a function of the ratio of eddy diameter to track separation (γ) so that the results may be generalized to other situations.

The diameter of the eddy is taken to be 600 km; this value was determined from Figure 3a simply by averaging the distance between outermost contours of the eddy in the north-south and east-west directions. The calculated diameter of 600 km is larger than that given by other techniques, such as twice the e-folding radius or the distance between speed maxima. Hence for a given eddy, the calculated ratio of eddy diameter

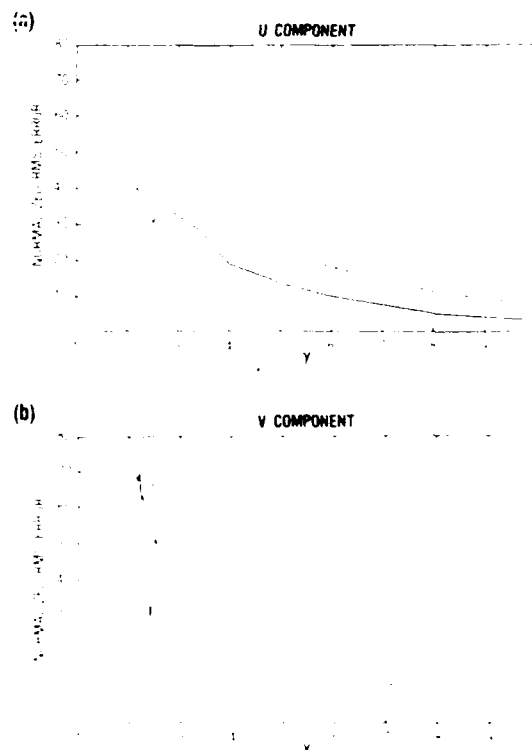


Fig. 6. Normalized RMS error of geostrophic velocity field as a function of ratio of eddy diameter to track spacing. (a) The u component. (b) The v component. Solid and dashed lines are as in Figure 4.

to track spacing is conservatively large. For each value of track separation, two values of the RMS error are calculated: (1) only one set of tracks, i.e., ascending or descending, is used in the analysis and (2) both ascending and descending tracks are used to reconstruct the height field. The results (Figure 4) reveal that if data from both tracks are used, track separation as large as an eddy radius adequately resolves the features. Additional tracks yield only a slightly improved representation. For cases in which the ascending and descending tracks sample the eddy at significantly different times, it may be advantageous to assimilate the observations from only one set of tracks. In such instances, Figure 4 suggests that approximately two or three tracks per eddy are required.

The necessary track spacing for an irregularly shaped eddy was examined by repeating the above sampling experiments with the 10-km Gulf of Mexico simulation. Day 1680 from this case was chosen and is shown in Figure 5a with ascending tracks 50 km apart superimposed. The average diameter of the

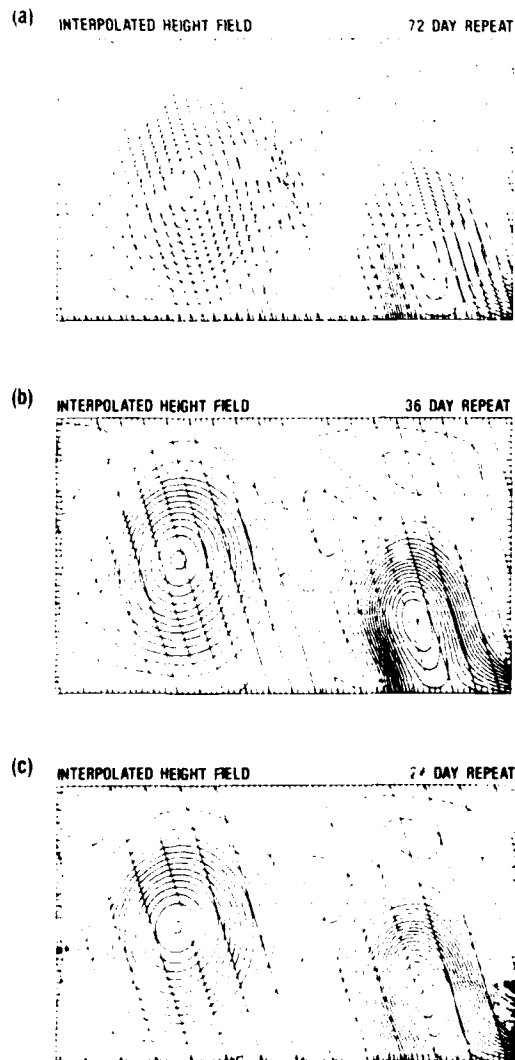


Fig. 7. Asynoptic sampling along the descending tracks of the 20-km grid simulation. Contours are the same as in Figure 3. Dashed straight lines denote position of tracks during the first half of the observing period, and solid lines depict satellite tracks during the most recent half of the repeat period. The most recent track (day 1200) is a solid line with an adjacent dashed line (oldest track) to the east. Repeat period for each case is (a) 72 days, (b) 36 days, and (c) 24 days.

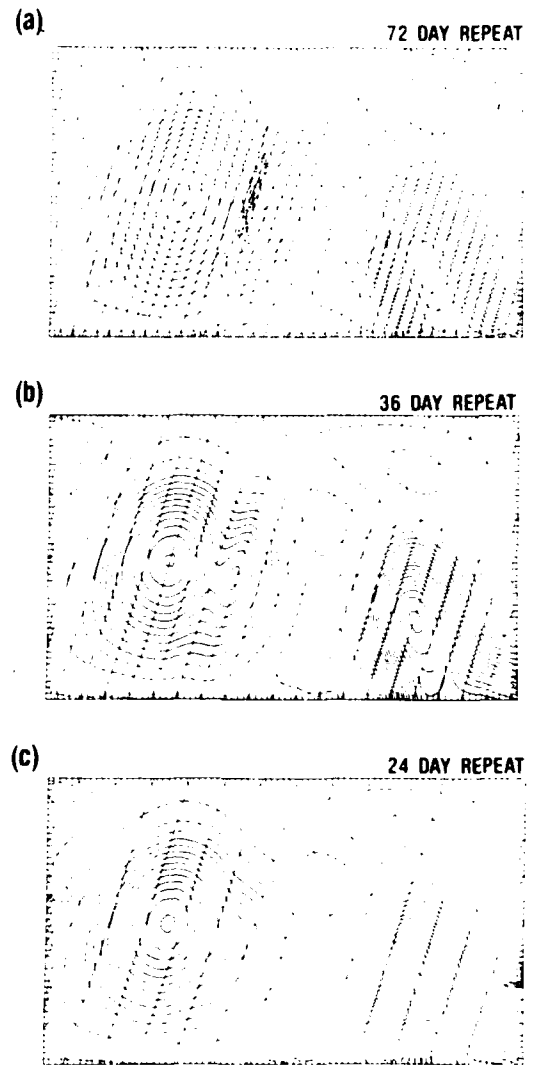


Fig. 8. As in Figure 7, but for ascending tracks. Repeat period is (a) 72 days, (b) 36 days, and (c) 24 days.

eddy is assumed to be 600 km. Figure 5b presents the normalized RMS error between the true and observed solutions as a function of the ratio γ . Not surprisingly, the noncircular eddy requires more tracks than the symmetric one. From Figure 5b, the "break point" occurs at approximately $\gamma = 4$; hence a noncircular eddy requires three or four tracks (ascending or descending) for adequate resolution.

The sampling requirements for the geostrophic velocity field are presented in Figure 6. Using the finer resolution experiment, the geostrophic velocity components are determined by differencing the height field for each track separation value in Figure 5a. The u (east-west) and v (north-south) components were computed after the simulated altimeter data were mapped onto the numerical grid. Figure 6 displays the RMS error of the geostrophic velocity components relative to the true geostrophic field associated with the major anticyclonic eddy. Note that the error in both the u and v components begins to increase markedly at approximately the same point as for the height field, i.e., at $\gamma = 4$. At higher values of γ (narrower track spacing), both velocity components are determined with comparable accuracy, although about twice that of the height field error. As the track spacing increases beyond $\gamma = 4$, the v field error increases much more rapidly than the u

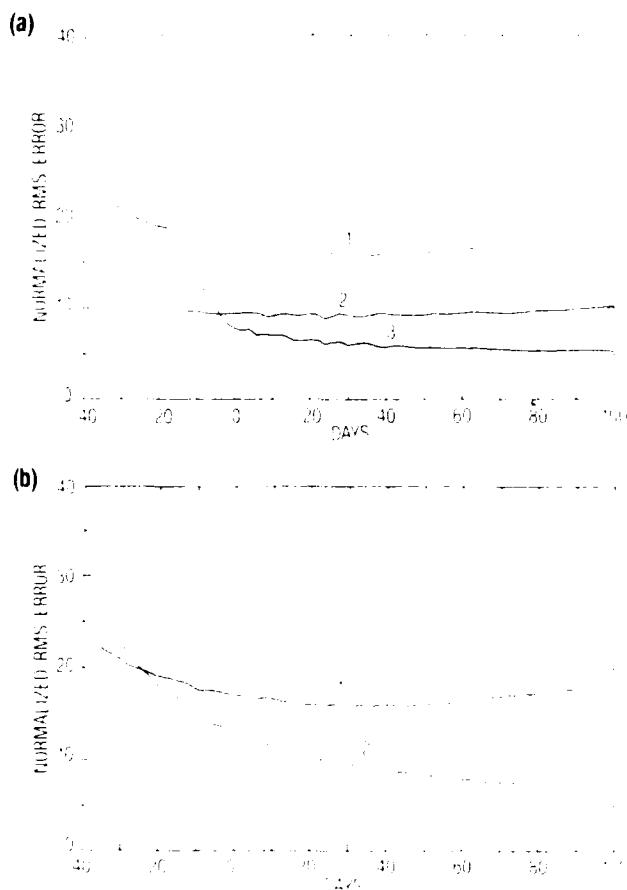


Fig. 9. (a) Normalized RMS error versus time of predictions initialized with ascending track observations: curve 1, 72-day repeat; curve 2, 36-day repeat; curve 3, 24-day repeat. Negative days denote nowcast period, while positive days indicate forecast. (b) Normalized RMS error versus time of forecasts in which the nowcasts were initialized with asynchronous observations from the 72-day repeat period: curve 1, initialized with ascending data (same as curve 1 in (a)); curve 2, initialized with descending track observations.

field because the v component is more nearly aligned with the along-track velocity component than with the cross-track component. The important point is that if the track spacing adequately resolves the eddy height field, the geostrophic velocity components (regardless of track orientation) are determined with equivalent accuracy. Hence even satellites with high inclination angles, i.e., polar orbiters, can provide the north-south velocity field given track spacing sufficiently narrow to determine the height field.

4. ASYNOPTIC SAMPLING AND ASSIMILATION, PART I

A variety of techniques have been developed for the assimilation of asynchronous observations into numerical weather prediction (NWP) models [Bengtsson *et al.*, 1981]. The NWP initialization, updating problem is one of combining the observations from the extensive synoptic network with asynchronous observations such as remotely sensed data. Recently, the statistical-dynamical methods developed for NWP have been modified and applied to the numerical prediction of ocean circulation in limited area, open boundary regions [DeMey and Robinson, 1984; Robinson and Leslie, 1985]. DeMey and Robinson specifically address the assimilation of altimeter data into quasi-geostrophic models for the POLYgon Mid Ocean Dynamics Experiment (POLYMODE) region. Their four-dimensional assimilation techniques arrive at an initial

condition for the forecast by utilizing predetermined statistical parameters of the circulation fields in conjunction with satellite and in situ observations. In regions where the statistical parameters are adequately determined, such objective analysis schemes are very promising. In addition, such statistical techniques permit the formulation of optimum sampling strategies in terms of correlation length and time scales. If, however, a basin-wide forecast is desired (either as an end in itself or to provide boundary information for an open ocean forecast), synoptic in situ data are extremely sparse, and the statistics of the flow field may not be adequately determined throughout the basin. In such cases it may be necessary to determine the initial state of the forecast using only asynchronous satellite data and utilize the dynamics of the model as the primary constraints on the assimilation. It is in this sense that the assimilation experiments are presented herein. The techniques are admittedly simple and intended to explore fundamental capabilities and problems of dynamic assimilation of asynchronous data.

The inverse relationship between repeat track period and track separation for a single nadir beam altimeter demands a prudent sampling and four-dimensional assimilation strategy for optimum results. If the dynamical features of interest necessitate narrow track spacing, the temporal resolution may be inadequate unless a numerical model is able to fill in the temporal gaps. This problem is illustrated by Figure 7, in which the interpolated Gulf of Mexico height field is shown for repeat track periods of 72, 36, and 24 days; the respective track separation values for these periods are 40, 80, and 120 km. The 20-km grid GOM simulation is utilized as the "true" ocean height field. The model ocean is sampled during the repeat period in a manner similar to that of a real altimeter. The track sequence is virtually identical to that shown in

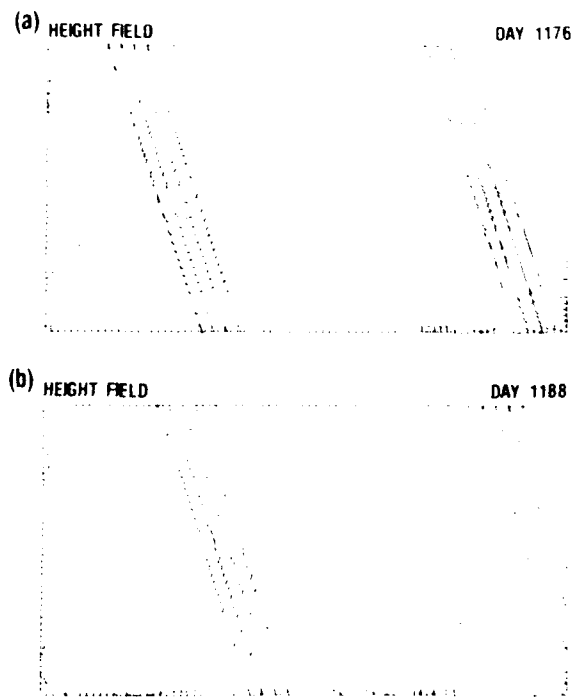


Fig. 10. Contours of height field during nowcast initialized at day 1164 with asynchronous data from the ascending tracks of the 72-day repeat period (see Figure 9b). (a) Day 1176 superimposed with tracks along which data are to be inserted. For both sets of tracks, the corresponding day of the track is, from left to right, day 1167, 1170, 1173, and 1176. (b) Same as (a), but 12 days later.

Figure 2, except that the tracks that are separated by approximately 900 km in space and 1 day in time (Figure 2a) are assumed to occur on the same day. This slight difference merely simplifies the assimilation experiments but does not modify the results. In addition, the satellite is assumed to lay down exactly repeating tracks; the spacing between adjacent tracks is the equatorial separation distance.

The reconstructed height fields shown in Figure 7 were obtained by using only information from the ascending tracks and by treating the asynoptic observations as synoptic. The most recent satellite track occurs on day 1200 of the model simulation and is approximately at the same position for each of the three sampling periods. In order to ensure uniform coverage of the basin, the hypothetical altimeter samples the model ocean for a duration nearly equal to the repeat track period. Hence the sampling period is from day 1131 to day 1200 for the 72-day repeat track case, day 1167 to day 1200 for the 36-day case, and from day 1179 to day 1200 for the 24-day repeat track period. No four-dimensional assimilation techniques were employed to construct the fields shown in Figure 7. The essential result of these sampling experiments is that the westward propagation of the anticyclonic eddy, together with the eastward progression of satellite tracks, causes the eddy to be distorted, with the greatest distortion being just east of the most recent track. Clearly, the 72-day repeat track case is affected most by the asynoptic sampling. Although the 24-day case does exhibit some distortion of the eddy, its primary disadvantage is poor spatial resolution, particularly along the meridional boundaries.

It should be noted that the ground tracks of the nominal GEOSAT orbit will be modified for the extended mission to repeat exactly with a period of 17 days. The primary alternate orbit has a 34-day repeat period (J. L. Mitchell, personal communication, 1985). The 17-day repeat period orbit was not examined in this study; for track spacing greater than 130 km, the simple interpolation scheme generated large gradients along the N-S boundaries that the model could not handle. Future experiments will incorporate a more sophisticated interpolation scheme, and the shorter repeat orbits will be examined.

The numerical experiments in this section begin with nowcasts that are initialized from the asynoptic altimeter data of the 72-, 36-, and 24-day repeat track sampling periods. The

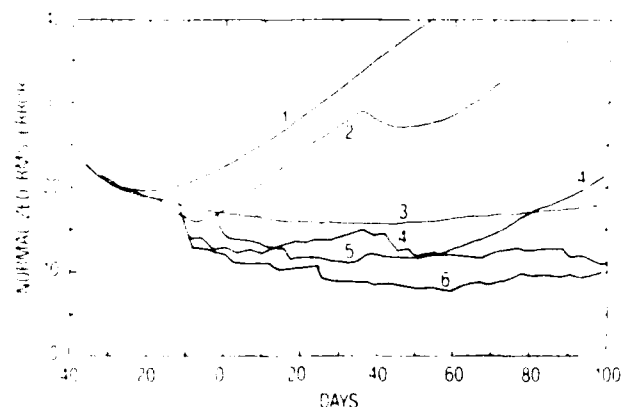


Fig. 11. Normalized RMS error versus time of forecasts in which updating interval is varied. Curve 1, no updating, but field is reinitialized with geostrophically balanced velocity field every 3 days; curve 2, update every 3 days; curve 3, no update, same as curve 1 in Figure 9b; curve 4, update every 6 days; curve 5, update every 18 days; curve 6, update every 12 days.

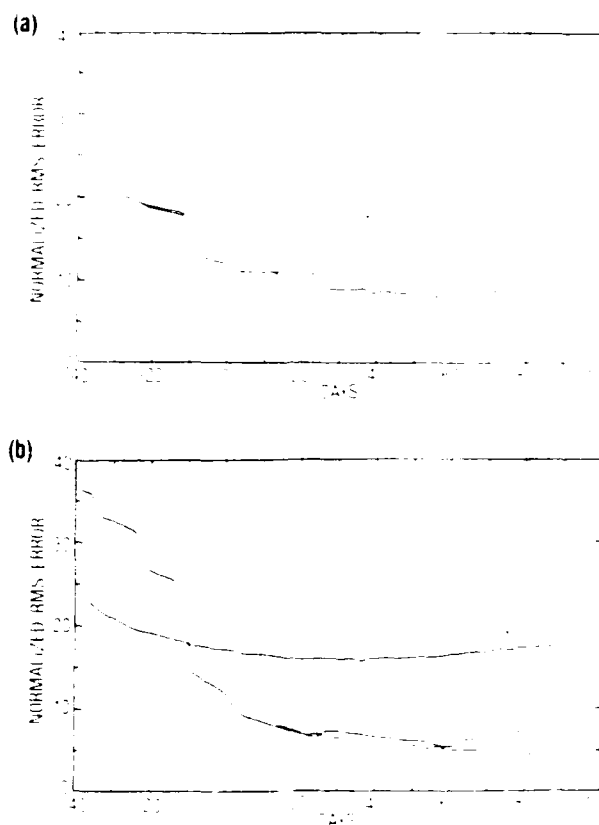


Fig. 12. RMS error versus time of forecasts in which duration and timing of updating is varied. When updating is applied, the period is every 12 days. (a) Nowcast initialized at day -36: curve 1, no updating, same as curve 3 in Figure 11; curve 2, update nowcast but not forecast; curve 3, update nowcast and forecast. (b) Curve 1, same as 1 in (a); curve 2, nowcast initialized at day -72 and updated every 12 days. Forecast is not updated; curve 3, update nowcast and forecast.

RMS errors of the forecasts relative to the true solutions are calculated and compared. It is shown that two forecasts initialized with the data from the ascending and descending tracks, respectively, yield significantly different results—a finding that is incompatible with the development of an accurate forecasting methodology. An initialization scheme is developed that updates the nowcast with the simulated altimeter data in order to provide a more accurate initial condition for the forecast. The optimum updating period and the consistency of the initialization scheme are examined. Finally, forecasts utilizing the initialization scheme and the asynoptic data from the 72-, 36-, and 24-day sampling periods are generated.

A quantitative assessment of the space time sampling schemes is determined by initializing the numerical model using the simulated altimeter data, running the model in forecast mode, and calculating the RMS difference between the forecast and the true solution. Initial conditions are determined by treating the simulated altimeter observations as a synoptic "snapshot" valid at the midpoint of the observing period. Initial velocity components are determined geostrophically from the height field. Because the most recent satellite track used in the initialization is at day 1200, this is designated as the start (day 0) of the forecast; the duration of the forecast is 100 days. The forward integration of the model prior to day 1200 is the nowcast, the purpose of which is twofold: (1) to yield an accurate depiction of the present oceanic circulation and height field, and (2) to provide an initial condition for the

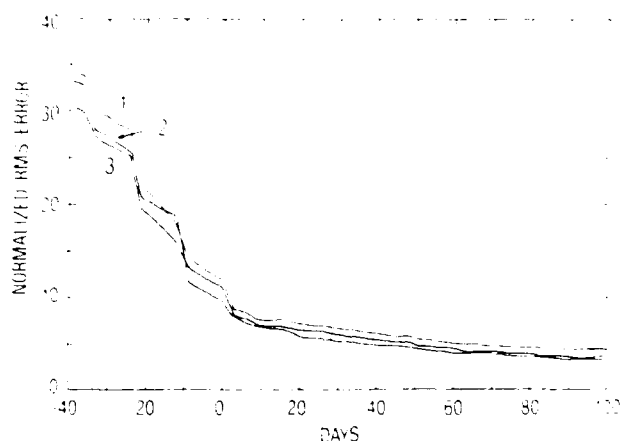


Fig. 13. Normalized RMS error versus time of forecasts using various combinations of ascending and descending track data from 72-day repeat period observations. Nowcast is initialized at day -72; updating is applied during nowcast only. Curve 1, nowcast initialized and updated with ascending track data. Same as Figure 12b, curve 2; curve 2, nowcast initialized with descending track data but updated with observations from ascending tracks; curve 3, nowcast initialized and updated from descending track observations.

forecast. In the first set of experiments the nowcast is initialized at the midpoint of the observing period; the forecast is always initialized at model day 1200. The forcing of the circulation through the Yucatan Straits, which is constant in time, is the same for each experiment.

The initial data for the first three forecast experiments, i.e., for the 72-, 36-, and 24-day repeat track cases, are based on observations along the ascending tracks (Figure 8). The descending tracks or a combination of ascending and descending tracks could also be used; the ascending tracks were chosen because they exhibit less distortion of the large anticyclonic eddy. Also, it is advantageous for experimental duplication to separate the two data sets because they represent two "independent" realizations with which to initialize a model. A blending of observations from the ascending and descending tracks could be accomplished by a four-dimensional optimal interpolation scheme, an approach that is not being addressed in this report. The results of these initial forecast experiments are shown in Figure 9a as a time series of RMS difference between the forecast height field and the true solution. The RMS error is calculated only over the westernmost 1000 km of the basin in order to focus on the isolated westward propagating eddy. Hence the relatively steady and directly forced Loop Current is not included in the error analysis. The RMS error is normalized by the true solution. These solutions suggest that for this Gulf of Mexico simulation the track spacing of the 24-day sampling case (120 km) is sufficient to resolve the primary features; the asynopticity introduced by the longer repeat track periods yields a less accurate forecast.

Unfortunately, the comparison is not quite so simple. If the model nowcast is initialized with the data from the descending tracks, the resulting forecast is substantially improved, even though the initial height field has a larger RMS error (Figure 9b). The essential difference between the two experiments is that the "nowcast" initialization with the descending track data is more nearly in phase with the true solution; when the Loop Current sheds the next anticyclonic eddy, it more accurately predicts the position of the eddy as it propagates westward. This is a coincidental result that depends upon the relative timing between the sampling of the most important dynamic feature(s) and the date chosen to initialize the nowcast.

The accuracy of the 36-day repeat track experiment can also be improved by adjusting the phase of the nowcast initialization (not shown). The 24-day experiment, however, shows little difference as to whether the ascending or descending data are used to initialize the forecast: the propagation of the eddy is sufficiently slow that the observations approach a synoptic realization.

In a true forecast experiment, however, the most appropriate phase of the initial nowcast field is an unknown. Hence it is important to develop an initialization scheme which consistently yields an accurate nowcast (day 0 of the forecast) with zero phase shift relative to the true solution throughout the model basin. As was evident in the previous experiments, the altimeter observations can form a nearly synoptic representation of the true solution if the tracks repeat at a sufficiently high frequency relative to the time scale of the oceanic phenomena. If, however, the ocean features require a narrower track spacing (longer repeat periods), the asynopticity of the observations may become a serious problem. The goal of the experiments described below is to test whether the numerical model can convert asynoptic observations into a consistently accurate nowcast forecast of the model ocean. The asynoptic observations will be assimilated into the model periodically so that the spatial variability of initial phase differences are reduced or eliminated. The primary questions that will be addressed are (1) model stability to periodic injection of data over limited domains, (2) the optimum frequency of inserting new data, i.e., updating the forecast, and (3) the major problems associated with such an initialization updating scheme in a real forecast situation.

The initialization/updating scheme is tested using the 72-day repeat track case. Adjacent tracks are 40 km apart in space and 3 days in time. The model is initialized from the asynoptic set of observations (Figure 8a), which are assumed to be valid at day 1164 (i.e., day -36 of the forecast). The model is integrated forward in time and stopped every T_u days, where T_u is the updating interval. For example, if the updating period is 3 days (that is, the tracks are inserted one at a time), the model is integrated to day 1167, and the altimeter height data observed along the track on day 1167 are inserted into the model in exactly the same manner as the original observations. The height field is remapped to the numerical grid, and

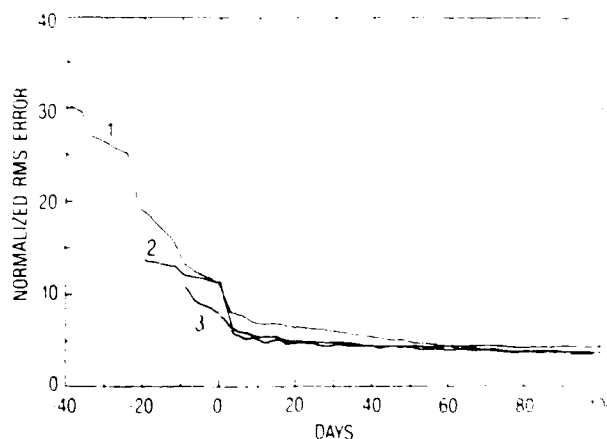


Fig. 14. Normalized RMS error versus time of forecasts for three repeat track periods. Nowcast is initialized at the beginning of the observation period and updated every 12 days. Only observations from ascending tracks are used. Repeat periods are as follows: curve 1, 72 days; curve 2, 36 days; and curve 3, 24 days. Compare with Figure 9a.

a new initial geostrophic velocity is obtained throughout the basin. From this new initial field on day 1167 the model is integrated to day 1170, at which time the altimeter observations taken along the track(s) on day 1170 are inserted into the solution. The insertion of new altimeter data into the model is effected by the following sequence: (1) the nowcast forecast is sampled, e.g., at day 1176, using a simultaneous set of tracks (i.e., as in the stationary sampling of section 3) that exactly overlay the altimeter tracks, (2) the height field along the tracks associated with the update are replaced by the altimeter data along the designated tracks (Figure 10), (3) the height field throughout the basin is reinterpolated to the numerical grid, (4) the new height field is differenced to obtain the geostrophic velocity field, and (5) the model is reinitialized and integrated to the next update time. For the 72-day repeat track forecast the error introduced by the stationary sampling is small because the track spacing (40 km) accurately determines the height field with an error of less than 1‰ (Figure 4). For the 36-day repeat track case, every other track of the simultaneous "comb" coincides with an altimeter track; for the 24-day repeat period, every third track is replaced by altimeter data. If the updating period is 12 days, the model is first integrated to day 1176, and four tracks are inserted at a time (Figure 10). This initialization updating (henceforth IU) scheme continues into and through the forecast period because the technique is equivalent to updating the forecast with new altimeter data.

A number of forecast experiments were conducted with the updating period varying from 3 to 18 days. An additional experiment was performed to test the effects of geostrophic initialization; the model integration was halted every 3 days and reinitialized with the same height field and the geostrophically balanced velocity field. The primary sources of forecast error in these experiments are (1) the asynopticity of the data, (2) the generation of gravity waves by the insertion of new data and the geostrophic initialization scheme, and (3) the spatial interpolation of the altimeter measurements to the numerical grid. An additional possible contribution to the error is the accumulation of noise due to the interaction of the non-linear terms in the model. From the many experiments conducted in this study, as well as those performed by *Hurlburt and Thompson* [1980], this source of error is judged to be much smaller than those listed above. In addition, the 40-km track spacing is sufficiently narrow to rule out spatial interpolation as a significant error source. Hence the forecast error is due to a combination of the asynopticity of the data and the generation of gravity wave noise. The reduction of the asynoptic error depends upon the frequency of application of the updating scheme. As the updating interval increases, the inserted data represent the observations at a particular time less accurately. The forecast error approaches that of the nonupdated forecast as the updating interval nears the repeat track period. Optimally, inserting one track at a time corrects the asynopticity most effectively. However, frequent application of the updating scheme generates gravity wave noise. The results are shown in Figure 11. The optimum updating interval was found to be 12 days or four tracks at a time. Intermittent updating at longer intervals did not correct for the asynopticity of the observations as effectively. If the interval is shorter than 12 days, the forecast is degraded by the buildup of spurious gravity wave noise generated by the updating scheme. The experiment in which only a geostrophic initialization is performed every 3 days reveals that the frequent restarting of the model with a geostrophically balanced velocity field is the primary source of spurious gravity wave energy. It should be noted that a more sophisticated technique for determining the

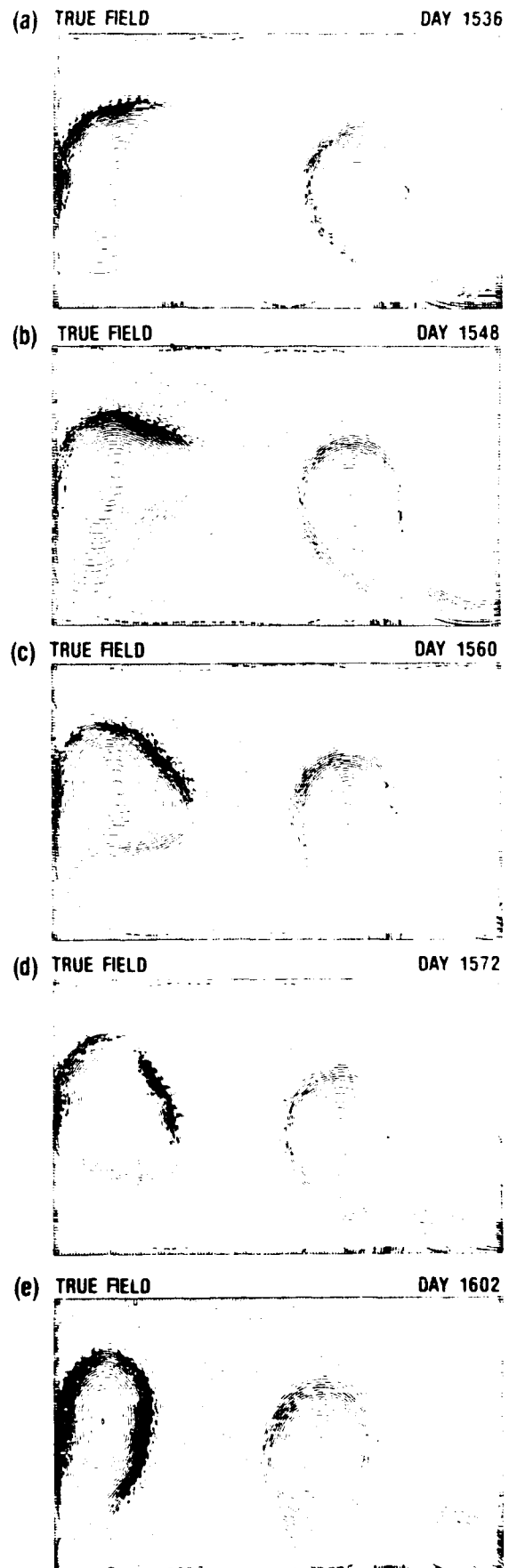


Fig. 15. Contour plots of height field for finer resolution (10-km grid) Gulf of Mexico simulation. (a) Day 1536, (b) Day 1548, (c) Day 1560, (d) Day 1572, (e) Day 1602. For contour interval, see Figure 3.

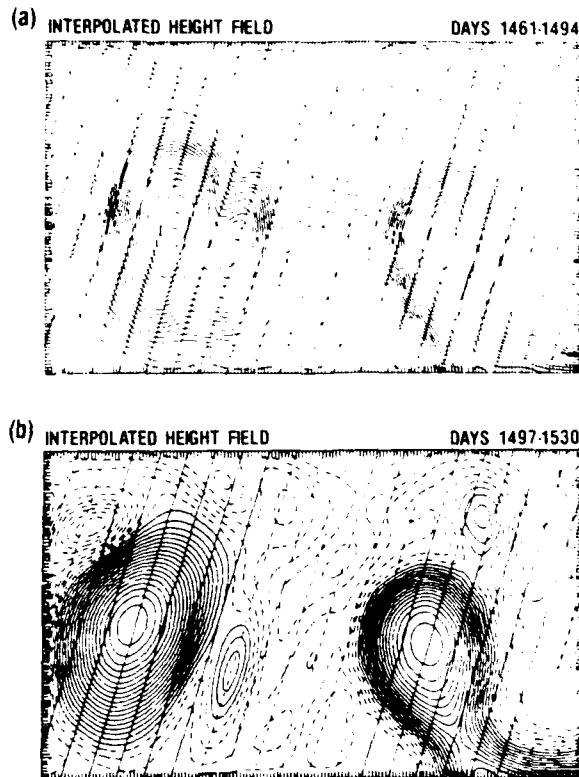


Fig. 16. Asynoptic sampling of 10-km grid GOM simulation using 36-day repeat tracks (descending only). Track spacing is 80 km. For explanation of solid and dashed straight lines, see Figure 7. (a) Sampling occurs from day 1461 to day 1494. (b) Model ocean sampled from day 1497 to day 1530.

initial velocity field, such as a nonlinear balance equation or the balancing scheme of Ghil [1980] (to name just a few), might reduce the amplitude of the spurious gravity waves. Experiments with the 36-day repeat track observations also revealed that the most effective updating interval was 12 days. Hence the optimum updating interval for these GOM simulations is at least every 12 days.

The experiments depicted in Figure 11 reduced the forecast error by (1) improving the nowcast (i.e., generating a more accurate initial state for the forecast) and (2) updating the forecast with new altimeter data. In the next set of experiments, the relative effects on the forecast error of these factors are examined. The updating interval for these experiments is 12 days. A forecast is generated that is initialized by the nowcast but not updated during the forecast period. Figure 12a reveals that updating the forecast improved the prediction after approximately 25 days. If, however, the nowcast is started at the beginning of the observation period, i.e., at day -69, and the two experiments are repeated, the result is quite different. Figure 12b reveals that the RMS error begins to increase at day 60 if the updating continues during the forecast. This is due to the very slow accumulation of inertia-gravity wave noise that only begins to degrade the forecast after approximately 130 days of integration. Note that if the nowcast is initialized with the asynoptic data at the beginning of the observing period, the initial RMS error of the nowcast is necessarily large. As the IU scheme proceeds, all the observed data are reinserted into the model at (or near) the appropriate time, and the RMS error rapidly decreases as day 0 of the forecast is approached.

Note that updating the forecast did not improve the prediction because this GOM simulation is a well-behaved initial value problem. No external forcing (except a constant inflow through the Yucatan Straits) was applied, and the circulation exhibited no instabilities during the forecast period. The satellite track spacing provided adequate spatial resolution, and the IU scheme yielded an accurate nowcast. Hence initialization with a proper nowcast was sufficient to yield an accurate forecast. Many other oceanic regimes, however, will require an updated forecast.

The consistency of the initialization updating scheme is tested by generating independent forecasts based on the observations from the ascending and descending tracks, respectively. Recall from Figure 9b that when the nowcast is not updated, the "ascending" and "descending" forecasts differed substantially. The first experiment is the forecast described above, in which the nowcast was initialized at the beginning of the observations period and updated with the ascending track data. The second forecast is identical except that the descending track data are used to initialize and update instead of the ascending track observations. A third forecast is generated in which the nowcast is initialized with descending track data but is updated with observations from the ascending tracks. This experiment is designed to test the sensitivity of the nowcast to variations of the initial state. In all of the experiments there is no updating during the forecast phase. The RMS errors of the forecasts (Figure 13) are essentially the same for all three experiments. Clearly, the IU scheme yields a consistently accurate nowcast in which the error decreases on the time scale of the repeat period.

Finally, forecasts are conducted using the 72-, 36-, and

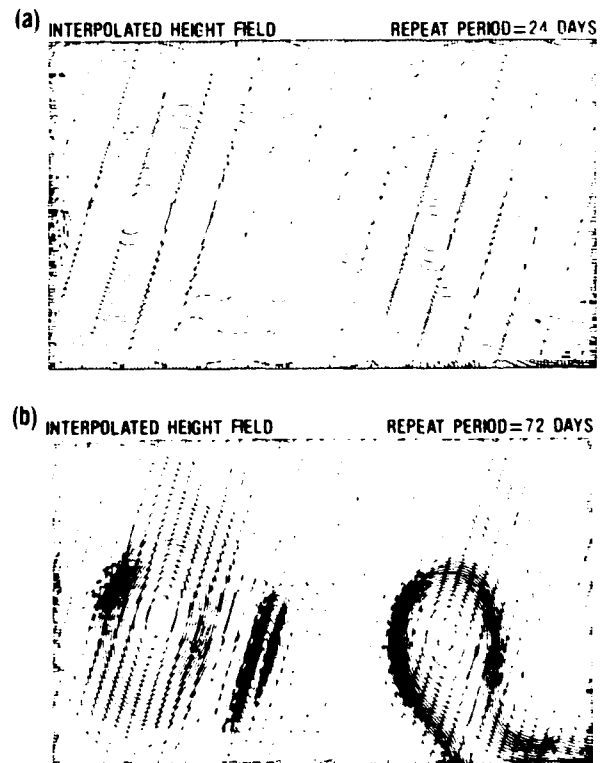


Fig. 17. Asynoptic sampling (descending tracks only) of 10-km grid GOM simulation for two repeat periods (a) 24-day repeat track period (days 1461 to 1530) and (b) 72-day repeat track period (days 1461 to 1530). The corresponding track spacing is 120 km in (a) and 40 km in (b).

24-day repeat track observations and the initialization technique discussed above. In each experiment the nowcast is initialized with the descending track data (Figure 8) at the beginning of the observing period, and the nowcast is updated every 12 days. No updating is performed during the forecast. The results (Figure 14) show that the forecasts using the 24- and 36-day repeat track data are virtually indistinguishable. Surprisingly, the RMS error of the forecast from the 72-day sampling period is only slightly larger; after 50 days, all three forecasts have equivalent errors. This is a very encouraging result for the use of satellite altimeter observations with numerical models. It suggests that the inherent asynoptic nature of the altimeter measurement may be substantially reduced by an initialization updating scheme that uses a numerical model to assimilate the data.

It should be noted that in a real forecast situation, additional sources of error are (1) measurement noise (including environmental effects and geoid uncertainty), (2) orbit error, (3) vertical assimilation of the surface observations into subsurface information, and (4) all the approximations inherent in a numerical simulation of real physical processes. Although these are nonnegligible error sources, this work focuses on the temporal spatial resolution problems of a single nadir beam altimeter.

5. ASYNOPTIC SAMPLING AND ASSIMILATION, PART 2

The experiments in the previous section presented an encouraging demonstration of model assimilation of asynoptic altimeter data. In this section, the simulation from which the observations are drawn is changed to one with much greater temporal and spatial variability. The GOM simulation with 10-km grid resolution and an eddy viscosity coefficient of 100 $\text{m}^2 \text{sec}$ is used. The forecast period is shortened to 72 days; day 0 of the forecast is model day 1530. This is approximately 1 year later than for the 20-km grid solution because the lower eddy viscosity requires a longer spin up time to attain statistical equilibrium. As noted in section 2, the behavior of the solution is much more irregular than the 20 km grid simulation. Figure 15 reveals snapshots of the height field for days 1536 to 1602. Note the movement of the small cyclonic eddy clockwise along the perimeter of the large anticyclonic eddy in the western portion of the basin. The diameter of the small eddy at day 1497 is approximately 200 km. The region be-

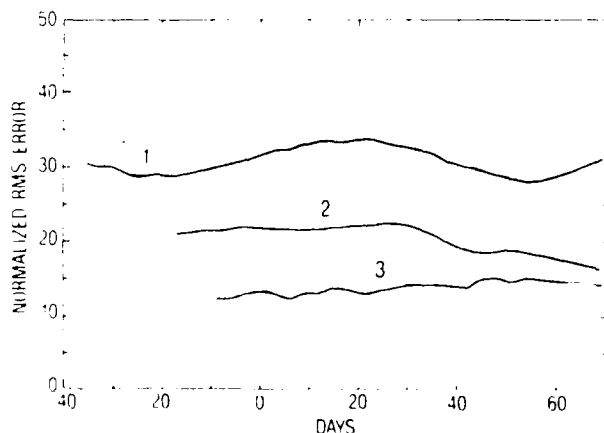


Fig. 18. Normalized RMS error versus time of forecasts in which the nowcast is initialized with asynoptic observations from three repeat track periods. Curve 1, 72-day repeat (Figure 17b); curve 2, 36-day repeat (Figure 16b), and curve 3, 24-day repeat (Figure 17c). No updating is applied.

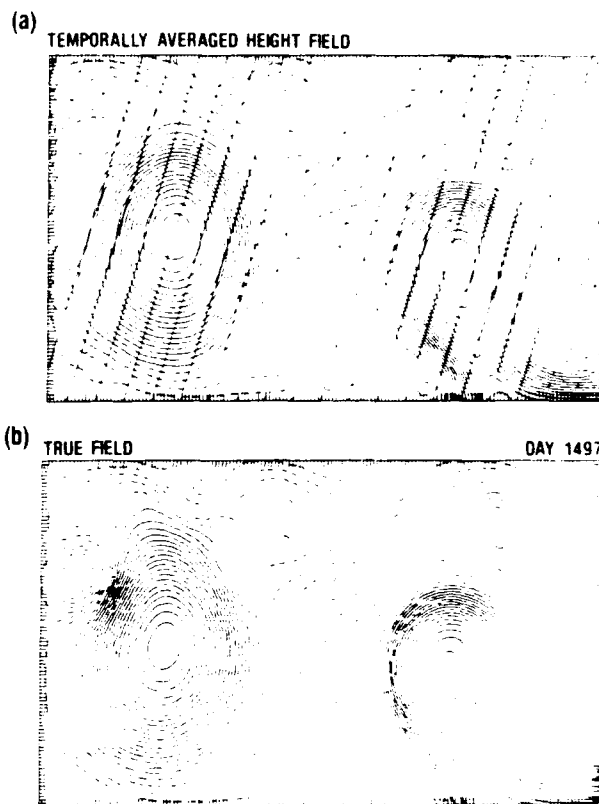


Fig. 19. (a) Resultant height field for 36-day repeat period if data along each set of repeating tracks (Figure 16) are interpolated in time to day 1497. (b) True solution of 10-km grid simulation at day 1497.

tween the two eddies is characterized by very sharp pressure gradients, and the clockwise rotation of this feature is associated with significant distortion of the large eddy. Both these aspects of the solution present a challenging forecasting situation.

The sampling procedure for the simulated altimeter data is identical to that of the 20-km grid experiments, except that the model is sampled every 10 km along the track instead of every 20 km. Asynoptic sampling along tracks which repeat every 72-, 36-, and 24-days is conducted. The observations along the descending tracks for two consecutive 36-day repeat track periods are shown in Figure 16. The most recent track in Figure 16a is on day 1494, while in Figure 16b, the same track is on day 1530. The asynoptic sampling for the 24- and 72-day repeat track periods is shown in Figure 17. Forecasts are generated in which the model nowcast is initialized with the asynoptic observations, and there is no subsequent application of an IU scheme. The forecast procedure is identical to the 20-km grid experiments; the nowcast is initialized at the midpoint of the observing period with the most recent data from the descending tracks. The results (Figure 18) reveal that the 24-day sampling period yields the most accurate prediction. Although the fine resolution case contains numerous small-scale features, the primary features are sufficiently large that the track spacing of the 24-day repeat pattern yields adequate resolution. This is true even for the small cyclonic eddy in the western gulf. The RMS errors of all the forecasts, however, are approximately twice that of the corresponding 20 km forecasts.

Prior to examining predictions that use an updating technique, a forecast is conducted from the 36-day repeat track

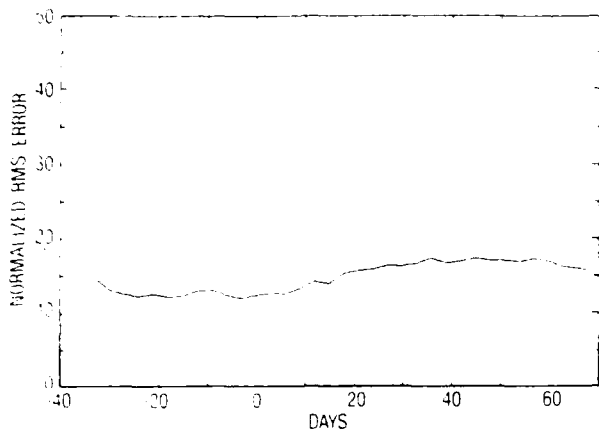


Fig. 20. Normalized RMS error versus time if forecast is initialized at day 1497 (day -33 of prediction) using the height field of Figure 19a. No updating is applied.

sampling using a different scheme for the nowcast initialization. The data from the previous 36-day sampling period are used (i.e., days 1461 to 1494). Because the time of the observations along each exactly repeating track bracket day 1497, the data are interpolated in time to that day. Hence before mapping the observations to the numerical grid, the data from each set of repeating tracks are used to find the interpolated value at day 1497. This is a simple attempt to produce an initial condition for the nowcast with a more uniform phase distribution relative to the true solution (Figure 19). The interpolated field is surprisingly similar to the true solution in view of the asynoptic nature of each data set (Figure 16). The nowcast is initialized at day 1497 with the interpolated field; the RMS error of the resulting forecast (Figure 20) is substantially less than that using the asynoptic initialization, at least out to day 40.

Because of limited computer resources and the cost of the 10-km grid runs, the study was limited to just a few predictions using the IU scheme. Focus is placed only on the forecasts utilizing 36-day repeat track observations. Two experiments are conducted in which the nowcast is updated four tracks at a time every 12 days until day 0 of the forecast; subsequently, there is no updating of the forecast. In the first experiment the nowcast is initialized with the asynoptic observations (Figure 16b) at day 1497; in the second experiment the nowcast is initialized with the time interpolated field (Figure 19a) also at day 1497. Figure 21a demonstrates that the IU scheme improves the forecast throughout the duration of the prediction. Just as in the 20-km grid forecasts, the application of updating to the nowcast reduces the RMS error to approximately that of the 24-day repeat period forecast.

In the final experiment the prediction continues to be updated during the first 48 days of the forecast; this is a continuation of the nowcast initialized by the temporal interpolation and updated every 12 days. The RMS error of the updated and the nonupdated forecasts are plotted in Figure 21b. Updating the forecast did not improve the accuracy of the solution, but for a different reason than in the 20-km grid case described in section 4. In the 20-km grid forecasts the accumulation of gravity wave energy eventually degraded the forecast. In the 10-km grid forecasts the errors are due to cyclonic eddies generated by the periodic insertion of new data into the model solution. The intense pressure gradient on the perimeter of the large anticyclonic eddy and the low value of lateral viscosity coefficient excite cyclonic eddies at the edge(s) of the

data patch inserted by the IU scheme. The spurious eddies generated in this unstable regime can persist for a month or longer. This is clearly depicted in Figure 22, which displays "snapshots" 1 month after the start of the forecast (model day 1560) for each of the five forecasts based on the 36-day repeat track observations; the true numerical solution at day 1560 is also shown. Figure 22f shows an intense cyclonic eddy in the northwest corner of the basin; this eddy is only weakly indicated in the true field (Figure 22a). Although the 10-km grid solution presents a difficult challenge for accurate simulated forecast studies, it does suggest that altimeter data assimilation in unstable regions may require sophisticated techniques for blending the observations into the model.

The remaining panels in Figure 22 clearly show the value of updating the nowcast. Each case in which the IU scheme was applied during the nowcast reveals a more realistic (i.e., in comparison to Figure 22a) anticyclonic eddy; the pronounced asymmetry of the large eddy is better defined (Figure 22c and 22d). During the observation period the diameter of the cyclonic eddy was approximately 200 km, and it translated at a speed of about 5.6 cm/s. Note that these values are consistent with observations of Gulf Stream rings [Lai and Richardson, 1977]. Given these parameters of the eddy, it is encouraging that (1) the 120-km track spacing of the 24-day repeat tracks adequately resolved the 200-km eddy, and (2) the asynoptic nature of the 36-day repeat tracks could be corrected by the application of an initialization/updates scheme. The results suggest that the assimilation of data from a single beam altimeter into a numerical forecast model may be able to monitor the

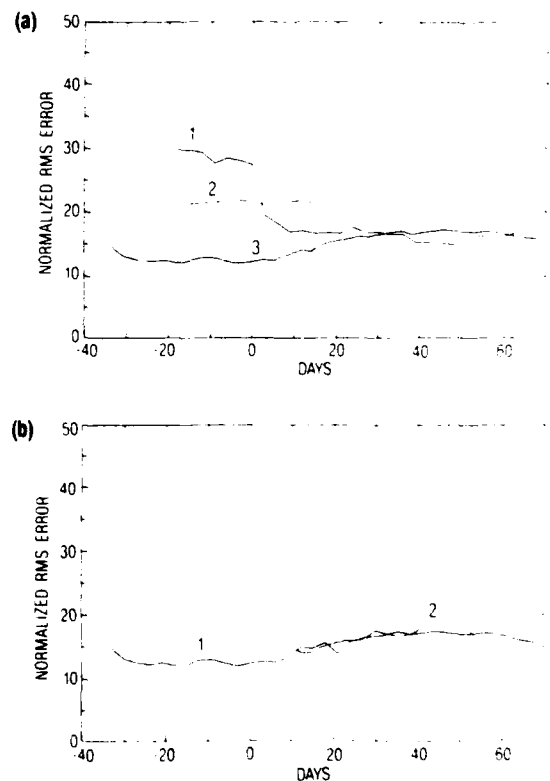


Fig. 21. Normalized RMS error of forecasts for 10-km grid simulation using descending track data from 36-day repeat period. (a) Curve 1, Nowcast is initialized with asynoptic observations (Figure 16b) and updated every 12 days; curve 2, same as 1, except that no updating is applied; curve 3, nowcast is initialized with time-interpolated height field (Figure 19a) and updated every 12 days. (b) Curve 1, same as curve 3 in (a); curve 2, same as 1, except that nowcast and forecast are updated to day 48.

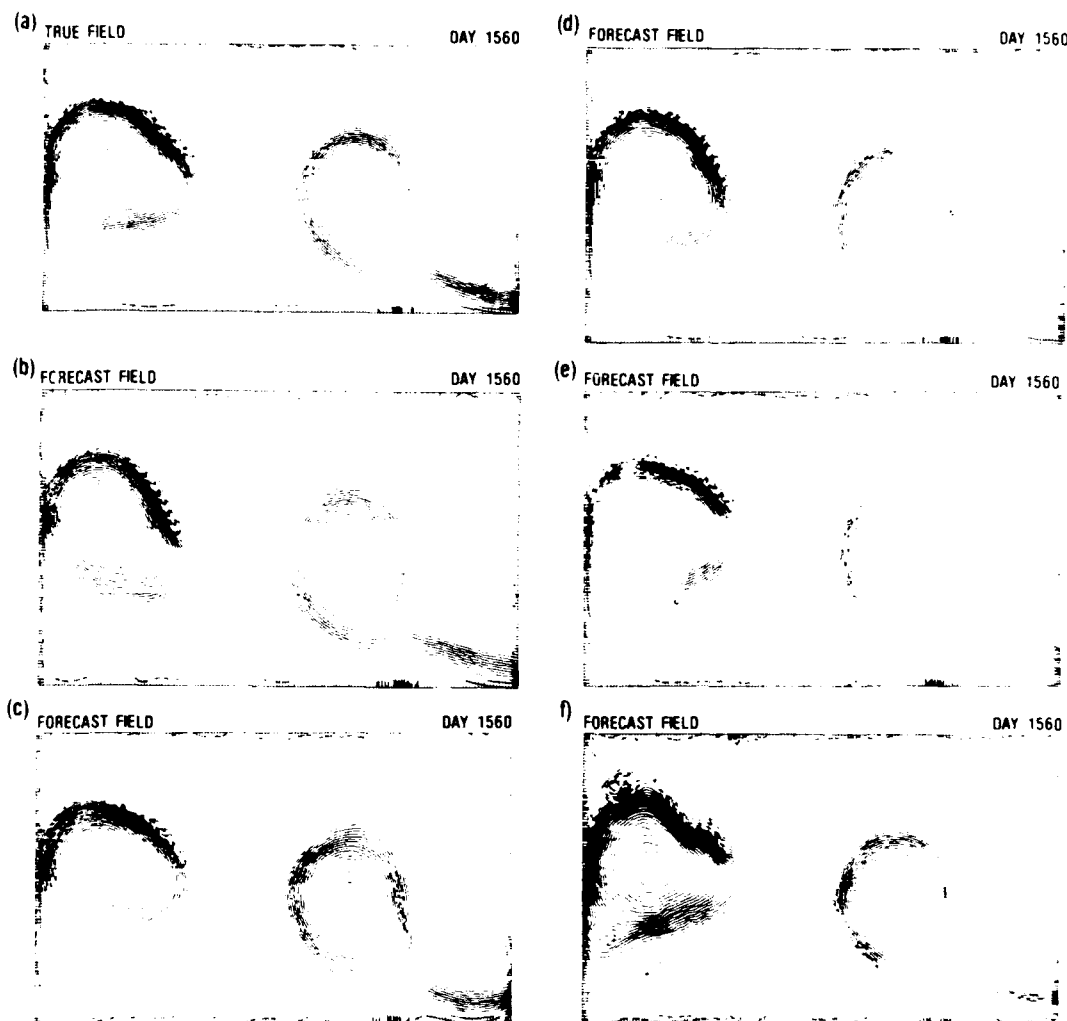


Fig. 22. Contour plots of height field for true solution (a) and five forecasts using 36-day repeat track observations. All plots are for one month after the start of the forecast. (a) True field. (b) Asynoptic height field used to initialize height field. No updating is applied during nowcast or forecast (Figure 21a, curve 2). (c) Same as (b) except that nowcast is updated (Figure 21a, curve 1). (d) Nowcast is initialized with time interpolated field; no updating is applied (Figure 20). (e) Same as (d), except that nowcast is updated (Figure 21a, curve 3). (f) Same as (e) except that forecast is updated to day 1578.

mesoscale variability in a variety of regions throughout the globe. Recall that the track spacing used in this report did not take into account the poleward convergence of tracks; this convergence is approximately proportional to the cosine of the latitude. Hence at mid-latitudes the 24-day repeat tracks would actually be approximately 90 km apart, and the 36-day tracks would have a spacing of about 60 km (Table 2). Given such track spacing and the ability of the numerical model to assimilate the data and correct for asynopticity, the potential benefits of altimeter-derived sea surface heights are indeed significant.

6. SUMMARY AND CONCLUSIONS

This work used simulated asynoptic perfect altimeter data and a one-layer reduced gravity model of the Gulf of Mexico to examine such issues as (1) the track spacing required to adequately resolve oceanic eddies, (2) the initialization of a dynamic primitive equation forecast model using only altimeter derived sea surface heights, (3) the effects of the asynopticity of the observations on the forecast, and (4) the use of an initialization updating technique to improve the forecast. The simulated data were obtained by flying a hypothetical altimeter

over the model ocean and sampling the model sea surface in a manner similar to that of a real altimeter. Among the issues that were not addressed in the study were the assimilation of altimeter data into a multilayer model and the effects of error on the measurement of the dynamic sea surface height. Error in the height field can be caused by instrument noise, imperfect correction for environmental effects, orbit uncertainty, and/or inadequate knowledge of the geoid.

The stationary sampling studies revealed that a circular eddy requires two tracks (either ascending or descending) across the eddy to ensure adequate spatial resolution. An eddy with a highly irregular shape may require three or four tracks. The study also discovered that if the track spacing is sufficient to resolve the height field of an eddy, the along-track geostrophic velocity component is determined with comparable accuracy to that of the cross-track component.

The simulated asynoptic altimeter measurements of sea surface height were obtained by (1) integrating the Gulf of Mexico model to statistical equilibrium, (2) flying a hypothetical altimeter with a realistic track sequence over the model ocean, and (3) objectively mapping the perfect sampled data onto a numerical grid. The tracks were assumed to repeat

TABLE 2. Track Spacing as a Function of Repeat Period Latitude

Latitude	Repeat Period, days			
	72	36	24	17
0	40	80	120	164
25	36	72	108	149
40	31	61	92	126

Track spacing given in kilometers. The values were determined by assuming that the poleward convergence of ground tracks is a function only of the cosine of the latitude and the altitude of the satellite orbit is 800 km.

exactly with a period of 72, 36, or 24 days. The model was initialized and restarted by using the "observed" height field and a geostrophically balanced velocity field. Experiments were conducted using one of two model oceans. The first one utilized a grid spacing of 20 km and an eddy viscosity coefficient of $300 \text{ m}^2 \text{ s}^{-1}$. The large anticyclonic eddy that sheds from the Loop Current had a diameter of approximately 600 km and a regular behavior pattern. The second model ocean was identical to the first except that the grid resolution and eddy viscosity coefficient were reduced to 10 km and $100 \text{ m}^2 \text{ s}^{-1}$, respectively. This ocean exhibited much greater temporal and spatial variability. In both model simulations, no wind forcing was applied, and the transport through the Yucatan Straits remained constant.

Three types of forecast experiments were conducted:

1. The nowcast (that period prior to the start of the forecast during which the observations were collected) is initialized with the asymptotic data set; the model is integrated forward with no updating applied during the nowcast or forecast.

2. An initialization updating scheme is applied during the nowcast but not during the forecast.

3. Both the nowcast and the forecast are updated.

The updating technique inserts the observed altimeter heights into the nowcast forecast on a track by track basis.

The results of the Gulf of Mexico forecast experiments demonstrated the following.

1. The optimum updating period is at least every 12 days or (for the assumed track pattern) four tracks at a time.

2. Suitable application of the initialization updating scheme during the nowcast always resulted in a more accurate forecast. In the 20-km grid experiments the asymptoticity of the 72-day repeat track observations was reduced so effectively that the forecast was just as accurate as the one using the 24-day repeat track data. The RMS errors of both forecasts were approximately 5% after 100 days. The time scale for the reduction of the asymptotic error is the repeat period of the satellite. The 10-km grid forecasts also showed significant improvement. These simulations displayed an impressive ability of the sampling modeling to detect and predict the behavior of a small ($\sim 200 \text{ km}$), swiftly moving ($\sim 5\text{--}6 \text{ cm s}^{-1}$) eddy that played a key role in the dynamics of the model ocean.

3. Repeated application of an updating scheme in an unstable oceanic regime may result in the generation of spurious eddies at the edge(s) of the inserted data patch. For rapidly evolving unstable regions the development of a multibeam altimeter [Bush *et al.*, 1984] would provide a significant improvement over the single-beam altimeter measurements.

The interaction between asymptotic altimeter data and a hydrodynamic numerical model indicates that both adequate spatial and temporal resolution may be possible with a single nadir beam altimeter, particularly for oceanic regimes such as

the Gulf of Mexico. The observations form the basis of the model initialization, and in turn, the model "corrects" the asymptoticity of the data. The result is an accurate nowcast that for highly asymptotic data would not have been possible without the use of the model. A sampling strategy should favor spatial resolution. A track spacing that resolves the important dynamic features should be chosen; the inherent asymptoticity of the measurements can be reduced by applying an initialization updating scheme to the numerical nowcast. In dynamically complex regions, such as near western boundary currents, a multiple beam altimeter or multiple single beam altimeters may be required for sufficient spatial and temporal resolution.

It should be noted that the ability of a numerical scheme to generate a realistic nowcast depends on the numerical and physical accuracy of the model. For the simulations presented above, the model dynamics match the dynamics of the "true" solution exactly. Certainly this is not the case in a true forecast. Although reduced gravity models are able to simulate a variety of oceanic phenomena, it is necessary to develop assimilation schemes for multilayer models and more complex forecasting scenarios [see Hurlburt, 1985]. Future simulation experiments will utilize multi-vertical mode models in the Gulf Stream region. However, the simple experiments presented in this study are encouraging for the eventual use of satellite altimetry in ocean monitoring and prediction.

NOTATION

- A lateral eddy viscosity coefficient.
- f Coriolis parameter.
- g acceleration due to gravity.
- g' reduced gravity, equal to $g \nabla \rho / \rho$.
- h instantaneous local thickness of the layer.
- H initial thickness of the upper layer.
- ξ free surface anomaly; deviation of free surface above its initial flat position.
- PHA pycnocline height anomaly; deviation of interface below its initial uniform position.
- $\Delta \rho$ density difference between upper and lower layers.
- ρ average density of model ocean.
- t time.
- u velocity component in x direction.
- v velocity component in y direction.
- V transport, equal to $h \bar{u}$.
- x, y, z Cartesian coordinates with x positive eastward, y positive northward, and z positive upward.
- τ surface wind stress vector.

Acknowledgments. This paper is a contribution to NORDA's Special Focus Program, "Ocean Dynamics from Altimetry," funded by the Office of Naval Research. I would like to acknowledge Monty Peffley of NORDA for developing the software for the synoptic sampling of the model ocean by the simulated altimeter. Appreciation is also extended to Harley Hurlburt, Dana Thompson, and Jim Mitchell of NORDA for many informative discussions as well as their useful comments and suggestions during the research. The numerical model, which was originally designed by Harley Hurlburt, utilized a fast, vectorized Helmholtz solver provided by Daniel Moore of Imperial College, London. A graphics package was provided by the National Center for Atmospheric Research. The numerical calculations were performed on the two-pipeline Texas Instruments Advanced Scientific Computer at the Naval Research Laboratory in Washington, D. C. Appreciation is extended to Charlene Parker for typing the manuscript.

REFERENCES

- Bengtsson, L., M. Ghil, and E. Kallen (Eds.), *Dynamic Meteorology: Data Assimilation Methods*, Appl. Math. Sci. Ser., vol. 36, 330 pp., Springer-Verlag, New York, 1981.

- Bush, G. B., E. B. Dobson, R. Matyskiela, C. C. Kilgus, and E. J. Walsh. An analysis of a multibeam altimeter, *Mar. Geod.*, 8, 345-384, 1984.
- Cheney, R. E., Comparison data for Seasat altimetry in the western North Atlantic, *J. Geophys. Res.*, 87, 3247-3253, 1982.
- Cheney, R. E., and J. G. Marsh, Seasat altimeter observations of dynamic topography in the Gulf Stream region, *J. Geophys. Res.*, 86, 473-483, 1981.
- Committee on Geodesy, Geodesy, A look to the future, report, Natl. Res. Coun. Board of Earth Sci., Natl. Acad. of Sci., Washington, D. C., in press, 1985.
- DeMey, P., and A. R. Robinson, Simulation and assimilation of satellite altimeter data at the oceanic mesoscale, paper presented at the URSI Commission F Symposium and Workshop, Shresh, Israel, May 1984.
- Fu, L., Recent progress in the application of satellite altimetry to observing the mesoscale variability and general circulation of the oceans, *Rev. Geophys.*, 21, 1657-1666, 1983.
- Ghil, M., The compatible balancing approach to initialization, and four-dimensional data assimilation, *Fellus*, 32, 198-206, 1980.
- Hurlburt, H. E., The potential for ocean prediction and the role of altimeter data, *Mar. Geod.*, 8, 17-65, 1984.
- Hurlburt, H. E., Dynamic transfer of simulated altimeter data into subsurface information by a numerical ocean model, *J. Geophys. Res.*, this issue.
- Hurlburt, H. E., and J. D. Thompson, A numerical study of Loop Current intrusions and eddy shedding, *J. Phys. Oceanogr.*, 10, 1611-1651, 1980.
- Lai, D. Y., and P. L. Richardson, Distribution and movement of Gulf Stream rings, *J. Phys. Oceanogr.*, 7, 670-683, 1977.
- Mitchell, J. L., Z. R. Hallock and J. D. Thompson, The REX and the U.S. Navy Geosat, *Nav. Res. Rev.*, in press, 1985.
- Robinson, A. R., and W. G. Leslie, Estimation and prediction of oceanic eddy fields, in *Essays on Oceanography: A Tribute to John Swallow*, edited by J. Crease, W. J. Gould, and P. M. Saunders, *Prog. Oceanogr. Ser.*, vol. 14, Pergamon, New York, 1985.
- Tapley, B. D., G. H. Born, and M. E. Parke, The Seasat altimeter data and its accuracy assessment, *J. Geophys. Res.*, 87, 3179-3188, 1982.
- Thompson, J. D., Altimeter data and geoid error in mesoscale ocean prediction: Some results from a primitive equation model, *J. Geophys. Res.*, this issue.
- Wunsch, C., and E. M. Gaposchkin, On using satellite altimetry to determine the general circulation of the oceans with application to geoid improvement, *Rev. Geophys.*, 18, 725-745, 1980.
- Zlotnicki, V., On the accuracy of gravimetric geoids and the recovery of oceanographic signals from altimetry, *Mar. Geod.*, 8, 129-158, 1984.

John C. Kindle, Ocean Dynamics and Prediction Branch, Code 323, Naval Ocean Research and Development Activity, NSTL, MS 39529.

(Received February 12, 1985;
accepted March 5, 1985)

DISTRIBUTION LIST

Commander
Space and Naval Warfare Sys Com
Attn: CAPT Carl Hoffman
Code PMW-141
2511 Jefferson Davis Highway
Washington, DC 2-363-5100

Oceanographer of the Navy
Chief of Naval Operations
Attn: OP-096B (R. Feden)
OP-961E2 (J. Malay)
U.S. Naval Observatory
34th and Massachusetts Ave., NW
Washington, DC 20390-1800

Space and Naval Warfare Sys Com
Attn: LCDR Bill Cook
2511 Jefferson Davis Highway
Washington, DC 20363-5100

Naval Oceanography Command
Attn: Dr. Paul Moersdorf
Stennis Space Center, MS 35925

Commanding Officer
Fleet Numerical Oceanography Ctr
Attn: CAPT Jack Jensen
Monterey, CA 93943-5004

Naval Oceanographic Office
Attn: CAPT Charles A. Martinek
Stennis Space Center, MS 39529

Planning Systems, Inc.
Attn: Dr. R. L. Crout (MT)
115 Christian Lane
Seattle, WA 98188

BDM
Attn: Max Coon
16300 Christensen Road
Slidell, LA 70458

Navy/NOAA Joint Ice Center
Attn: Mr. Gary Whol
4301 Suitland Road
Washington, DC 20395

NOARL Liaison Office
Attn: Mr. Brooke Farquhar
Crystal Plaza #5, Room 802
2211 Jefferson Davis Highway
Arlington, VA 22202-5000

NOARL
Code 100
115
125L (10)
125P
200
300
320
321 (25)
322 (R. Preller)

Naval Postgraduate School
Attn: Dr. Curtis A. Collins
Dept of Oceanography, Code 68
Monterey, CA 93943

Commander
Naval Ocean Systems Center
Attn: Dr. Barbara Scitirin
San Diego, CA 92152-5000

NOARL Code 332
Attn: Dr. Duane Eppler
72 Lyme road
Hanover, NH 03755-1290

Naval Oceanographic Office
Attn: Mr. Andrew Johnson
Stennis Space Center, MS 39529

Naval Oceanographic Office
Attn: Mr. James Rigney
Stennis Space Center, MS 39529

Applied Physics Laboratory
Polar Science Center
Attn: Dr. R. A. Rothrock
1013 NE 40th Street
Seattle, WA 98105

NOARL
Attn: Mr. Robert W. Fett
Code 441
Monterey, CA 93934-5006

Naval Polar Oceanography Ctr.
Attn: Mr. David Benner
4301 Suitland Road
Washington, DC 20390

U.S. Naval Observatory
Attn: Mr. Don Montgomery
34th and Massachusetts Ave., NW
Washington, DC 20392-1800

Applied Research Laboratories
Attn: Dr. Nancy Bedford
P.O. Box 8029
University of Texas at Austin
Austin, TX 78713-8029

Director
Office of Naval Technology
Attn: Dr. C. V. Votaw, code 234
Dr. M. Briscoe, Code 229
800 N. Quincy Street
Arlington, VA 22217-5000

Commanding Officer
Naval Research Laboratory
Attn: CAPT John J. Donegan, Jr
Washington, DC 20375

Institute of Naval Oceanography
Attn: Dr. John Leese
Stennis Space Center, MS 39529

Naval Research Laboratory
Attn: Dr. Vincent Noble
Washington, DC 20375-5000

Naval Polar Oceanography Ctr.
Attn: LCDR Kathy Garcia
4301 Suitland Road
Washington, DC 20390

Commander
Naval Oceanography Command
Attn: W. Shutt
Stennis Space Center, MS 39529

Sverdrup Technology, Inc.
Applied Math & Physics Section
Attn: Dr. Vivien Cambridge
Bldg. 2109
Stennis Space Center, MS 39529

Director
Office of Naval Research
Attn: Dr E. Hartwig, Code 112
Dr E. Silva, Code 10D/10P
Dr C. Luther, Code 112D1
Dr T. Curtin

Director
National Ocean Data Center
WSC1 Rm 103
6001 Executive Blvd
Attn: G. W. Withee
Rockville, MD 20852

Commander
Naval Oceanography Command
Attn: RADM J. E. Koehr
Stennis Space Center, MS 39529

NOARL
Attn: Dr. John Hovermale
Code 400
Monterey, CA 93943-5006

Naval Postgraduate School
Attn: Dr. C. Wash
Monterey, CA 93943

REPORT DOCUMENTATION PAGE

Form Approved
CSM No. 0704-0188

Public reporting burden for this collection of information is estimated to average 1 hour per response, including the time for reviewing instructions, searching existing data sources, gathering and maintaining the data needed, and completing and reviewing the collection of information. Send comments regarding this burden estimate or other aspect of this collection of information, including suggestions for reducing this burden, to Washington Headquarters Services, Directorate for Information Operations and Reports, 1215 Jefferson Davis Highway, Suite 1204, Arlington, VA 22202-4302, and to the Office of Management and Budget, Paperwork Reduction Project (0704-0188), Washington, DC 20503.

1. Agency Use Only (Leave blank).		2. Report Date. November 1990		3. Report Type and Dates Covered. Final	
4. Title and Subtitle Satellite Altimetry for Naval Oceanography				5. Funding Numbers. Program Element No. 63704N Project No. 0101 Task No. 100 Accession No. DN294462	
6. Author(s). D. R. Johnson					
7. Performing Organization Name(s) and Address(es). Naval Oceanographic and Atmospheric Research Laboratory Ocean Science Directorate Stennis Space Center, Mississippi 39529-5004				8. Performing Organization Report Number. NOARL Technical Note 87	
9. Sponsoring/Monitoring Agency Name(s) and Address(es). Space and Naval Warfare Systems Command Washington, DC				10. Sponsoring/Monitoring Agency Report Number. NOARL Technical Note 87	
11. Supplementary Notes.					
12a. Distribution/Availability Statement. Approved for public release; distribution is unlimited.				12b. Distribution Code.	
13. Abstract (Maximum 200 words). Taking advantage of experience gained during the flight of the U.S. Navy's GEOSAT altimeter, this technical note discusses some of the problems encountered and recommends new approaches for future altimeter systems. In particular, I strongly urge that exact-repeat track sampling be continued for the next decade. Optimum sampling for mesoscale features can be realistically accomplished with three altimeters flying at 7-day refresh periods with equidistant cross-track spacing. More formal recommendations will come with the results of current studies using various configurations during mission simulations. It is also recommended that additional effort be invested in sea-ice monitoring and in geophysical corrections.					
14. Subject Terms. (U) Remote Sensing, (U) Satellite Altimeter, (U) Automated Techniques				15. Number of Pages. 98	
				16. Price Code.	
17. Security Classification of Report. Unclassified	18. Security Classification of This Page. Unclassified	19. Security Classification of Abstract. Unclassified	20. Limitation of Abstract. SAR		